

Fundamental Core Effects in Co-Cr-Fe-Ni Based High Entropy Alloys

2019

Abhishek Mehta
University of Central Florida

Find similar works at: <https://stars.library.ucf.edu/etd>

University of Central Florida Libraries <http://library.ucf.edu>

 Part of the [Materials Science and Engineering Commons](#)

STARS Citation

Mehta, Abhishek, "Fundamental Core Effects in Co-Cr-Fe-Ni Based High Entropy Alloys" (2019). *Electronic Theses and Dissertations*. 6333.
<https://stars.library.ucf.edu/etd/6333>

This Doctoral Dissertation (Open Access) is brought to you for free and open access by STARS. It has been accepted for inclusion in Electronic Theses and Dissertations by an authorized administrator of STARS. For more information, please contact lee.dotson@ucf.edu.

FUNDAMENTAL CORE EFFECTS IN Co-Cr-Fe-Ni BASED HIGH ENTROPY ALLOYS

by

ABHISHEK MEHTA

B.Tech. Malaviya National Institute of Technology Jaipur, India, 2010

M.S. University of Central Florida, 2015

A dissertation submitted in partial fulfillment of the requirements
for the degree of Doctor of Philosophy
in the Department of Materials Science and Engineering
in the College of Engineering and Computer Science
at the University of Central Florida
Orlando, Florida

Spring Term

2019

Major Professor: Yongho Sohn

© 2019 Abhishek Mehta

ABSTRACT

High entropy alloys (HEAs) are near equiatomic multi-principal-element-alloys (MPEAs) which are different from traditional solvent-based multicomponent alloys. Based on initial work by Yeh and Co-workers, they were proposed to exhibit four “core” effects: high entropy, sluggish diffusion, lattice distortion, and cocktail effect. Present work investigates two of the four “core” effects, i.e. high entropy and sluggish diffusion effects, in Co-Cr-Fe-Ni based transition metal high entropy alloys. Solid-to-solid diffusion couple approach was adopted to investigate, these core effects. Experimental results contradicts the “high entropy” effect based on thermodynamics analysis: that the HEAs with low entropy of mixing may be thermodynamically more stable than the HEA of similar constituent elements with high entropy of mixing. In such cases, enthalpy of mixing can also play a vital role in stabilizing the HEA with lower entropy of mixing. Measurement of diffusion coefficients (i.e. both interdiffusion and tracer diffusion coefficients) in HEAs and its comparison with conventional solvent-based multicomponent alloys suggests that diffusion is not always sluggish in high entropy alloys. Contrary to previous findings, larger fluctuations in lattice potential energy (LPE) of an alloy may not always result in anomalously slow diffusion, in comparison to alloy systems which exhibits smaller fluctuation in LPE. Findings from his dissertation provide a “controversial” understanding of high entropy alloys, and alloy development strategies in the future for the most aggressive applications such as those found in gas turbines and nuclear reactors. As these applications will certainly require the knowledge of high temperature stability and nature of diffusion under extreme application environment.

The author would like to dedicate this work to his friends and family

ACKNOWLEDGMENTS

I would like to express my deepest gratitude to those who helped and encouraged me during my Ph.D. study in Materials Science and Engineering. I am deeply indebted to my advisor Dr. Yongho Sohn for all the help, guidance and continued assistantship support during my Ph.D. In addition to my advisor, I would also like to thank my dissertation committee members: Dr. Kevin Coffey, Dr. Akihiro Kushima, Dr. Tengfei Jiang, and Dr. Sergey Stolbov for their encouragements and valuable guidance. I would also like to thank my fellow colleagues for their overall help and support in the laboratory. Special thanks to Mr. Edward Dein for teaching the operation of arc-melter, carrying out E-beam physical vapour deposition (PVD) for this project and overall technical support in the laboratory. Great appreciation goes to the staff of Materials characterization Facility for their support.

I also want to express my sincere gratitude to Dr. Dennis D. Keiser, Jr. at the Idaho National Laboratory (INL) for his financial support and sponsorship. Also, thanks to Dr. Bharat Gwalani at Pacific Northwest National Lab (PNNL) for valuable discussions on HEAs.

Finally, I would like to thank my friends and family for their endless support and patience.

TABLE OF CONTENTS

LIST OF FIGURES	ix
LIST OF TABLES	xvii
CHAPTER 1 INTRODUCTION	1
1.1 General Background	1
1.2 Motivation.....	3
1.3 Objective.....	4
CHAPTER 2 LITERATURE REVIEW	6
2.1 Core effects in High Entropy alloys.....	6
2.2 Sluggish Diffusion in High Entropy alloys.....	8
2.3 Diffusion Coefficients.....	11
2.3.1 Interdiffusion coefficients.....	11
2.3.2 Tracer diffusion coefficient	14
2.4 Potential energy fluctuation model	19
2.5 Solid-solution phase formation rule pertaining to HEAs.....	21
CHAPTER 3 THEORETICAL VALIDATION OF FORMALISM TO MEASURE TRACER DIFFUSION COEFFICIENT	24
3.1 Concentration profiles.....	24
3.2 Validation.....	25
CHAPTER 4 EXPERIMENTAL METHODS.....	33
4.1 Alloy Preparation	33

4.2 Thin Film Deposition	34
4.3 Diffusion Couples	35
4.4 Characterization	38
CHAPTER 5 HIGH ENTROPY EFFECT.....	40
5.1 Solubility limit of Al in Al-Co-Cr-Fe-Ni alloy.....	41
5.2 Solubility limit of Al in Al-Co-Cr-Fe-Ni-Mn alloy	49
5.3 Role of Enthalpy of mixing.....	56
5.4 Application of Solid solution formation rules to off-equiatomic compositions generated in diffusion couples	60
CHAPTER 6 SLUGGISH DIFFUSION EFFECT.....	63
6.1 Measurement of average effective interdiffusion coefficients.....	64
6.1.1 Fe ₅₀ Cr ₅₀ vs. Co ₅₀ Ni ₅₀ quaternary diffusion couples	64
6.1.2 Co ₂₀ Cr ₂₇ Fe ₃₃ Ni ₂₀ vs Co ₃₀ Cr ₂₀ Fe ₂₀ Ni ₃₀ quaternary diffusion couples	68
6.1.3 Co ₂₅ Cr ₂₅ Ni ₂₅ Fe ₁₅ Mn ₁₀ vs Co ₁₅ Cr ₁₅ Ni ₁₅ Fe ₂₅ Mn ₃₀ quinary diffusion couples...	72
6.1.4 Al ₆ Co ₁₉ Cr ₂₈ Fe ₂₈ Ni ₁₉ vs. Al ₆ Co ₂₈ Cr ₁₉ Fe ₁₉ Ni ₂₈ quinary diffusion couples.....	76
6.1.5 Al ₄₈ Ni ₅₂ vs. Co ₂₅ Cr ₂₅ Fe ₂₅ Ni ₂₅ quinary diffusion couples.....	79
6.1.6 Al ₄₈ Ni ₅₂ vs. Co ₂₀ Cr ₂₀ Fe ₂₀ Ni ₂₀ Mn ₂₀ senary diffusion couples.....	82
6.2 Comparison of interdiffusion coefficients	86
6.3 Measurement of Tracer diffusion coefficient	91
6.3.1 Tracer diffusion coefficient of Ni in quaternary CoCrFeNi alloy	91
6.3.2 Tracer diffusion coefficient of Ni in quinary CoCrFeNiMn alloy	93

6.3.3	Tracer diffusion coefficient of Ni in quinary Al _{0.25} CoCrFeNi alloy	95
6.4	Comparison of Tracer diffusion coefficient of Ni in various FCC alloys	97
6.5	Potential Energy Fluctuation and Excess Entropy	99
CHAPTER 7	SUMMARY AND CONCLUSIONS	108
7.1	High Entropy Effect	108
7.2	Sluggish Diffusion Effect	109
7.3	Overall Conclusion	110
APPENDIX A:	X-RAY DIFFRACTION AND COMPOSITION OF ALLOYS	111
A.1	Compositions of alloys	112
A.2	X-ray diffraction of alloys	113
APPENDIX B:	LIST OF PUBLICATIONS AND PRESENTATION	120
B.1	Publications	121
B.2	Conference Presentations	123
LIST OF REFERENCES	125

LIST OF FIGURES

Figure 1. Example of alloy design in (a) traditional multicomponent alloy (MCA), and (b) High Entropy alloy (HEA).....	1
Figure 2. Entropy based classification of alloys	2
Figure 3. Configuration of alloys in sandwich type arrangement for measurement of tracer diffusion coefficient.	16
Figure 4. Geometrical representation of Gaussian distribution function	19
Figure 5. Schematic representation of diffusion couple arrangement to measure tracer diffusion coefficient using Belova et al. approach.	26
Figure 6. Demonstration of Subtraction method of interdiffusion profile from spike profile when $D/D^*=10$ with 1 μm film thickness. Concentration profile at (a) interdiffusion interface, (b) Spike interface. (c) Superimposed Spike profile over interdiffusion profile, and (d) Gaussian fitting implemented on subtracted (difference) profile.....	28
Figure 7. Demonstration of Subtraction method of interdiffusion profile from spike profile when $D/D^*=1$ with 1 μm film thickness. Concentration profile at (a) interdiffusion interface, (b) Spike interface. (c) Superimposed Spike profile over interdiffusion profile, and (d) Gaussian fitting implemented on subtracted (difference) profile.....	29
Figure 8. Demonstration of Subtraction method of interdiffusion profile from spike profile when $D/D^*=0.1$ with 1 μm film thickness. Concentration profile at (a) interdiffusion interface, (b)	

Spike interface. (c) Superimposed Spike profile over interdiffusion profile, and (d) Gaussian fitting implemented on subtracted (difference) profile..... 29

Figure 9. Demonstration of Subtraction method of interdiffusion profile from Spike profile when $D/D^* = 2$ with 1 μm film thickness. Concentration profile at (a) interdiffusion interface, (b) Spike interface. (c) Superimposed Spike profile over interdiffusion profile, and (d) Gaussian fitting implemented on subtracted (difference) profile..... 30

Figure 10. Demonstration of Subtraction method of interdiffusion profile from spike profile when $D/D^* = 2$ with 2 μm film thickness. Concentration profile at (a) interdiffusion interface, (b) Spike interface. (c) Superimposed Spike profile over interdiffusion profile, and (d) Gaussian fitting implemented on subtracted (difference) profile..... 30

Figure 11. Demonstration of Subtraction method of interdiffusion profile from spike profile when $D/D^* = 2$ with 3 μm film thickness. Concentration profile at (a) interdiffusion interface, (b) Spike interface. (c) Superimposed Spike profile over interdiffusion profile, and (d) Gaussian fitting implemented on subtracted (difference) profile..... 31

Figure 12. A schematic of electron beam physical vapor deposition system. 35

Figure 13. Concentration profiles superimposed on BSE micrographs of $\text{Al}_{48}\text{Ni}_{52}$ vs. $\text{Co}_{25}\text{Cr}_{25}\text{Fe}_{25}\text{Ni}_{25}$ diffusion couples isothermally annealed at (a) 900°C for 240 hours, (b) 1000°C for 120 hours, (c) 1100°C for 48 hours, and (d) 1200°C for 24 hours. 42

Figure 14. Pseudo-binary phase diagram between Al and equiatomic CoCrFeNi 43

Figure 15. Comparison of maximum solubility limit of Al as a function of temperature in $Al_pCo_qCr_rFe_sNi_t$ (via diffusion couple) and $Al_xCoCrFeNi$ (via. phase diagram) HEAs. 44

Figure 16. (a) Comparison of Entropy of mixing ($\Delta S_{mix}/R$) in $Al_pCo_qCr_rFe_sNi_t$ (using diffusion couple), and $Al_xCoCrFeNi$ (using phase diagram) for the compositions corresponding to the maximum solubility limit of Al. (b) Comparison of thermodynamic parameters measured in the $Al_pCo_qCr_rFe_sNi_t$, and $Al_xCoCrFeNi$ alloys..... 46

Figure 17. (a) Comparison of correlated entropy of mixing ($\Delta S_{Corr}/R$) in $Al_pCo_qCr_rFe_sNi_t$ (using diffusion couple), $Al_xCoCrFeNi$ (using phase diagram) for the compositions corresponding to the maximum solubility limit of Al. (b) Comparison of correlated thermodynamic parameters measured in the $Al_pCo_qCr_rFe_sNi_t$ and $Al_xCoCrFeNi$ alloys. 48

Figure 18. Concentration profiles superimposed on BSE micrographs of $Al_{48}Ni_{52}$ vs. $Co_{20}Cr_{20}Ni_{20}Fe_{20}Mn_{20}$ diffusion couples isothermally annealed at (a) 900°C for 240 hours, (b) 1000°C for 120 hours, (c) 1100°C for 48 hours, and (d) 1200°C for 24 hours. 50

Figure 19. Pseudo-binary phase diagram between Al and equiatomic CoCrFeNiMn..... 51

Figure 20. Comparison of maximum solubility limit of Al as a function of temperature in $Al_pCo_qCr_rFe_sNi_tMn_u$ (via. diffusion couple) and $Al_xCoCrFeNiMn$ (via. phase diagram) HEAs. 51

Figure 21. (a) Comparison of Entropy of mixing ($\Delta S_{mix}/R$) in $Al_pCo_qCr_rFe_sNi_t$ (using diffusion couple), and $Al_xCoCrFeNi$ (using phase diagram) for the compositions corresponding to the maximum solubility limit of Al. (b) Comparison of thermodynamic parameters measured in the $Al_pCo_qCr_rFe_sNi_t$, and $Al_xCoCrFeNi$ 53

Figure 22. (a) Comparison of correlated entropy of mixing ($\Delta S_{\text{Corr.}}/R$) in $\text{Al}_p\text{Co}_q\text{Cr}_r\text{Fe}_s\text{Ni}_t\text{Mn}_u$ (using diffusion couple) and $\text{Al}_x\text{CoCrFeNiMn}$ (using phase diagram), (b) Comparison of correlated thermodynamic parameters measured in the $\text{Al}_p\text{Co}_q\text{Cr}_r\text{Fe}_s\text{Ni}_t\text{Mn}_u$ and $\text{Al}_x\text{CoCrFeNiMn}$ 55

Figure 23. Application of solid-solubility predictors to the various off-equiatomic FCC $\text{Al}_p\text{Co}_q\text{Cr}_r\text{Fe}_s\text{Ni}_t$ generated in the diffusion couples. (a) Ω - δ , (b) $\Delta H_{\text{mix.}}$ - δ , (c) VEC- δ , and (d) $\Delta\chi$ - δ plot. 61

Figure 24. Application of solid-solubility predictors to the various off-equiatomic FCC $\text{Al}_p\text{Co}_q\text{Cr}_r\text{Fe}_s\text{Ni}_t\text{Mn}_u$ generated in the diffusion couples. (a) Ω - δ , (b) $\Delta H_{\text{mix.}}$ - δ , (c) VEC- δ , and (d) $\Delta\chi$ - δ plot. 62

Figure 25. Concentration profiles superimposed on BSE micrographs of $\text{Fe}_{50}\text{Cr}_{50}$ vs. $\text{Co}_{50}\text{Ni}_{50}$ diffusion couples isothermally annealed at (a) 900°C for 120 hours, (b) 1000°C for 120 hours, (c) 1100°C for 48 hours, and (d) 1200°C for 48 hours 65

Figure 26. Temperature dependence of average effective interdiffusion coefficients for Co, Cr, Fe and Ni in BCC FeCr alloy and FCC CoNi measured using $\text{Fe}_{50}\text{Cr}_{50}$ vs. $\text{Co}_{50}\text{Ni}_{50}$ diffusion couples in temperature range from 900° to 1200°C 68

Figure 27. Concentration profiles superimposed on BSE micrographs of $\text{Co}_{20}\text{Cr}_{27}\text{Fe}_{33}\text{Ni}_{20}$ vs $\text{Co}_{30}\text{Cr}_{20}\text{Fe}_{20}\text{Ni}_{30}$ diffusion couples isothermally annealed at (a) 900°C for 240 hours, (b) 1000°C for 240 hours, (c) 1100°C for 240 hours, and (d) 1200°C for 48 hours. 69

Figure 28. Temperature dependence of average effective interdiffusion coefficients for Co, Cr, Fe and Ni in $\text{Co}_{20}\text{Cr}_{27}\text{Fe}_{33}\text{Ni}_{20}$ vs $\text{Co}_{30}\text{Cr}_{20}\text{Fe}_{20}\text{Ni}_{30}$ diffusion couples in temperature range from 900° to 1200°C.	72
Figure 29. Concentration profiles superimposed on BSE micrographs of $\text{Co}_{25}\text{Cr}_{25}\text{Ni}_{25}\text{Fe}_{15}\text{Mn}_{10}$ vs $\text{Co}_{15}\text{Cr}_{15}\text{Ni}_{15}\text{Fe}_{25}\text{Mn}_{30}$ diffusion couples isothermally annealed at (a) 900°C for 120 hours, (b) 1000°C for 120 hours, (c) 1100°C for 48 hours, and (d) 1200°C for 48 hours.	73
Figure 30. Temperature dependence of average effective interdiffusion coefficients for Co, Cr, Fe, Ni, and Mn in $\text{Co}_{25}\text{Cr}_{25}\text{Ni}_{25}\text{Fe}_{15}\text{Mn}_{10}$ vs $\text{Co}_{15}\text{Cr}_{15}\text{Ni}_{15}\text{Fe}_{25}\text{Mn}_{30}$ diffusion couples in temperature range from 900 to 1200°C.....	75
Figure 31. Concentration profiles superimposed on BSE micrographs of $\text{Al}_6\text{Co}_{19}\text{Cr}_{28}\text{Fe}_{28}\text{Ni}_{19}$ vs. $\text{Al}_6\text{Co}_{28}\text{Cr}_{19}\text{Fe}_{19}\text{Ni}_{28}$ diffusion couples isothermally annealed at (a) 900°C for 240 hours, (b) 1000°C for 120 hours, (c) 1100°C for 48 hours, and (d) 1200°C for 24 hours.	76
Figure 32. Temperature dependence of average effective interdiffusion coefficients for Co, Cr, Fe and Ni in $\text{Al}_6\text{Co}_{19}\text{Cr}_{28}\text{Fe}_{28}\text{Ni}_{19}$ vs. $\text{Al}_6\text{Co}_{28}\text{Cr}_{19}\text{Fe}_{19}\text{Ni}_{28}$ diffusion couples in temperature range from 900° to 1200°C.....	78
Figure 33. Temperature dependence of average effective interdiffusion coefficients for Co, Cr, Fe and Ni in FCC $\text{Co}_{25}\text{Cr}_{25}\text{Fe}_{25}\text{Ni}_{25}$ end member alloy measured using $\text{Al}_{48}\text{Ni}_{52}$ vs. $\text{Co}_{25}\text{Cr}_{25}\text{Fe}_{25}\text{Ni}_{25}$ diffusion couples in temperature range from 900 to 1200°C.....	81

Figure 34. Temperature dependence of average effective interdiffusion coefficients for Al, Co, Cr, Fe and Ni in BCC $Al_{48}Ni_{52}$ end member measured using $Al_{48}Ni_{52}$ vs. $Co_{25}Cr_{25}Fe_{25}Ni_{25}$ diffusion couples in temperature range from 900° to 1200°C 82

Figure 35. Temperature dependence of average effective interdiffusion coefficients for Al, Co, Cr, Fe, Ni, and Mn in FCC $Co_{20}Cr_{20}Fe_{20}Ni_{20}Mn_{20}$ end member alloy measured using $Al_{48}Ni_{52}$ vs. $Co_{20}Cr_{20}Fe_{20}Ni_{20}Mn_{20}$ diffusion couples in temperature range from 900° to 1200°C..... 85

Figure 36. Temperature dependence of average effective interdiffusion coefficients for Al, Co, Cr, Fe, Ni, and Mn in BCC $Al_{48}Ni_{52}$ end member alloy measured using $Al_{48}Ni_{52}$ vs. $Co_{20}Cr_{20}Fe_{20}Ni_{20}Mn_{20}$ diffusion couples in temperature range from 900 to 1200°C. 86

Figure 37. Comparison of average effective interdiffusion coefficients of (a) Co, (b) Cr, (c) Fe, (d) Ni, (e) Al, and (f) Mn in various FCC alloys 88

Figure 38. Comparison of average effective interdiffusion coefficients of (a) Co, (b) Cr, (c) Fe, (d) Ni, and (e) Al in various BCC alloys 89

Figure 39. Concentration profiles in CoCrFeNi system. (a.1) Spike profile at 900°C superimposed on the interdiffusion profile of Ni, (a.2) corresponding Gaussian fitted subtracted profile in (a.1). (b.1) Spike profile at 950°C superimposed on the interdiffusion profile of Ni, (b.2) corresponding Gaussian fitted subtracted profile in (b.1). (c.1) Spike profile at 1000°C superimposed on the interdiffusion profile of Ni, (c.2) corresponding Gaussian fitted subtracted profile in (c.1)..... 92

Figure 40. Concentration profiles in CoCrFeNiMn system. (a.1) Spike profile at 900°C superimposed on the interdiffusion profile of Ni, (a.2) corresponding Gaussian fitted subtracted

profile in (a.1). (b.1) Spike profile at 950°C superimposed on the interdiffusion profile of Ni, (b.2) corresponding Gaussian fitted subtracted profile in (b.1). (c.1) Spike profile at 1000°C superimposed on the interdiffusion profile of Ni, (c.2) corresponding Gaussian fitted subtracted profile in (c.1) 94

Figure 41. Concentration profiles in $Al_{0.25}CoCrFeNi$ system. (a.1) Spike profile at 900°C superimposed on the interdiffusion profile of Ni, (a.2) corresponding Gaussian fitted subtracted profile in (a.1). (b.1) Spike profile at 950°C superimposed on the interdiffusion profile of Ni, (b.2) corresponding Gaussian fitted subtracted profile in (b.1). (c.1) Spike profile at 1000°C superimposed on the interdiffusion profile of Ni, (c.2) corresponding Gaussian fitted subtracted profile in (c.1) 96

Figure 42. Comparison of tracer diffusion coefficient of Ni in $CoCrFeNi$, $CoCrFeNiMn$ and $Al_{0.25}CoCrFeNi$ alloys measured in present study 98

Figure 43. Comparison of tracer diffusion coefficient of Ni in various FCC alloys as a function of temperature. 99

Figure 44. Excess entropy as a function of normalized potential energy fluctuations. 100

Figure 45. Schematic illustration of the potential energy landscape (PEL) for ideal mixing, low entropy alloys, high entropy alloy and glass forming alloy..... 103

Figure 46. Normalized potential energy fluctuation as a function of temperature in $FeNi$, $FeCrNi$, $CoCrFeNi$, $CoCrFeNiMn$, $Al_{0.25}CoCrFeNi$ and Viterloy 4 104

Figure 47. Tracer diffusion coefficient as a function of temperature in CoCrFeNi, CoCrFeNiMn, Al _{0.25} CoCrFeNi and Viterloy4.	106
Figure 48. Tracer diffusion coefficient as a function normalized potential energy fluctuation (p) in CoCrFeNi, CoCrFeNiMn, Al _{0.25} CoCrFeNi and Viterloy4.	107
Figure 49. X-ray diffraction pattern of Al ₄₈ Ni ₅₂ alloy.	113
Figure 50. X-ray diffraction pattern of Co ₅₀ Ni ₅₀ alloy.	114
Figure 51. X-ray diffraction pattern of Fe ₅₀ Cr ₅₀ alloy.	114
Figure 52. X-ray diffraction pattern of Co ₂₅ Cr ₂₅ Fe ₂₅ Ni ₂₅ alloy.	115
Figure 53. X-ray diffraction pattern of Co ₂₀ Cr ₂₇ Fe ₃₃ Ni ₂₀ alloy.	115
Figure 54. X-ray diffraction pattern of Co ₃₀ Cr ₂₀ Fe ₂₀ Ni ₃₀ alloy.	116
Figure 55. X-ray diffraction pattern Co ₂₀ Cr ₂₀ Fe ₂₀ Ni ₂₀ Mn ₂₀ alloy.....	116
Figure 56. X-ray diffraction pattern of Co ₂₅ Cr ₂₅ Ni ₂₅ Fe ₁₅ Mn ₁₀ alloy.....	117
Figure 57. X-ray diffraction pattern of Co ₂₅ Cr ₂₅ Ni ₂₅ Fe ₁₅ Mn ₁₀ alloy.....	117
Figure 58. X-ray diffraction pattern of Al ₆ Co ₂₈ Cr ₁₉ Fe ₁₉ Ni ₂₈ alloy.....	118
Figure 59. X-ray diffraction pattern of Al ₆ Co ₂₈ Cr ₁₉ Fe ₁₉ Ni ₂₈ alloy.....	118

LIST OF TABLES

Table 1. Literature on diffusion based studies in HEAs.	10
Table 2. Parameters used to generate the concentration profiles with constant thin film thickness.	27
Table 3. Parameters used to generate the concentration profiles with constant D/D^* ratio	27
Table 4. Target compositions of alloys employed in this study.	33
Table 5. Diffusion couples employed for interdiffusion study.	37
Table 6. “Sandwich” thin film diffusion couples employed for tracer diffusion study.	38
Table 7. Binary enthalpy of mixing calculated by Miedema’s model for atomic pair between elements i and j in various Co-Cr-Fe-Ni based alloy systems.	58
Table 8. Compositions of $Al_pCo_qCr_rFe_sNi_t$ alloy corresponding to the maximum solubility limit of Al.....	58
Table 9. Compositions of $Al_pCo_qCr_rFe_sNi_tMn_u$ alloy corresponding to the maximum solubility limit of Al.....	59
Table 10. Average effective interdiffusion coefficients, activation energy and pre-exponential factor of Co, Cr, Fe, and Ni measured in FeCr (BCC) and CoNi (FCC) phases measured using $Fe_{50}Cr_{50}$ vs. $Co_{50}Ni_{50}$ diffusion couples	67

Table 11. Average effective interdiffusion coefficients, activation energy and pre-exponential factor of Co, Cr, Fe and Ni in CoCrFeNi alloy for the near equiatomic composition measured using $\text{Co}_{20}\text{Cr}_{27}\text{Fe}_{33}\text{Ni}_{20}$ vs $\text{Co}_{30}\text{Cr}_{20}\text{Fe}_{20}\text{Ni}_{30}$	71
Table 12. Average effective interdiffusion coefficients, activation energy and pre-exponential factor of Co, Cr, Fe and Ni in CoCrFeNiMn alloy for the near equiatomic composition measured using $\text{Co}_{25}\text{Cr}_{25}\text{Ni}_{25}\text{Fe}_{15}\text{Mn}_{10}$ vs $\text{Co}_{15}\text{Cr}_{15}\text{Ni}_{15}\text{Fe}_{25}\text{Mn}_{30}$ diffusion couples.....	74
Table 13. Average effective interdiffusion coefficients, activation energy and pre-exponential factor of Al, Co, Cr, Fe and Ni in $\text{Al}_{0.25}\text{CoCrFeNi}$ alloy composition measured using $\text{Al}_6\text{Co}_{19}\text{Cr}_{28}\text{Fe}_{28}\text{Ni}_{19}$ vs. $\text{Al}_6\text{Co}_{28}\text{Cr}_{19}\text{Fe}_{19}\text{Ni}_{28}$ diffusion couples.	77
Table 14. Average effective interdiffusion coefficients, activation energy and pre-exponential factor of Al, Co, Cr, Fe and Ni in BCC $\text{Al}_{48}\text{Ni}_{52}$ and FCC $\text{Co}_{25}\text{Cr}_{25}\text{Fe}_{25}\text{Ni}_{25}$ end member alloy measured using $\text{Al}_{48}\text{Ni}_{52}$ vs $\text{Co}_{25}\text{Cr}_{25}\text{Fe}_{25}\text{Ni}_{25}$ diffusion couples.....	80
Table 15. Average effective interdiffusion coefficients, activation energy and pre-exponential factor of Al, Co, Cr, Fe, Ni, and Mn in BCC $\text{Al}_{48}\text{Ni}_{52}$ and FCC $\text{Co}_{20}\text{Cr}_{20}\text{Fe}_{20}\text{Ni}_{20}\text{Mn}_{20}$ end member alloy measured using $\text{Al}_{48}\text{Ni}_{52}$ vs $\text{Co}_{20}\text{Cr}_{20}\text{Fe}_{20}\text{Ni}_{20}\text{Mn}_{20}$ diffusion couples.....	84
Table 16. Comparison of average effective interdiffusion coefficients of Fe, Cr, and Ni at 1100°C in FeCrNi alloy with average effective interdiffusion coefficients of Cr, Fe, Co, and Ni in CoCrFeNi, CoCrFeNiMn and $\text{Al}_{0.25}\text{CoCrFeNi}$ alloys.	91
Table 17. Tracer diffusion coefficient of Ni in CoCrFeNi alloy.	93
Table 18. Tracer diffusion coefficient of Ni in CoCrFeNiMn alloy.	95

Table 19. Tracer diffusion coefficient of Ni in Al _{0.25} CoCrFeNi.....	97
Table 20. Atomic radius and bulk modulus of various elements.....	101
Table 21. Binary enthalpy of mixing calculated by Miedema's model for atomic pair between element <i>i</i> and <i>j</i> [52].	102
Table 22. Thermodynamic parameters measured at 1000°C f or equiatomic alloy composition	102
Table 23. Compositions and lattice parameter of the alloys prepared for present study	112
Table 24. Lattice parameters and crystal structure of the alloys determined using X-ray diffraction	119

CHAPTER 1 INTRODUCTION

1.1 General Background

Metallic alloys for most engineering application are designed near one of the terminal end of the multi-component phase diagram with a primary solvent, as shown in Figure 1(a) [1]. Examples of such an alloy systems are Co based superalloys, Ni based superalloys, steels, and various commercial Al based alloys (e.g. 5083, 6061, 7075 etc.). Such an alloy systems are typically referred to as multicomponent alloys where one of the constituent elements are typically present more than 50 at.% (i.e. solvent) while other elements are present as minor constituents (i.e. solute). In most of the engineering alloys, concentration of solvent usually exceeds more than 90 at. %.

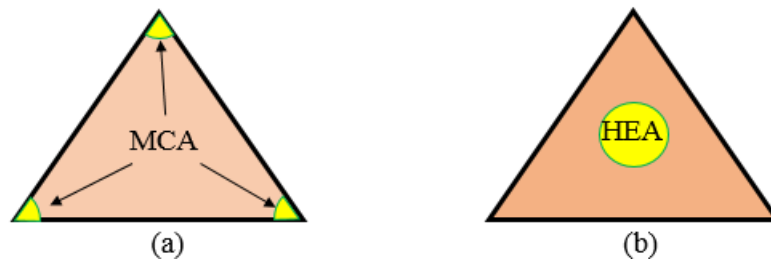


Figure 1. Example of alloy design in (a) traditional multicomponent alloy (MCA), and (b) High Entropy alloy (HEA)

Based on multicomponent alloy system, new class of the alloys called High Entropy alloys (HEAs) were first brought to the attention in the year 2004 [2, 3], although this new class of material was first patented in the year 2002 [4]. HEAs typically refer to a family of alloys that contain near equiatomic (5-35 at.%) composition of minimum four principal elements with high

(maximum) configurational entropy. From alloy design standpoint, alloys compositions of HEAs lie approximately in the middle of the multicomponent phase diagram, as shown in Figure 1(b). The term high entropy refers to the magnitude of a mixing entropy in an alloy system, given by [5]:

$$\Delta S_{\text{mix}} = -R \sum_{i=1}^n (X_i \ln X_i) \quad (1)$$

where, R is the ideal gas constant, X_i is the mole fraction of the constituent elements. In general, a multicomponent alloy typically has one principal elements forming the solvent, and other elements as solute. Therefore, the overall configurational entropy of multicomponent alloys is relatively low. Figure 2 shows the alloys classification based on magnitude of configurational entropy. Generally, configurational entropy of mixing greater than $1.5R$ is adopted as the minimum entropy requirement for an alloy to be classified as HEA.

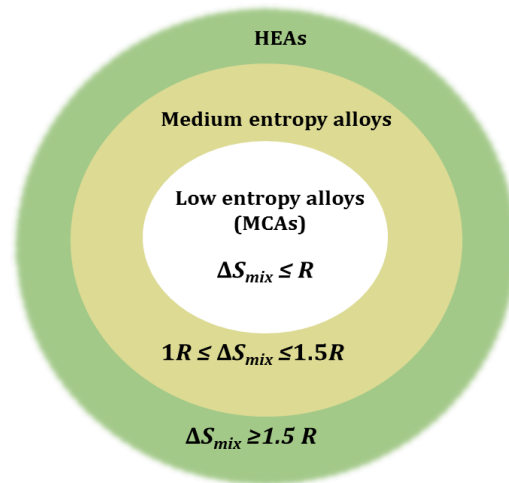


Figure 2. Entropy based classification of alloys

Due to the presence of many elements in equiatomic or near-equiatomic composition, these HEAs are sometimes also referred to as multi-principal element alloys (MPEAs) or Complex concentrated alloys (CCAs). These nomenclature are based on the fact that there is no identifiable solvent in these alloys, and all the elements are present as principal alloying additions [6]. HEAs, MPEAs and CCAs are now-a-days used interchangeably, but strictly speaking HEAs are associated with the alloys which exhibit single phase solid solutions microstructure while MPEAs or CCAs are broader terms which allows the formation of multiphase microstructure, including intermetallic phases, in the alloy [6].

HEAs were initially postulated to exhibit four *core effects*, i.e. high-entropy effect [2], lattice distortion effect, sluggish diffusion effect [7], and cocktail effect [8]. Except cocktail effect, all other core effects may not be significant as was first proposed [9]. Various researchers [6, 9], have casted a doubt on these core effects. Based on various observations these core effects cannot be generalized for all the HEAs.

1.2 Motivation

Extensive investigations have been carried out in past two decades on improving the physical and mechanical properties of HEAs, along with some specific focus on thermodynamics and precipitation kinetics of second phase. However, limited efforts were made to validate the proposed *core effects* in HEAs. These core effects are also considered as a founding principles of HEAs, therefore, it become imperative to validate the applicability of these fundamental core effects for most commonly used/studied HEAs, if not for all HEAs. Out of the aforementioned

four core effects, high entropy effect and sluggish diffusion effects are the two most debatable core effects. Therefore the present dissertation will investigate these two core effects in transition metal HEAs.

Among transition metal HEAs, CoCrFeNi based HEAs are most commonly investigated HEAs. In fact, the first HEA, developed by Brian Cantor, also called Cantor alloy ($\text{Co}_{20}\text{Cr}_{20}\text{Fe}_{20}\text{Ni}_{20}\text{Mn}_{20}$) is also based on CoCrFeNi alloys [3]. Therefore, present dissertation investigate the high entropy effect in AlCoCrFeNi and AlCoCrFeNiMn HEAs, and sluggish diffusion effects in CoCrFeNi, CoCrFeNiMn, $\text{Al}_{0.25}\text{CoCrFeNi}$ alloys.

1.3 Objective

In present dissertation, high throughput combinatorial diffusion couple approach was employed to investigate the two of fundamental core effects, i.e. high entropy and sluggish diffusion effect, which will improve the present understanding of HEAs. In diffusion couples, composition gradient was generated after high temperature interdiffusion, which allowed to study many composition of HEAs using single experiment. The two-fold objective of present dissertation are:

1. **Experiments to investigate High entropy effect:** *High entropy effect* is purely based on entropic stabilization of phases due to high configurational entropy due to the large number of constituent elements. To study this effect, $\text{Al}_{48}\text{Ni}_{52}$, $\text{Co}_{25}\text{Cr}_{25}\text{Fe}_{25}\text{Ni}_{25}$, $\text{Co}_{20}\text{Cr}_{20}\text{Fe}_{20}\text{Ni}_{20}\text{Mn}_{20}$ were fabricated in the using arc-melting and diffusion couple were fabricated between $\text{Al}_{48}\text{Ni}_{52}$ vs. $\text{Co}_{25}\text{Cr}_{25}\text{Fe}_{25}\text{Ni}_{25}$ and $\text{Al}_{48}\text{Ni}_{52}$ vs. $\text{Co}_{20}\text{Cr}_{20}\text{Fe}_{20}\text{Ni}_{20}\text{Mn}_{20}$ at several temperature. Various

composition of off-equiatomic quinary AlCoCrFeNi and senary AlCoCrFeNiMn were generated in the temperature range from 900° to 1200°C, as presented in Chapter 5. Solubility limit of Al in off-equiatomic $Al_pCo_qCr_rFe_sNi_t$ and $Al_pCo_qCr_rFe_sNi_tMn_u$ alloys, with lower entropy, were directly measured as a function of temperature, and compared with solubility limit of Al in equiatomic $Al_xCoCrFeNi$ and $Al_xCoCrFeNiMn$, with higher entropy, determined from equilibrium phase diagrams. Contributions from various thermodynamic parameters, i.e. ΔH_{mix} and $-T\Delta S_{mix}$ towards the overall stability, i.e. ΔG_{mix} , of the alloys were determined to assess the high entropy effects in the alloys.

2. Experiments to investigate Sluggish diffusion effect: *Sluggish diffusion* hypothesis in HEAs is based on the fact that the formation of new phases in HEA requires cooperative diffusion of many different kinds of atoms to accomplish the partitioning, which is difficult to achieve. Consequently, diffusion in HEAs has been proposed to be anomalously slow or sluggish. This postulation was experimentally examined in three different face centered cubic HEAs (i.e. CoCrFeNi, CoCrFeNiMn and AlCoCrFeNi) system, as presented in Chapter 6. Tracer diffusion and interdiffusion coefficients in CoCrFeNi based HEAs were measured to elucidate the sluggish diffusion, if any, in HEAs. Diffusion coefficients was compared to the diffusion coefficient reported for traditionally-defined multicomponent alloys. Concepts of potential energy landscape was used to understand the diffusion process in HEAs, and fluctuations in lattice potential energy and resulting reduction in entropy (i.e. excess entropy) was examined using potential energy fluctuation (PEF) model [10]. Tracer diffusion coefficients of constituent elements in HEA system was correlated with excess entropy and potential energy fluctuation of the HEA systems.

CHAPTER 2 LITERATURE REVIEW

2.1 Core effects in High Entropy alloys

Based on initial work by Yeh and co-workers [11], HEAs were proposed to exhibit four core effects. Due to high entropy of mixing, overall Gibb's free energy of mixing, given by Equation 2, is lowered. High entropy phases, e.g. random/disordered solid solution phases, tend to stabilize in comparison to low entropy phases, e.g. intermetallic phases.

$$\Delta G_{\text{mix}} = \Delta H_{\text{mix}} - T\Delta S_{\text{mix}} \quad (2)$$

This *high entropy effect* is purely based on entropic stabilization of phases due to high configurational entropy due to the large number of constituent elements. Due to this high entropy effect, alloy compositions forming single phase solid solution with high entropy of mixing (i.e. equiatomic alloys) should be more stable than alloys of similar constituent elements with lower entropy of mixing. In practice, theory of entropic stabilization of phases due to high configurational entropy fails to explain the multiple phases in various experimental alloys, e.g. AlCoCrFeNi [12], AlCoCrFeNiMn [13], CoCrFeNiMo [14] etc, near equiatomic composition. It can be intuitively understood by the simple fact that merely replacing any constituent element of single phase HEA with any random non-constituent element would not ensure the formation of single phase solid solution, e.g. replacing Mn with either Al or Mo from CoCrFeNiMn single phase FCC type HEA. Therefore, entropy of mixing alone may not always results in lower Gibbs free energy [15]. Otto *et al.* [16] also suggested that increased configurational entropy may not stabilize the single phase in all alloys, as effect may not be sufficient enough to overcome the driving forces

that favor the formation of secondary phases. But recent studies [16, 17] suggest that enthalpy of mixing also plays an important role in the stabilization of these HEAs. Also, it has been argued that almost all HEAs, when subjected to appropriate heat treatment, would decompose into multiple phases [9]. This hypothesis does not place any general restriction on what is required for solid solution formation, i.e. Hume-Rothery rules.

In HEA, every atom can be surrounded by different types of atoms, and therefore suffers lattice strain due to the difference in atomic size. Large differences in atomic size would favor the formation of intermetallic compounds rather than single phase solid solution, based on Hume-Rothery rules. Therefore, high entropy effect would not coexist with *lattice distortion effect* in HEA. Experimentally, it has been observed that HEA does not have lattice distortion more than 5% of the lattice parameter [9].

Unlike in conventional alloys, the formation of new phases in HEA requires cooperative diffusion of many different kinds of atoms to accomplish the partitioning. Consequently, diffusion in HEAs has been proposed to be anomalously slow or sluggish. This postulation is mainly motivated by the indirect observation of nanocrystals/amorphous phases upon solidifications and stable single-phase formation [2]. These indirect observations may support the *sluggish diffusion effect*, which Yeh *et al.* [18-21] initially hypothesized: sluggish diffusion arises from the fluctuations in lattice potential energy of the diffusing element. However, various evidence exists [9], such as precipitation during quenching that do not support this hypothesis.

Ranganathan [8] was the first to call HEAs as “*multimetallic cocktail*” owing to their unusual attractive properties. Properties not only come from the basic properties of elements by

the rule of mixture, but also from the mutual interactions among all the elements. Due to the complexity in compositions, unusual non-linear behavior could be expected due to different interactions between neighboring elements. This effect has not been investigated quantitatively.

2.2 Sluggish Diffusion in High Entropy alloys

Sluggish diffusion in HEA was first reported by Yeh *et al.* [21] based on experimental results and analyzed with fluctuations in potential energies of lattice sites in CoCrFeMn_{0.5}Ni. They suggested that different bond strengths and atomic size mismatch of constituent elements in HEAs gave rise to fluctuations in lattice potential energy (LPE). Greater fluctuations in LPE inhibits the diffusion process mainly because atoms would prefer to stay in atomic sites with lower LPE, i.e., atomic traps. If an atom jumps into a higher LPE site from lower LPE site, then the atom will have a tendency to revert the jump back to low LPE site. Sluggish diffusion hypothesis originates from this variation in lattice potential energy, leading to formation of atomic traps on lattice sites, which could inhibit the atomic diffusion [18]. Miracle and Senkov [6] compared the tracer diffusion coefficient of Ni in CoCrFeMn_{0.5}Ni alloy, with that in Fe-15Cr-20Ni stainless steel. Their analysis suggested that tracer diffusion coefficient in same temperature range, however, is slightly higher in HEA.

The sluggish diffusion hypothesis is sometimes purely interpreted based on microstructural observations [22, 23]. Pickering and Jones [9] casted doubt on the sluggish diffusion hypothesis based on the precipitates observed in an as-cast HEA. These precipitates were observed under different cooling rates, including furnace cooling and water quenching after high temperature heat

treatment, demonstrating a high rate of elemental redistribution even during quenching. Jones *et al.* [24] observed precipitation of Ni- and Al-rich B2 precipitates in Al_{0.5}CrFeCoNiCu after water quenching and air cooling, and concluded that the elemental redistribution kinetics was fast.

At present very few experimental or simulation studies have been reported to explore the interdiffusion or tracer diffusion in HEAs. Table 1 reports the all diffusion studies conducted till date. Ni tracer diffusion studies conducted by Vaidya *et al.* [25] in CoCrFeNi and CoCrFeNiMn alloys challenged the sluggish diffusion hypothesis. However, Zhao *et al.* [26] supported the sluggish diffusion effect, based on density functional theory (DFT) simulation, that calculated the tracer diffusion coefficients in Ni based alloys. Middleburgh *et al.* [27] reported high vacancy formation energy in CoCrFeNi alloys using DFT approach, however, DFT calculations have been demonstrated to overestimate the energy of vacancy formation [28]. Experimental data is important in understanding the diffusion process in HEAs. However, it is challenging to measure intrinsic and interdiffusion coefficient in quaternary or higher systems. In fact, since the conceptual discovery of HEAs in 1995 [29], although patented in 2002 [4] and named in 2004 [2], it took almost 18 years to conduct the first experiment to measure the diffusion coefficient in 2013 [21]. Limited experimental diffusion data can be attributed to the difficulty in quantifying the diffusion coefficients in HEAs, because of complexity having many principal elements. Due to limited available diffusion database, it is difficult to substantiate the originally proposed hypothesis of sluggish diffusion in HEAs.

Table 1. Literature on diffusion based studies in HEAs.

HEA system	Study	Approach	Conclusion	Reference
CoCrFeNiMn	Experimental	Pseudo-binary	Sluggish	[21]
CoCrFeNi	Experimental	Interdiffusion experiments	-	[30]
CoCrFeNiMn (Theoretical)	Theoretical	Empirical rules	Sluggish	[31]
AlCoCrFeNi (FCC)	Experimental	Darken Manning Formalism	Sluggish	[32]
CoCrFeNi/CoCrFeNiMn	Experimental	Radiotracers	Non-sluggish at absolute temperatures	[25]
CoCrFeNiMn _{0.5}	Theoretical	Moleko, Allnatt, and Allnatt (MAA) light approach	Sluggish	[33]
CoCrFeNiMn	Experimental/ Theoretical	Interdiffusion (Manning Formalism)	-	[34]
CoCrFeNiMn _{0.5}	Theoretical	MAA light approach	Sluggish	[35]
CoCrFeNi/CoCrFeNiMn	Experimental	Radiotracers	Non-sluggish (grain boundary diffusion)	[36]
CoCrFeNi/CoCrFeNiMn	Experimental	Radiotracers	Non sluggish	[37]
CoCrFeNi/CoCrFeNiMn	Experimental	Self diffusion	Non sluggish	[38]
CoCrFeNiMn	Experimental	Radiotracer (Belova-Sohn-Murch Formalism)	-	[39]
Ni-CoCrFeMn	Experimental	Tracer diffusion	Non sluggish	[40]

2.3 Diffusion Coefficients

Diffusion can occur in the presence of chemical potential gradient (i.e., typically represented by concentration gradient), and in homogeneous systems (i.e., self diffusion). Tracer diffusion coefficient represents diffusion in the absence of concentration gradient, and interdiffusion coefficient describes chemical diffusion under a concentration gradient.

2.3.1 Interdiffusion coefficients

Onsager formalism [41] based on irreversible thermodynamics is generally used to understand the interdiffusion flux in multicomponent system. The general expression of interdiffusion coefficient in an n-component system is given by:

$$\tilde{J}_i = - \sum_{j=1}^{n-1} \tilde{D}_{ij}^n \frac{\partial C_j}{\partial x} \quad (i = 1, 2, \dots, n - 1) \quad (3)$$

where \tilde{D}_{ij}^n are the interdiffusion coefficients, and $\frac{\partial C_j}{\partial x}$ is concentration gradient of component j.

Interdiffusion flux at any plane x can be determined without the knowledge of interdiffusion coefficients from the concentration profiles using following relationship [42]:

$$\tilde{J}_i = \frac{1}{2t} \int_{C_i(\pm\infty)}^{C_i(x)} (x-x_0) dC_i \quad (i = 1, 2, \dots, n - 1) \quad (4)$$

When the variation of molar volume is negligible with composition, extension of Boltzmann – Matano analysis in multicomponent system is employed to measure the interdiffusion coefficients [43] as expressed by:

$$\int_{C_i(\pm\infty)}^{C_i(x)} (x-x_0)dC_i = -2t \sum_{j=1}^{n-1} \tilde{D}_{ij}^n \frac{\partial C_j}{\partial x} \quad (i = 1, 2, \dots, n - 1) \quad (5)$$

This method will require a precise of location of Matano plane (x_0), which could be determined by the following relation:

$$\int_{C_i(-\infty)}^{C_i(+\infty)} (x-x_0)dC_i = 0 \quad (6)$$

Measurement of interdiffusion coefficients using the above Boltzmann-Matano method is challenging for quaternary or higher systems. For instance, in a quinary system, four independent compositional gradients are correlated with four independent interdiffusion fluxes. In order to determine the full matrix of sixteen interdiffusion coefficients at fixed composition, four diffusion couple experiments are necessary. Simply conducting these diffusion couple experiment will not ensure the successful determination of interdiffusion coefficients, because diffusion paths of four diffusion couples must intersect at a single composition in the five-dimensional compositional space of Gibbs pentahedron. Therefore, the probability of having a common intersection from four diffusion paths is practically zero.

Dayananda and Sohn outlined two methods to measure relatively simplified representations of interdiffusion coefficients with a single diffusion couple experiment. First, average effective interdiffusion coefficients [44] for multicomponent system can be measured for any component over a desired composition range. The average effective interdiffusion coefficient on either side of the Matano plane can be determined by:

$$\int_{x_1}^{x_2} \tilde{J}_i dx = -\bar{D}_i^{\text{eff}} (C_i(x_1) - C_i(x_2)) = -\frac{1}{2t} \int_{C_i(x_1)}^{C_i(x_2)} (x-x_0)^2 dC_i \quad (i = 1, 2, \dots, n) \quad (7)$$

where $\bar{D}_{i,R}^{\text{eff}}$ represents the average effective interdiffusion coefficient of component i on right hand side of the matano plane. The average effective interdiffusion coefficient represents one \bar{D} number for one component. It does not give any information about the main and cross-interdiffusion coefficients.

Second, average multicomponent interdiffusion coefficients, which individually represents an average value of main and cross interdiffusion coefficients over desired composition range [45] can be written as:

$$\int_{x_1}^{x_2} \tilde{J}_i (x-x_0)^p dx = - \sum_{j=1}^{n-1} \bar{D}_{ij}^n \int_{C_j(x_1)}^{C_j(x_2)} (x-x_0)^p dC_j \quad (i = 1, 2, \dots, n) \quad (8)$$

where, \bar{D}_{ij}^n represents the average interdiffusion coefficient of component i and concentration gradient dC_j . By varying the value of p in Equation 8, this analysis can be extended to measure the average multicomponent interdiffusion coefficients in quaternary and higher order HEAs.

Kulkarni and Chauhan [30] employed this approach to study the interdiffusion in Fe-Ni-Co-Cr alloys.

2.3.2 Tracer diffusion coefficient

Radioactive tracers are typically employed to track the movement of atoms. For tracer diffusion measurement, a thin layer of radioactive isotopes of element of interest (say, A*) is deposited on the alloy surface. Then, the alloy is isothermally annealed for a time. The annealed alloy is then serial sectioned in thin slices and intensity of radiation emitted by radioactive isotopes is measured at different penetration depths. Alternatively, secondary ion mass spectroscopy (SIMS) profiling could also be performed to determine the concentration as a function of penetration depth. A thin film solution is applicable in this case, expressed by following Gaussian solution:

$$C(x,t) = \frac{C_0 \Delta x}{\sqrt{4\pi D_i^* t}} \exp\left(-\frac{x^2}{4D_i^* t}\right) \quad (9)$$

where, $\Delta x \ll \sqrt{D_i^* t}$, $C(x,t)$ is the time dependent concentration at depth x , C_0 is the initial tracer concentration, Δx represents thickness of tracer thin film and D_i^* is the tracer diffusion coefficient. Recently, Vaidya *et al.* [25] utilized this approach to measure the Ni tracer diffusion coefficients in CoCrFeNi and CoCrFeNiMn alloys. In general, tracer diffusion coefficient (D_i^*) is related to the self-diffusion coefficient (D_i), by a correlation factor (f), given by:

$$f = \frac{D_i^*}{D_i} \quad (10)$$

Based on linear response theory coupled with Boltzmann–Matano method, Belova *et al.* [46] developed a mathematical formalism, to measure the tracer diffusion coefficient in multicomponent alloys using traditional diffusion couple experiments. Instead of application of radiotracers, this formalism uses the same type atoms (X) sandwiched as a thin film between two alloys with different compositions on either side. Sandwich type diffusion couple arrangement is used to include both standard interdiffusion and thin film diffusion in the same experiment. Experimentally, three alloy discs are stacked in a sequence such that first alloy (say, A₁) is sandwiched between two same alloys (say, A₂) and one of the interfaces between A₁ and A₂ has a thin film of metal (say, X), for which tracer diffusion coefficient will be measured. Figure 3 schematically illustrates the stacking sequence used for the experimental measurement of tracer diffusion coefficient. Isothermal annealing of the sandwich diffusion couple will create the spike in the concentration profile of the thin film metal (X). At the spike interface, shown in Figure 3, the spike profile (say, X₁+X₂) includes the concentration profile due to both interdiffusion (X₁) and thin film diffusion (X₂). The concentration profile due to tracer movement (X₂) could be extracted by simple mathematical subtraction of interdiffusion profile (X₁), measured at the interdiffusion interface, from spike profile (X₁+X₂), measured at the spike interface. In comparison to traditional radiotracer experiment, X₂ acts as an isotope tracer in sandwich diffusion couple experiment to measure tracer diffusion coefficient. Tracer diffusion coefficient could be measured using the Belova *et al.* [46] mathematical formalism, given by:

$$D_A^* = - \left(\frac{(x+a)}{2t} + \tilde{D} \frac{d \ln c_{X2}}{dx} \right) / \left(\frac{d \ln (c_{X1}/c_{X2})}{dx} \right) \quad (11)$$

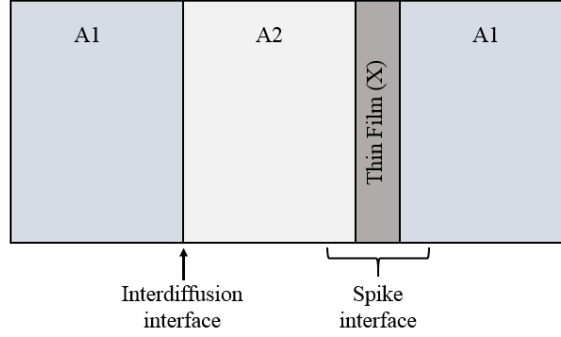


Figure 3. Configuration of alloys in sandwich type arrangement for measurement of tracer diffusion coefficient.

Schulz *et al.* [47] experimentally implemented Belova's mathematical formalism for the first time to measure concentration dependent tracer diffusion coefficient in binary Cu-Ni system. Schulz *et al.* [47] demonstrated that formalism cannot be relied for the accurate of measurement of composition-dependence tracer diffusion coefficient as *formalism approximately estimates the tracer diffusion coefficient, however did not give the reliable composition dependence.* Alternatively, Gaussian distribution function can be used to measure the diffusion coefficients for the composition of interest. Equation 12 represents the Gaussian distribution function, typically used to curve fit the tracer concentration profile (X_2).

$$f(x) = A \exp \left[- \frac{(x-b)^2}{2c^2} \right] \quad (12)$$

where, A represents the height of the peak of Gaussian distribution function, b is the position of the center of Gaussian distribution function and c is the standard deviation (σ). On comparing the exponential part of thin film solution for sandwich geometry (Equation 9) and Gaussian distribution function (Equation 12) for origin as a the peak's position:

$$\exp\left(-\frac{x^2}{4D^*t}\right) = \exp\left[-\frac{1}{2}\left(\frac{x-0}{c}\right)^2\right] \quad (13)$$

$$4D^*t = 2c^2 \quad (14)$$

$$D^* = \frac{c^2}{2t} \quad (15)$$

Most of the statistical curve fitting programs does not provide the c parameters. Therefore, the constant c needs to be expressed in some readily measurable quantity. Using simple geometrical analysis c can be expressed in other measureable quantity, e.g. full width at half maxima (FWHM) of Gaussian distribution function. In statistical terms, Gaussian distribution function can be expressed in terms of position (x), mean (μ) and standard deviation (σ) as :

$$f(x,\mu,\sigma) = \frac{1}{\sigma\sqrt{2\pi}} \exp\left[-\frac{1}{2}\left(\frac{x-\mu}{\sigma}\right)^2\right] \quad (16)$$

FWHM is measured at the half maxima position (say α) as shown in Figure 4 , therefore

$$\frac{1}{2}f(x_{\max}) = \frac{1}{\sigma\sqrt{2\pi}} \exp\left[-\frac{1}{2}\left(\frac{\alpha-\mu}{\sigma}\right)^2\right] \quad (17)$$

Maxima occurs at $x = \mu$

$$\frac{1}{2} \frac{1}{\sigma\sqrt{2\pi}} = \frac{1}{\sigma\sqrt{2\pi}} \exp\left[-\frac{1}{2}\left(\frac{\alpha-\mu}{\sigma}\right)^2\right] \quad (18)$$

On solving Equation 18 for the roots of α

$$\alpha = \pm \sigma\sqrt{2\ln 2} + \mu \quad (19)$$

Therefore, FWHM can be represented as the difference between two roots of α as:

$$\text{FWHM} = \alpha_2 - \alpha_1 = \sigma 2\sqrt{2\ln 2} \quad (20)$$

$$c = \sigma = \frac{\text{FWHM}}{2\sqrt{2\ln 2}} \quad (21)$$

On substituting the value of c in Equation 15, Tracer diffusion coefficient can be expressed as:

$$D^* = \frac{\text{FWHM}^2}{(16\ln 2)t} \quad (22)$$

Schulz et al. [47] had successfully validated the applicability of the Equation 22 for the measurement of Tracer diffusion coefficient in binary Cu-Ni system.

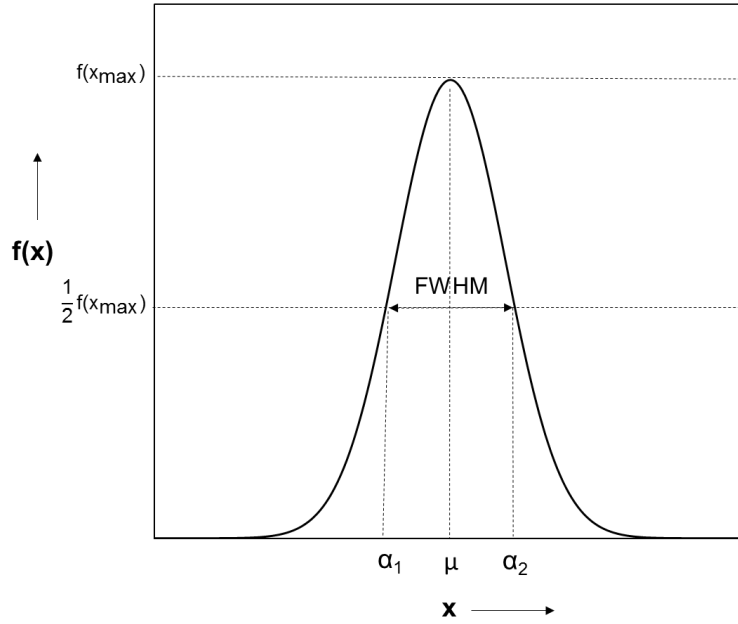


Figure 4. Geometrical representation of Gaussian distribution function

2.4 Potential energy fluctuation model

He *et al.* [10] demonstrated that ideal entropy of mixing (ΔS_{mix}) overestimates the entropy of mixing due to a correlation effect between constituent elements. This correlation depends on the difference in bond strengths and atomic size mismatch. A significant correlation effect in an alloy system give rise to a larger variation in lattice potential energy (LPE) and excess entropy (S_E). Using the statistical thermodynamics, He *et al.* [10] developed a phenomenology to describe excess configurational entropy by considering the general effects of potential energy fluctuations, given by:

$$S_E = k_B \times \left[1 + \frac{p}{2} - \ln(p) + \ln(1 - e^{-p}) - \frac{p}{2} \times \frac{1 + e^{-p}}{1 - e^{-p}} \right] \quad (23)$$

where, $p = \frac{\Delta E}{k_B T}$ is the normalized energy fluctuation and $\Delta E = (E_{\max.} - E_{\min.})$ represents the range of the potential energy fluctuation. In general, the correlated configurational entropy of mixing (S_{corr}) can be written as:

$$S_{\text{corr}} = \Delta S_{\text{mix}} + S_E \quad (24)$$

Therefore, the final expression for the entropy under correlated mixing, based on Equation 23 and Equation 24 can be written as [10]:

$$S_{\text{Corr}} = -k_B \sum_{i=1}^n (X_i \ln X_i) + k_B \times \left[1 + \frac{p}{2} - \ln(p) + \ln(1 - e^{-p}) - \frac{p}{2} \times \frac{1 + e^{-p}}{1 - e^{-p}} \right] \quad (25)$$

Pertaining to HEAs, potential energy fluctuation (x) could arise from the atomic size mismatch and chemical bond misfit. Lattice distortion, due to different atom sizes in HEA, would create an internal strain field (intrinsic residual strain). This fluctuation would create disturbance in configurational space and consequently reduce the configurational entropy [10, 48, 49]. Normalized energy fluctuation due to intrinsic residual strain can be expressed as:

$$p_e = 4.12 \delta \times \sqrt{\frac{\bar{K}\bar{V}}{k_B T}} \quad (26)$$

where, $\delta = \sqrt{\sum_{i=1}^n X_i \left(1 - \frac{r_i}{\sum X_i r_i}\right)^2}$ is the atomic size misfit, X_i is the composition of constituent elements, r_i is the atomic radius, \bar{K} is the composition-weighted average bulk modulus and \bar{V} is the composition-weighted average atomic volume.

Chemical interaction in the binary pair of the constituent elements could also give rise to potential energy fluctuation. Normalized energy fluctuation caused by the difference in chemical bond energy of various atomic pairs is given by [10]:

$$p_c = 2 \sqrt{\frac{\sqrt{\sum_i \sum_{j, i \neq j} X_i X_j (\Delta H_{ij}^{\text{mix}} - \bar{H})^2}}{k_B T}} \quad (27)$$

where, $\Delta H_{ij}^{\text{mix}}$ represents the binary enthalpy of mixing of element i and j , and \bar{H} is the average enthalpy of $\Delta H_{ij}^{\text{mix}}$. Therefore, total potential energy fluctuation (p) is given by the sum of potential energy fluctuation due to atomic size and chemical bond misfit, i.e. $p = p_e + p_c$:

$$p = 4.12 \delta \times \sqrt{\frac{\bar{K}\bar{V}}{k_B T}} + 2 \sqrt{\frac{\sqrt{\sum_i \sum_{j, i \neq j} X_i X_j (\Delta H_{ij}^{\text{mix}} - \bar{H})^2}}{k_B T}} \quad (28)$$

2.5 Solid-solution phase formation rule pertaining to HEAs

Hume-Rothery rules postulates the conditions under which elements show complete substitutional solid solubility in each other. Elements which comply these rules have similar atomic size, crystal structure, valency and electronegativity. Various researchers have mathematically extended the Hume-Rothery rules to multi component alloys. δ -parameter is adopted as a measure of mismatch in atomic size for multi-component alloys given by [50]:

$$\delta = \sqrt{\sum_{i=1}^n X_i \left(1 - \frac{r_i}{\sum X_i r_i}\right)^2} \quad (29)$$

where r_i is the atomic radius of i^{th} element. ΔH_{mix} is parameter used to predict the chemical compatibility among the constituent elements, given by:

$$\Delta H_{\text{mix}} = \sum_{i=1}^{n-1} \sum_{j=2, i < j}^n \Omega_{ij} X_i X_j \quad (30)$$

where, $\Omega_{ij} = 4 \times \Delta H_{ij}^{\text{mix}}$ is the regular solution interaction parameter between i^{th} and j^{th} elements. $\Delta H_{ij}^{\text{mix}}$ is the binary enthalpy of mixing of element i and j , which were estimated using the Miedema's macroscopic model for liquid binary alloy [51, 52]. ΔH_{mix} is an important predictor for the formation of disordered single phase solid solution. Alloys will exhibit the higher disordered solid solution formation tendency if the value of ΔH_{mix} for disordered single phase solid solution approaches zero. Recently, Yang and Zhang [53] describes the Ω - parameter, which accounts for the relative effects for enthalpy of mixing and entropy of mixing, given by [54]:

$$\Omega = \frac{T \Delta S_{\text{mix}}}{|\Delta H_{\text{mix}}|} \quad (31)$$

where, $\Delta S_{\text{mix}} (-R \sum X_i \ln X_i)$ is the Boltzmann entropy of mixing. In as-casts alloys, T is adopted as the melting temperature of the alloy, measured using simple rule of mixture. However in present study, alloy compositions were fabricated via diffusion under isothermal condition. Therefore, T is adopted as the temperature of annealing.

Difference in electronegativity ($\Delta\chi$) between constituent elements in HEA is measured as a root-mean square of composition-weighted average for the deviation in electronegativity from the mean value in HEAs as [50]:

$$\Delta\chi = \sqrt{\sum_{i=1}^n X_i \left(\chi_i - \sum_{i=1}^n X_i \chi_i \right)^2} \quad (i = 1, 2, \dots, n) \quad (32)$$

where, χ_i is the Pauling electronegativity of the i^{th} element. Electron concentration in HEAs can be measured as either valence electron concentration (VEC) or electron per atom (e/a ratio). VEC is typically considered as a more relevant parameter, than e/a ratio, as it represents more realistic electronic band structure when first principle band calculations are used in determination of fermi level [55]. VEC can be measured in HEAs as a composition-weighted average VEC value of the constituent elements [56]:

$$\text{VEC} = \sum X_i (\text{VEC})_i \quad (i = 1, 2, \dots, n) \quad (33)$$

CHAPTER 3 THEORETICAL VALIDATION OF FORMALISM TO MEASURE TRACER DIFFUSION COEFFICIENT

3.1 Concentration profiles

Error function solution can be used to generate the interdiffusion concentration profile given by:

$$C(x,t) = \frac{C_- + C_+}{2} + \frac{C_- - C_+}{2} \operatorname{erf}\left(\frac{x}{\sqrt{4\tilde{D}t}}\right) \quad (34)$$

where, C_- and C_+ are the terminal compositions of diffusion couple and \tilde{D} represents the interdiffusion coefficient. Aforementioned for multicomponent alloys (i.e. high entropy alloys) where number of constituents elements are typically more than four, measurement of interdiffusion coefficients are practically not feasible. In such cases, interdiffusion coefficients can be replaced by average effective interdiffusion coefficients (\tilde{D}_i^{eff}) measured by Dayanada-Sohn method [44], which represents the single nominal diffusion coefficient for each component in a given compositional range.

By assuming that film thickness is relatively thin (i.e., $\Delta x < \sqrt{D^*t}$) and interdiffusion of thin film do not contribute to the thickness of tracer diffusion profile, spike profile can be measured as the sum of interdiffusion and tracer diffusion given by:

$$C(x,t) = \frac{C_- + C_+}{2} + \frac{C_- - C_+}{2} \operatorname{erf}\left(\frac{x}{\sqrt{4\tilde{D}t}}\right) + \frac{C_0 \Delta x}{\sqrt{4\pi D^*t}} \exp\left(-\frac{x^2}{4D^*t}\right) \quad (35)$$

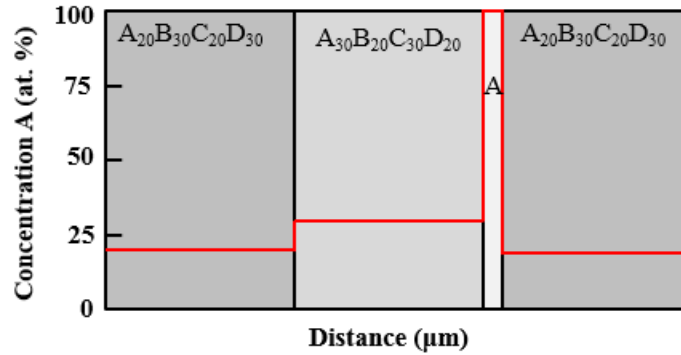
Curve fitting of Spike profile could be challenging using the regular sixth or seventh order polynomial functions, as these functions may underestimate the height of the spike concentration profile. Therefore, non-linear curve fitting function defined by the division of two third-order polynomials with seven fit parameters, given by Equation 36, can be used for the curve fitting of spike profile. This type of polynomial function yield satisfactory fit whenever concentration profile exhibits the uphill diffusion phenomena [57, 58].

$$c(x) = \frac{p_1 + p_2x + p_3x^2 + p_4x^3}{1 + p_5x + p_6x^2 + p_7x^3} \quad (36)$$

3.2 Validation

The main objective of this validations is to show the significance of the subtraction of interdiffusion concentration profile from spike concentration profile to extract the pure tracer diffusion concentration profile from subtraction method. Figure 5 schematically represents the diffusion couple arrangement and theoretical concentration profile before and after isothermal annealing in hypothetical quaternary ABCD alloy. In the diffusion couple, thicknesses of each alloy, both at spike and interdiffusion interface, is selected to maintain the semi-infinite boundary condition.

(a) Before annealing



(b) After annealing

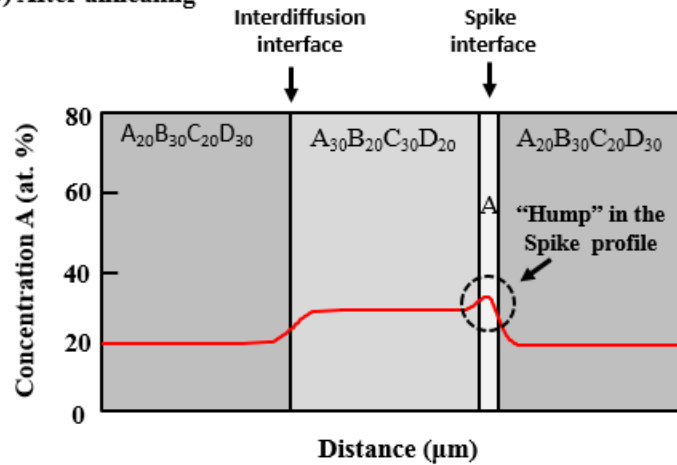


Figure 5. Schematic representation of diffusion couple arrangement to measure tracer diffusion coefficient using Belova et al. approach.

Two cases were considered for the validation of the mathematical formalism to measure tracer diffusion coefficient. First, constant film thickness (i.e., $1 \mu\text{m}$) with varying interdiffusion to tracer diffusion coefficient ratios (i.e., 10, 1, and 0.1). Table 2 reports the parameters used to generate the interdiffusion and spike concentration profiles with constant thin film thickness. Second, varying thin film thickness (i.e., 1, 2, and $3 \mu\text{m}$), with constant interdiffusion to tracer

diffusion coefficient ratio (i.e., 2). Table 3 reports the parameters used to generate the interdiffusion and spike concentration profiles with constant interdiffusion to tracer diffusion ratio. Theoretical interdiffusion concentration profile was obtained using Equation 34 and spike concentration profile was obtained using Equation 35.

Table 2. Parameters used to generate the concentration profiles with constant thin film thickness.

Thin Film thickness (μm)	$\frac{\tilde{D}}{D^*}$	\tilde{D} (m^2/s)	D^* (m^2/s)	t (s)	$\frac{\sqrt{D^*t}}{10^6}$ (μm)
1	10	6×10^{-15}	6×10^{-16}	18000	3.29
	1		6×10^{-15}	3600	4.65
	0.1		6×10^{-14}	900	2.32

Table 3. Parameters used to generate the concentration profiles with constant \tilde{D}/D^* ratio

Thin Film thickness (μm)	$\frac{\tilde{D}}{D^*}$	\tilde{D} (m^2/s)	D^* (m^2/s)	t (s)	$\frac{\sqrt{D^*t}}{10^6}$ (μm)
1	2	6×10^{-15}	3×10^{-15}	7200	4.65
2					
3					

Figure 6 through Figure 8 shows all the concentration profiles modelled using parameters outlined in Table 2. Figure 9 through Figure 11 shows all the concentration profiles modelled using parameters outlined in Table 3. Each figure shows: (a) concentration profile at interdiffusion interface, (b) concentration profile at spike interface, (c) spike profile superimposed over

interdiffusion profile, and (d) Gaussian fitting implemented on difference profile obtained after mathematical subtraction of interdiffusion concentration profile from spike profile.

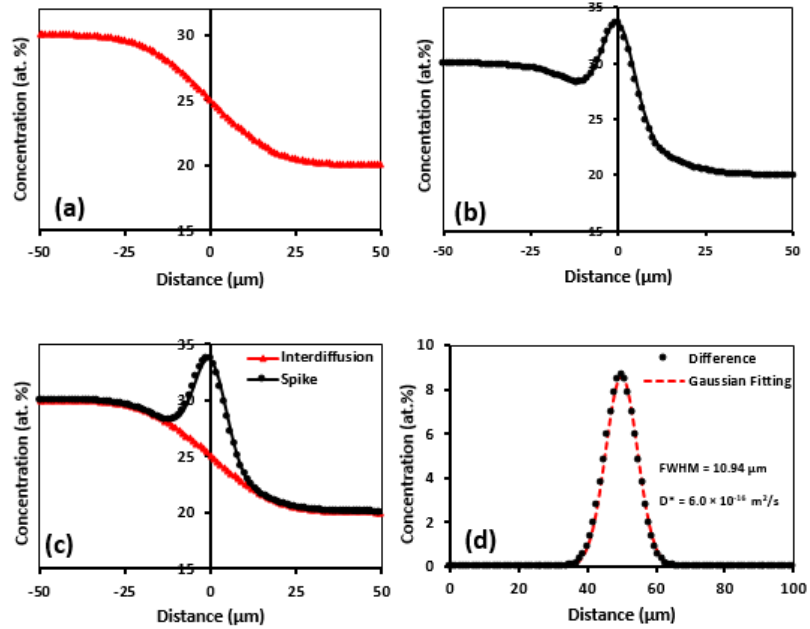


Figure 6. Demonstration of Subtraction method of interdiffusion profile from spike profile when $\tilde{D}/D^*=10$ with $1 \mu\text{m}$ film thickness. Concentration profile at (a) interdiffusion interface, (b) Spike interface. (c) Superimposed Spike profile over interdiffusion profile, and (d) Gaussian fitting implemented on subtracted (difference) profile.

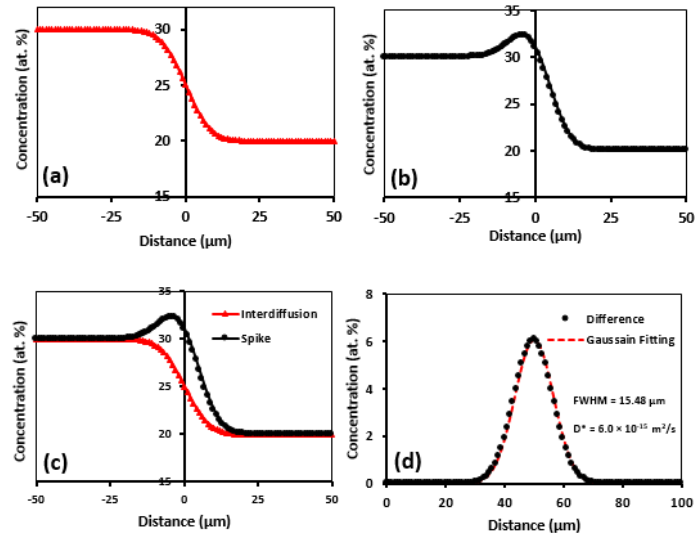


Figure 7. Demonstration of Subtraction method of interdiffusion profile from spike profile when $\tilde{D}/D^*=1$ with $1 \mu\text{m}$ film thickness. Concentration profile at (a) interdiffusion interface, (b) Spike interface. (c) Superimposed Spike profile over interdiffusion profile, and (d) Gaussian fitting implemented on subtracted (difference) profile.

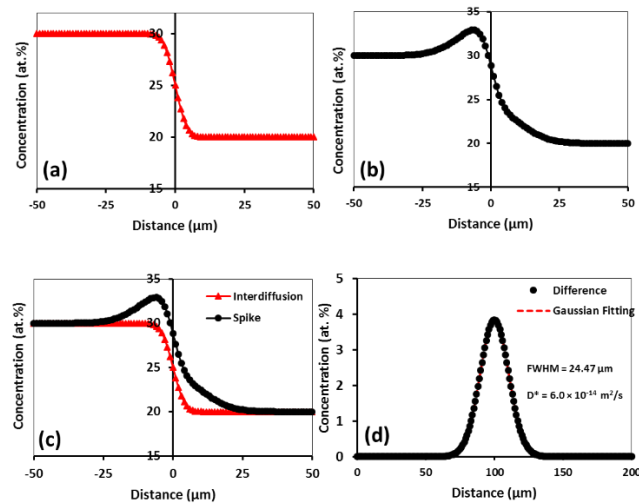


Figure 8. Demonstration of Subtraction method of interdiffusion profile from spike profile when $\tilde{D}/D^*=0.1$ with $1 \mu\text{m}$ film thickness. Concentration profile at (a) interdiffusion interface, (b) Spike interface. (c) Superimposed Spike profile over interdiffusion profile, and (d) Gaussian fitting implemented on subtracted (difference) profile.

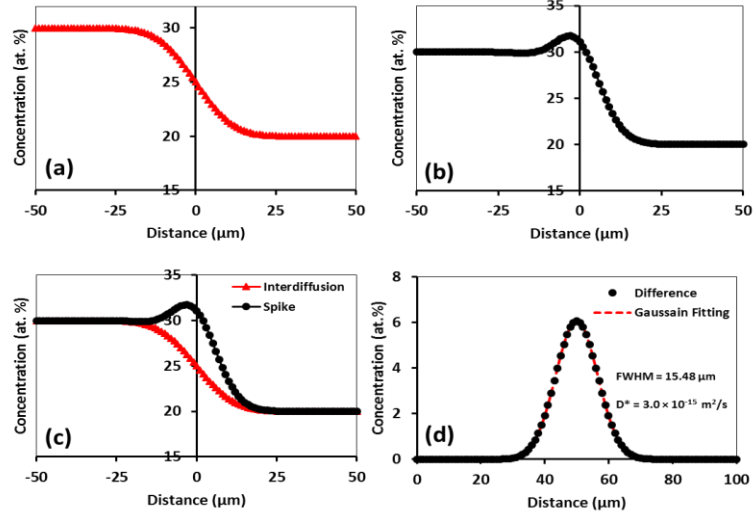


Figure 9. Demonstration of Subtraction method of interdiffusion profile from Spike profile when $\bar{D}/D^*=2$ with 1 μm film thickness. Concentration profile at (a) interdiffusion interface, (b) Spike interface. (c) Superimposed Spike profile over interdiffusion profile, and (d) Gaussian fitting implemented on subtracted (difference) profile.

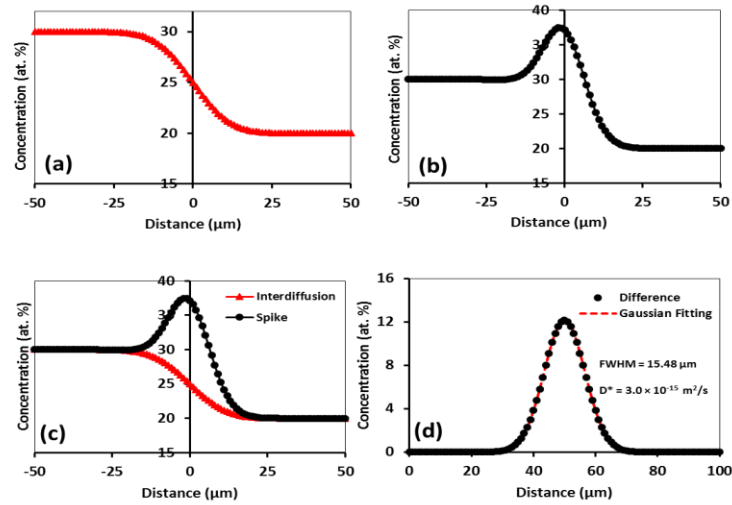


Figure 10. Demonstration of Subtraction method of interdiffusion profile from spike profile when $\bar{D}/D^*=2$ with 2 μm film thickness. Concentration profile at (a) interdiffusion interface, (b) Spike interface. (c) Superimposed Spike profile over interdiffusion profile, and (d) Gaussian fitting implemented on subtracted (difference) profile.

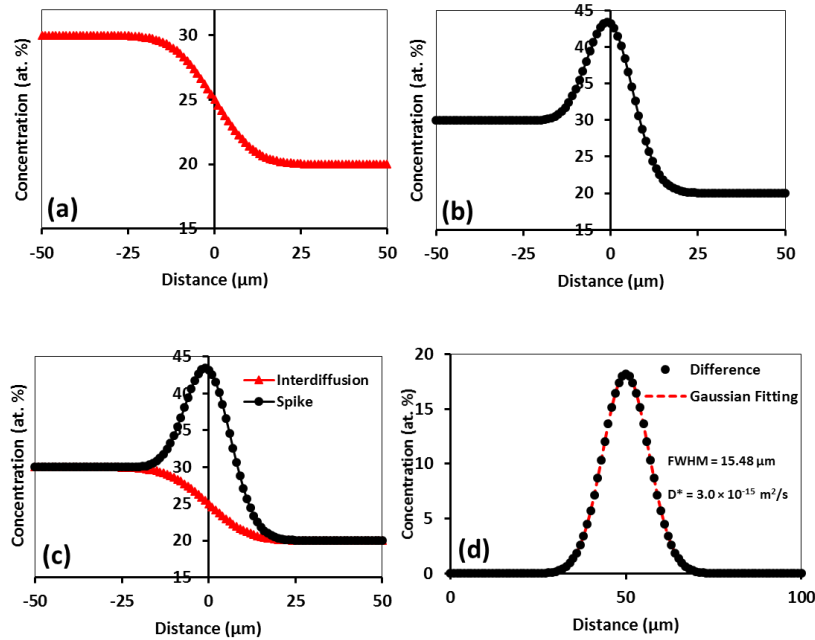


Figure 11. Demonstration of Subtraction method of interdiffusion profile from spike profile when $\bar{D}/D^*=2$ with $3\ \mu\text{m}$ film thickness. Concentration profile at (a) interdiffusion interface, (b) Spike interface. (c) Superimposed Spike profile over interdiffusion profile, and (d) Gaussian fitting implemented on subtracted (difference) profile.

Diffusion zone of the spike concentration profile must be carefully superimposed on the diffusion zone of the interdiffusion profile, such that unaffected terminal ends of both interdiffusion and spike concentration profile in the diffusion couple should exactly lay over one another. Any mismatch in overlaying the spike and interdiffusion profile will underestimate the height and consequently the full width at half maxima position of the difference profile. One of the extreme cases would be when spike profile is superimposed on the unaffected terminal end of the interdiffusion profile, such that the subtraction of interdiffusion profile from spike profile will yield only the “hump” in the spike profile. Hump will significantly underestimate the FWHM and

therefore, calculated tracer diffusion coefficient (D^*) will be lower than actual value. Otherwise, it could be normally misinterpreted that “hump” in the spike profile, represents the movement of tracers.

CHAPTER 4 EXPERIMENTAL METHODS

4.1 Alloy Preparation

Series of binary (FeCr, CoNi, AlNi), quaternary (CoCrFeNi), and quinary (CoCrFeNiMn, AlCoCrFeNi) alloy compositions were prepared with 99.9% pure Co, Cr, Fe, Ni, Mn and Al by arc melting in water cooled Cu crucibles in an Ar atmosphere. Table 4 reports the target composition of the alloys prepared in this study. Casting of the HEAs was performed using Centorr™ Arc melter. Prior to melting, the chamber was flushed with Ar, evacuated to a pressure of 5.0×10^{-5} torr or better, and backfilled with Ar. Alloy ingot was casted and re-melted five times, by flipping the ingot pellet after each melting to promote compositional homogeneity.

Table 4. Target compositions of alloys employed in this study.

Alloys	Al (at.%)	Co (at.%)	Cr (at. %)	Fe (at.%)	Ni (at.%)	Mn (at.%)
Al ₄₈ Ni ₅₂	48	-	-	-	52	-
Fe ₅₀ Cr ₅₀	-	-	50	50	-	-
Co ₅₀ Ni ₅₀	-	50	-	-	50	-
Co ₂₅ Cr ₂₅ Fe ₂₅ Ni ₂₅	-	25	25	25	25	-
Co ₂₀ Cr ₃₀ Fe ₃₀ Ni ₂₀	-	20	30	30	20	-
Co ₃₀ Cr ₂₀ Fe ₂₀ Ni ₃₀	-	30	20	20	30	-
Co ₂₀ Cr ₂₀ Ni ₂₀ Fe ₂₀ Mn ₂₀	-	20	20	20	20	20
Co ₂₅ Cr ₂₅ Fe ₁₅ Ni ₂₅ Mn ₁₀	-	25	25	25	25	10
Co ₁₅ Cr ₁₅ Fe ₂₅ Ni ₁₅ Mn ₃₀	-	15	15	25	15	30
Al ₆ Co ₁₉ Cr ₂₈ Fe ₂₈ Ni ₁₉	6	19	28	28	19	-
Al ₆ Co ₂₈ Cr ₁₉ Fe ₁₉ Ni ₂₈	6	28	19	19	28	-

All alloy ingots listed in Table 4 were further heat treated for homogenization. Each alloy ingot was placed in a quartz tube, flushed with argon and hydrogen several times, and evacuated to a pressure of 8×10^{-6} torr or better. The quartz tube was then backfilled with Ar to a pressure of 165 torr to provide atmospheric condition at elevated temperature and sealed using oxy-

acetylene torch. Homogenization for all alloys was carried out using a CM 1710 furnace at 1100°C for 48 hours. After homogenization, all alloys were water quenched to retain high temperature single phase microstructure. For microstructural examination and compositional measurement, representative sample from the homogenized alloy ingot was sectioned from the middle of the ingot and then metallographically prepared by polishing down to 1 μm surface finish.

4.2 Thin Film Deposition

Electron-beam physical vapor deposition (EB-PVD), with a built-in plasma cleaning capability, was used to deposit Ni thin film on selected HEAs. Figure 12 shows a schematic of the EB-PVD system used in this study. Initially, alloy disks, approximately 10 mm in diameter and 3 mm in height, were mounted on the substrate holder and loaded in the PVD chamber. EB-PVD deposition chamber was evacuated to a pressure of approximately 1.2×10^{-7} torr, and sample surfaces were plasma cleaned using Ar plasma. Electron beam was generated by passing a current (~80 mA) through tungsten filament (electron source). Then, electron beam was accelerated by applying an acceleration voltage (-10 kV). With an application of magnetic field, path of the electron beam was deflected towards the target. On impact, highly energetic electron loses its kinetic energy, and vaporize the target material. Due to the large mean free path under vacuum, vaporized metal travel towards substrate in the shortest distance.

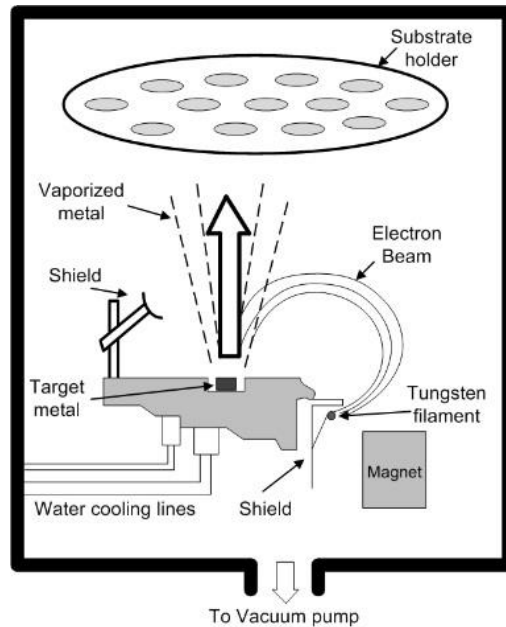


Figure 12. A schematic of electron beam physical vapor deposition system.

During deposition process, substrate holder was allowed to rotate to achieve uniform thickness of films. Deposition rate was maintained at approximately $0.7 \text{ \AA}/\text{sec}$, which was monitored using the resonant frequency of the oscillating quartz crystal. Thickness of the film deposited on alloys is proportional to the change in resonant frequency of the quartz crystal (i.e., shift in frequency). Time of deposition was adjusted to achieve a film thickness of approximately 900 nm. To verify the film thickness, Focused Ion beam (FEI™ TEM 200-FIB) was used to cut the thin slice of cross section, which allowed the direct measurement of film thickness.

4.3 Diffusion Couples

The surface of each alloy was metallographically polished down to $1 \text{ }\mu\text{m}$ finish. Diffusion couples were fabricated by placing the surfaces of two selected alloys in contact. In tracer diffusion

couples, one of the terminal alloy has a pre-deposited metal thin film (i.e., Ni tracer). The alloys in diffusion couple were held tightly by two stainless steel jigs and clamped together with screws, tightened with an applied torque of approximately 2.5 N-m. Thin alumina spacers were placed between alloys and stainless steel jigs to avoid any high temperature diffusional interaction between alloys and jigs. The assembled diffusion couple along with a tantalum foil (i.e., oxygen getter) was placed in a quartz tube, evacuated to a pressure of 8.0×10^{-6} torr or better, and flushed with high purity Ar and H₂ gas. Evacuation and flushing was repeated three times, and the quartz tube was finally backfilled with high purity Ar before sealing. Details of diffusion couple assembly can be found elsewhere [47, 59-62].

Each diffusion couple was isothermally annealed using a Lindberg Blue™ three-zone tube furnace operating at 900°C, 950°, and 1000°C, and CM 1710 furnace operating at 1100°C and 1200°C. After annealing, all diffusion couples were water quenched to preserve the high temperature microstructure. For interdiffusion study, six sets of diffusion couples, were annealed at 900°C, 1000°C, 1100°C, and 1200°C. All diffusion couples for interdiffusion study are listed in Table 5. Al₄₈Ni₅₂ vs. Co₂₅Cr₂₅Fe₂₅Ni₂₅ and Al₄₈Ni₅₂ vs. Co₂₀Cr₂₀Fe₂₀Ni₂₀Mn₂₀ diffusion couples were designed in such a way that the solubility limit of Al were directly determined in off-equiatom FCC Al-Co-Cr-Fe-Ni and Al-Co-Cr-Fe-Ni-Mn alloys to investigate the high entropy effect.

Table 5. Diffusion couples employed for interdiffusion study.

System	Alloy 1 Terminal Composition	Alloy 2 Terminal Composition	Temperature (°C)	Time (h)	
Quaternary	Fe ₅₀ Cr ₅₀	Co ₅₀ Ni ₅₀	900	120	
			1000	120	
			1100	48	
			1200	48	
	Co ₂₀ Cr ₃₀ Fe ₃₀ Ni ₂₀	Co ₃₀ Cr ₂₀ Fe ₂₀ Ni ₃₀	900	240	
			1000	240	
			1100	240	
			1200	48	
Quinary	Co ₂₅ Cr ₂₅ Ni ₂₅ Fe ₁₅ Mn ₁₀	Co ₁₅ Cr ₁₅ Ni ₁₅ Fe ₂₅ Mn ₃₀	900	120	
			1000	120	
			1100	48	
			1200	48	
	Al ₆ Co ₁₉ Cr ₂₈ Fe ₂₈ Ni ₁₉	Al ₆ Co ₂₈ Cr ₁₉ Fe ₁₉ Ni ₂₈	900	120	
			1000	120	
			1100	48	
			1200	24	
	Al ₄₈ Ni ₅₂	Co ₂₅ Cr ₂₅ Fe ₂₅ Ni ₂₅	900	240	
			1000	120	
			1100	48	
			1200	24	
	Senary	Al ₄₈ Ni ₅₂	Co ₂₀ Cr ₂₀ Fe ₂₀ Ni ₂₀ Mn ₂₀	900	240
				1000	120
				1100	48
				1200	24

For tracer diffusion study, three sets of diffusion couples, namely Co₂₀Cr₃₀Fe₃₀Ni₂₀ vs. Co₃₀Cr₂₀Fe₂₀Ni₃₀, Co₂₅Cr₂₅Ni₂₅Fe₁₅Mn₁₀ vs. Co₁₅Cr₁₅Ni₁₅Fe₂₅Mn₃₀ and Co₂₀Cr₂₅Ni₂₅Fe₁₅Cu₁₀ vs. Co₂₀Cr₁₅Ni₁₅Fe₂₅Cu₃₀, with the Ni thin film sandwiched between the two terminal alloys, were

annealed at 900°C, 950°C, and 1000°C. Table 6 reports the “sandwich” thin film diffusion couples and annealing temperature.

Table 6. “Sandwich” thin film diffusion couples employed for tracer diffusion study.

System	Alloy 1 Terminal Composition	Thin Film	Alloy 2 Terminal Composition	Temperature (°C)	Time (h)
Quaternary	Co ₂₀ Cr ₃₀ Fe ₃₀ Ni ₂₀	Ni	Co ₃₀ Cr ₂₀ Fe ₂₀ Ni ₃₀	900	24
				950	12
				1000	8
Quinary	Co ₂₅ Cr ₂₅ Ni ₂₅ Fe ₁₅ Mn ₁₀	Ni	Co ₁₅ Cr ₁₅ Ni ₁₅ Fe ₂₅ Mn ₃₀	900	12
				950	6
				1000	2
	Al ₆ Co ₁₉ Cr ₂₈ Fe ₂₈ Ni ₁₉	Ni	Al ₆ Co ₂₈ Cr ₁₉ Fe ₁₉ Ni ₂₈	900	12
				950	6
				1000	2

Annealing time of tracer diffusion couples were estimated such that a “spike” in concentration profile after isothermal annealing would not disappear. Estimated interdiffusion coefficient and thin film thickness were used to theoretically estimate the tracer concentration profile (e.g., spike) as a sum of standard interdiffusion solution (i.e., error function) and thin film solution (i.e., Gaussian function) given by Equation 35. Finally, diffusion couples are cross-sectioned using a low speed diamond saw and mounted in cold resin epoxy. Cross sectioned surfaces are metallographically polished down to 1 μm finish for characterization.

4.4 Characterization

Single phase formation and homogeneity in microstructure in homogenized alloys was examined by PANalytical Empyrean™ Basic X-ray diffraction system and Zeiss™ Ultra-55 field

emission scanning electron microscope (FE-SEM) equipped with energy dispersive X-ray spectroscopy (XEDS). The microstructure of each diffusion couple was also examined by FE-SEM. Concentration profiles across the interdiffusion zone were obtained using XEDS. Multiple interdiffusion line scans were collected and analyzed for each diffusion couple to ensure statistical confidence. Concentration profiles measured from XEDS were curve fitted using OriginPro 8.5 software, with non-linear curve fitting function given by Equation 36.

CHAPTER 5 HIGH ENTROPY EFFECT

Mechanism of stabilization of single phase, i.e. high entropy effect, in HEAs may be debatable. It was initially hypothesized that a large number of constituent elements in equal amount would increase the entropy of mixing, which would lower the overall Gibbs free energy of mixing, particularly at high temperature. Therefore, high entropy phases, e.g. random/disordered solid solution phases, tend to stabilize in comparison to low entropy phases, e.g. intermetallic phases. Theory of entropic stabilization of phases due to high configurational entropy, however, falls short to explain the multiple phases observed in various experimental, near-equiatomic alloys, e.g., AlCoCrFeNi [12], AlCoCrFeNiMn [13], CoCrFeNiMo [14]. Intuitively a simple replacement of an element in HEA by another element would not ensure the formation of single phase solid solution, e.g. replacing Mn with either Al or Mo in single phase, equiatomic CoCrFeNiMn alloy. Therefore, entropy of mixing alone may not always result in lowering of the Gibbs free energy [15]. Otto *et al.* [16] also suggested that an increase in configurational entropy may not stabilize the single phase in all alloys, since this effect may not be sufficient enough to overcome the driving forces that favor the formation of secondary phases.

In this chapter, high entropy effect was examined in Al-Co-Cr-Fe-Ni and Al-Co-Cr-Fe-Ni-Mn alloys using solid-to-solid diffusion couple investigation. The β -Al₄₈Ni₅₂ vs. Co₂₅Cr₂₅Fe₂₅Ni₂₅ and β -Al₄₈Ni₅₂ vs. Co₂₀Cr₂₀Fe₂₀Ni₂₀Mn₂₀ diffusion couple was annealed at high temperature (900 - 1200°C). The couples generated continuous compositions of off-equiatomic Al_pCo_qCr_rFe_sNi_t and Al_pCo_qCr_rFe_sNi_tMn_u alloys, respectively. Solubility limit of Al in Al_pCo_qCr_rFe_sNi_t and Al_pCo_qCr_rFe_sNi_tMn_u alloys were determined as a function of temperature and compared with the

solubility limit of Al in equiatomic $\text{Al}_x\text{CoCrFeNi}$ and $\text{Al}_x\text{CoCrFeNiMn}$ alloys, respectively. Results were analyzed with regards to the contributions of enthalpy (ΔH) and entropy ($-T\Delta S$) to the thermodynamic stability (ΔG) of equiatomic and off-equiatomic Al-Co-Cr-Fe-Ni and Al-Co-Cr-Fe-Ni-Mn alloys.

5.1 Solubility limit of Al in Al-Co-Cr-Fe-Ni alloy

Microstructure of Al-Co-Cr-Fe-Ni alloy depends on the amount of Al. For instance, in as-cast $\text{Al}_x\text{CoCrFeNi}$ alloy, FCC phase is stable for $x < 0.45$ (~ 10.1 at. % Al), BCC phase is stable for $x > 0.88$ (~ 18.0 at. % Al), and duplex (i.e. FCC + BCC) phases are stable for $0.45 \leq x \leq 0.88$ [12, 63]. Therefore, solubility limit of Al in off-equiatomic $\text{Al}_p\text{Co}_q\text{Cr}_r\text{Fe}_s\text{Ni}_t$ alloy was also determined, using diffusion couple experiments. Figure 13 presents the concentration profiles superimposed on backscatter electron micrographs from the $\text{Al}_{48}\text{Ni}_{52}$ vs. $\text{Co}_{25}\text{Cr}_{25}\text{Fe}_{25}\text{Ni}_{25}$ diffusion couples isothermally annealed at (a) 900°C for 240 hours, (b) 1000°C for 120 hours, (c) 1100°C for 48 hours, and (d) 1200°C for 24 hours. During interdiffusion of Al and Ni in $\text{Co}_{25}\text{Cr}_{25}\text{Fe}_{25}\text{Ni}_{25}$ (FCC) alloy, continuous off-equiatomic compositions of FCC $\text{Al}_p\text{Co}_q\text{Cr}_r\text{Fe}_s\text{Ni}_t$ evolved, however, BCC or duplex phases were not observed in the starting microstructure of $\text{Co}_{25}\text{Cr}_{25}\text{Fe}_{25}\text{Ni}_{25}$ alloy. This observation suggests that the diffusion was significantly faster in FCC phase than BCC phase.

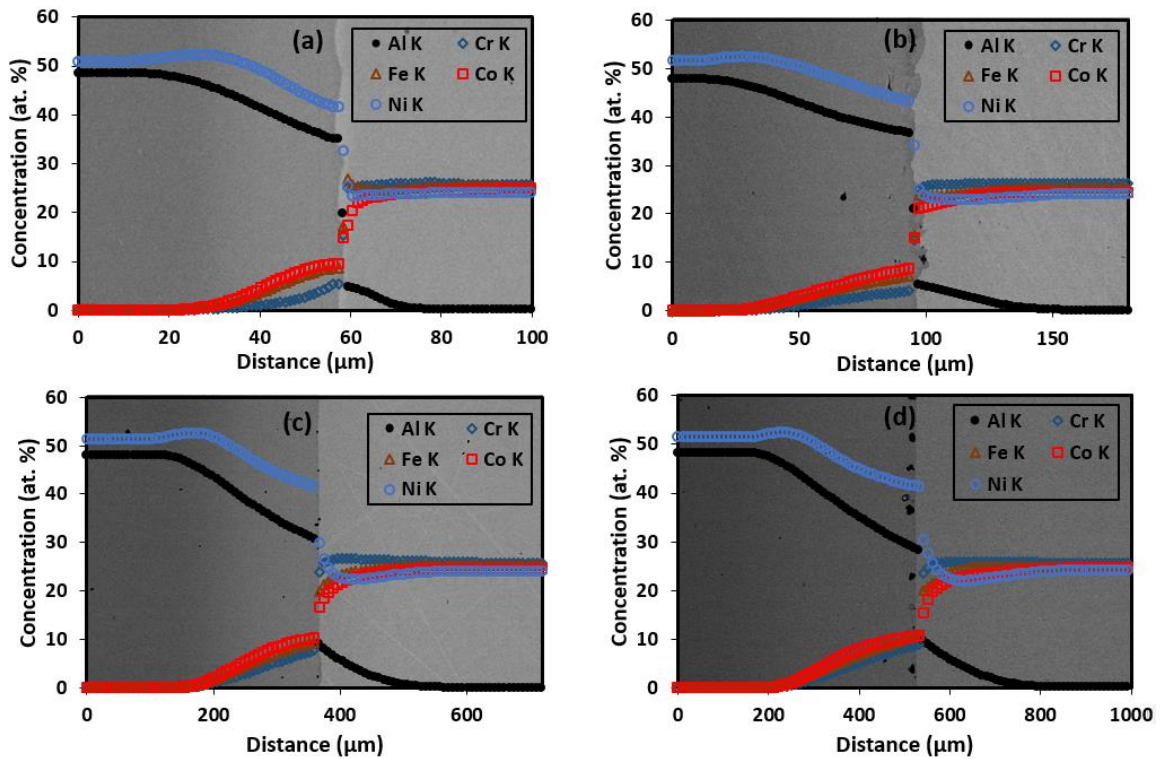


Figure 13. Concentration profiles superimposed on BSE micrographs of $\text{Al}_{48}\text{Ni}_{52}$ vs. $\text{Co}_{25}\text{Cr}_{25}\text{Fe}_{25}\text{Ni}_{25}$ diffusion couples isothermally annealed at (a) 900°C for 240 hours, (b) 1000°C for 120 hours, (c) 1100°C for 48 hours, and (d) 1200°C for 24 hours.

Temperature dependent solubility limit of Al in $\text{Al}_x\text{CoCrFeNi}$ alloy was determined using the pseudo-binary phase diagram between Al and equiatomic CoCrFeNi alloy, as shown in Figure 14 [64]. Figure 15 compares the experimentally determined solubility limit of Al in off-equiatomic FCC $\text{Al}_p\text{Co}_q\text{Cr}_r\text{Fe}_s\text{Ni}_t$ alloy, via diffusion couples, with the solubility limit of Al in equiatomic FCC $\text{Al}_x\text{CoCrFeNi}$ alloy, via phase diagram, and maximum solubility of Al in as-cast $\text{Al}_x\text{CoCrFeNi}$ (i.e. $x = 0.45$) alloy. Figure 15 depicts that the solubility limit of Al determined via

diffusion couples in $\text{Al}_p\text{Co}_q\text{Cr}_r\text{Fe}_s\text{Ni}_t$ at 1100° and 1200°C is higher than solubility limit of Al in $\text{Al}_x\text{CoCrFeNi}$ alloy determined using phase diagram.

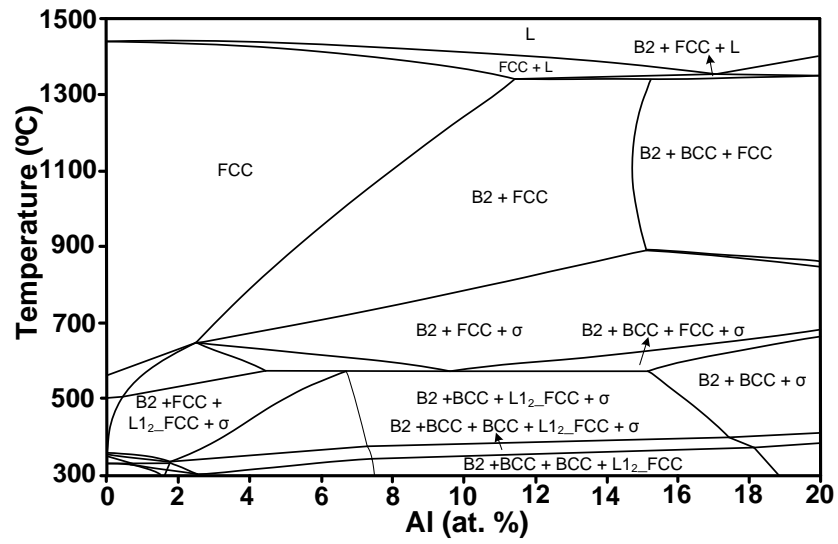


Figure 14. Pseudo-binary phase diagram between Al and equiatomic CoCrFeNi

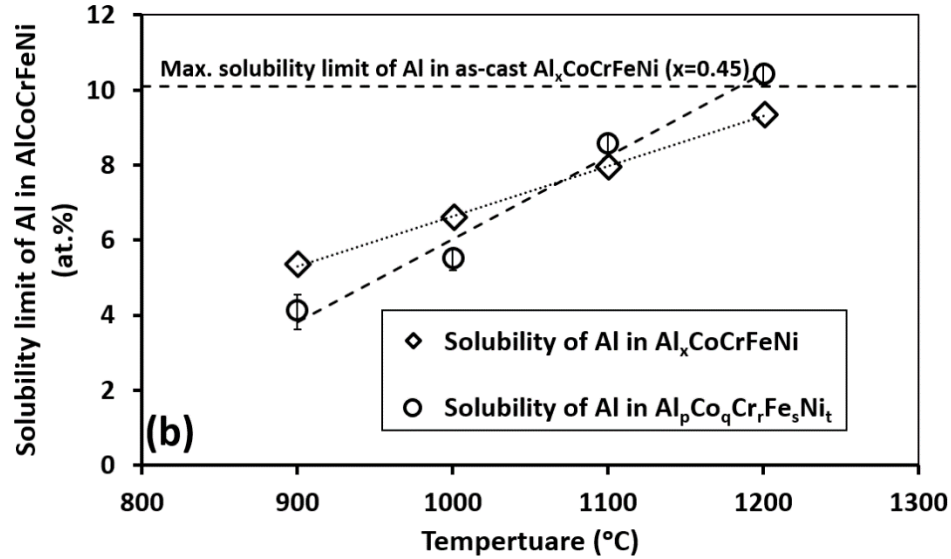


Figure 15. Comparison of maximum solubility limit of Al as a function of temperature in $Al_pCo_qCr_rFe_sNi_t$ (via diffusion couple) and $Al_xCoCrFeNi$ (via. phase diagram) HEAs.

Figure 16 (a) compares the configurational entropy of composition corresponding to the maximum solubility limit of Al in $Al_pCo_qCr_rFe_sNi_t$ alloy with the maximum solubility limit of Al in $Al_xCoCrFeNi$ alloy. Experimentally determined configurational entropy of $Al_pCo_qCr_rFe_sNi_t$ compositions between 900° and 1200°C has been extrapolated to temperature (~ 1340.9°C) corresponding to the maximum solubility limit of Al in $Al_xCoCrFeNi$, as per phase diagram. For all temperatures, configurational entropy of off-equiatomic $Al_pCo_qCr_rFe_sNi_t$ alloy is lower than the configurational entropy of equiatomic $Al_xCoCrFeNi$ alloy. This suggests that the entropy contribution ($-T\Delta S_{mix}$) in minimizing the overall free energy for stabilizing of the single phase in off-equiatomic $Al_pCo_qCr_rFe_sNi_t$ alloy is higher than the entropy contribution in equiatomic $Al_xCoCrFeNi$ alloy, i.e. $-T\Delta S_{mix}|^{equiatomic\ alloy} < -T\Delta S_{mix}|^{off-equiatomic\ alloy}$. Figure 16 (b) present the

thermodynamic stability parameters, i.e. ΔH_{mix} , $-T\Delta S_{\text{mix}}$, and ΔG_{mix} , as a function of temperature for equiatomic $\text{Al}_x\text{CoCrFeNi}$ and off-equiatomic $\text{Al}_p\text{Co}_q\text{Cr}_r\text{Fe}_s\text{Ni}_t$ alloys, corresponding to the maximum solubility limit of Al. It can be observed that the free energy of mixing (ΔG_{mix}) of $\text{Al}_p\text{Co}_q\text{Cr}_r\text{Fe}_s\text{Ni}_t$ alloy is lower than the free energy of mixing of $\text{Al}_x\text{CoCrFeNi}$ at 1100°C and above temperatures. Higher thermodynamic stability of $\text{Al}_p\text{Co}_q\text{Cr}_r\text{Fe}_s\text{Ni}_t$ alloy at 1100°C and above temperatures may be the possible reason for higher solubility of Al in off-equiatomic $\text{Al}_p\text{Co}_q\text{Cr}_r\text{Fe}_s\text{Ni}_t$ alloy than in equiatomic $\text{Al}_x\text{CoCrFeNi}$ alloy. Enthalpy of mixing (ΔH_{mix}) plays a significant role in minimizing the overall free energy of off-equiatomic $\text{Al}_p\text{Co}_q\text{Cr}_r\text{Fe}_s\text{Ni}_t$, in comparison to equiatomic $\text{Al}_x\text{CoCrFeNi}$ at 1100°C and above temperatures. This estimate can be drawn since entropy contribution ($-T\Delta S_{\text{mix}}$) is always lower in off-equiatomic $\text{Al}_p\text{Co}_q\text{Cr}_r\text{Fe}_s\text{Ni}_t$ than in equiatomic $\text{Al}_x\text{CoCrFeNi}$. It can also be noticed from Figure 16 (b) that ΔH_{mix} is lower for $\text{Al}_p\text{Co}_q\text{Cr}_r\text{Fe}_s\text{Ni}_t$ at 1100°C and above temperatures i.e. $\Delta H_{\text{mix}}^{\text{equiatomic alloy}} > \Delta H_{\text{mix}}^{\text{off-equiatomic alloy}}$. It also demonstrates that off-equiatomic (i.e. lower ΔS_{mix}) compositions may also exhibit the similar/higher stability than their possible equiatomic (i.e. highest ΔS_{mix}) counterparts at high temperature.

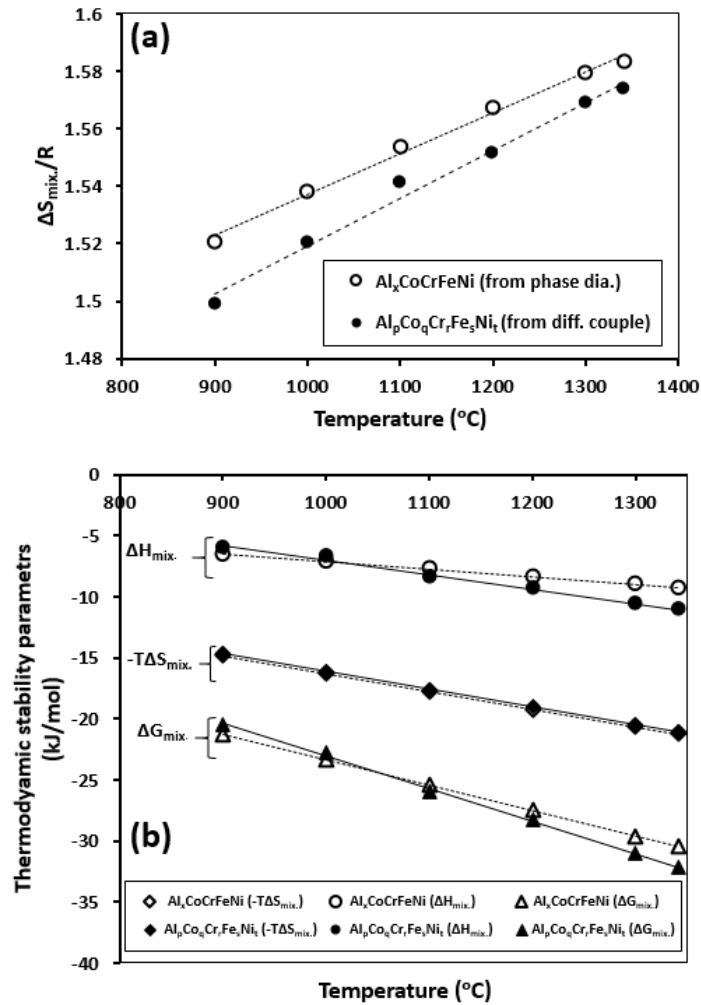


Figure 16. (a) Comparison of Entropy of mixing ($\Delta S_{mix}/R$) in $Al_pCo_qCr_rFe_sNi_t$ (using diffusion couple), and $Al_xCoCrFeNi$ (using phase diagram) for the compositions corresponding to the maximum solubility limit of Al. (b) Comparison of thermodynamic parameters measured in the $Al_pCo_qCr_rFe_sNi_t$, and $Al_xCoCrFeNi$ alloys.

It has been argued that configurational entropy of mixing does not remain constant for a given composition as a function of temperature, due to excess entropy term arises from the correlation effects between constituents elements [10], which is also described in section 3.2.

Figure 17 (a) compares the correlated configurational entropy as a function of temperature for the compositions corresponding to the maximum solubility limit of Al in $\text{Al}_p\text{Co}_q\text{Cr}_r\text{Fe}_s\text{Ni}_t$ with the maximum solubility limit of Al in $\text{Al}_x\text{CoCrFeNi}$. At 1100°C and above temperatures, correlated configurational entropy of $\text{Al}_p\text{Co}_q\text{Cr}_r\text{Fe}_s\text{Ni}_t$ is always lower than that of $\text{Al}_x\text{CoCrFeNi}$. Corresponding correlated free energy of mixing is also lower for $\text{Al}_p\text{Co}_q\text{Cr}_r\text{Fe}_s\text{Ni}_t$ than the $\text{Al}_x\text{CoCrFeNi}$ at 1100°C and above temperatures, as shown in Figure 17 (b). Therefore, enthalpy of mixing (ΔH_{mix}) plays a significant role in minimizing the overall correlated free energy of off-equiatomic $\text{Al}_p\text{Co}_q\text{Cr}_r\text{Fe}_s\text{Ni}_t$ alloy, in comparison to equiatomic $\text{Al}_x\text{CoCrFeNi}$ alloy.

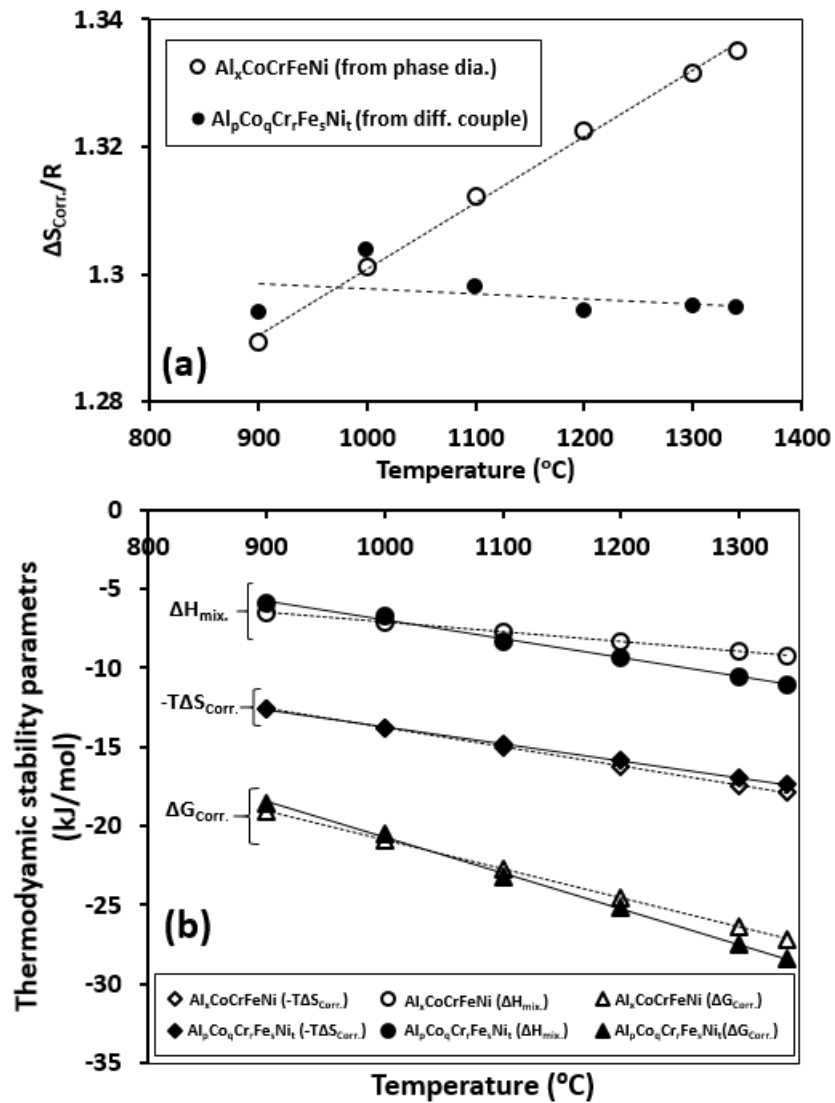


Figure 17. (a) Comparison of correlated entropy of mixing ($\Delta S_{\text{corr.}}/R$) in Al_pCo_qCr_rFe_sNi_t (using diffusion couple), Al_xCoCrFeNi (using phase diagram) for the compositions corresponding to the maximum solubility limit of Al. (b) Comparison of correlated thermodynamic parameters measured in the Al_pCo_qCr_rFe_sNi_t and Al_xCoCrFeNi alloys.

5.2 Solubility limit of Al in Al-Co-Cr-Fe-Ni-Mn alloy

Similar to Al-Co-Cr-Fe-Ni alloy, microstructure of Al-Co-Cr-Fe-Ni-Mn alloy also depends on the amount of Al. For instance, in as-cast $Al_xCoCrFeNiMn$ alloy, FCC phase is stable for $x < 0.435$ (~ 8 at. % Al), BCC phase is stable for $x > 1.25$ (~ 20 at. % Al), and duplex (i.e. FCC + BCC) phases are stable for $0.435 \leq x \leq 0.87$ [13]. Therefore, solubility limit of Al in off-equiatomic $Al_pCo_qCr_rFe_sNi_tMn_u$ alloys was also determined, using diffusion couple experiments. Figure 18 presents the concentration profiles superimposed on backscatter electron micrographs from the $Al_{48}Ni_{52}$ vs. $Co_{20}Cr_{20}Fe_{20}Ni_{20}Mn_{20}$ diffusion couples isothermally annealed at (a) 900°C for 240 hours, (b) 1000°C for 120 hours, (c) 1100°C for 48 hours, and (d) 1200°C for 24 hours. During interdiffusion of Al and Ni in $Co_{20}Cr_{20}Fe_{20}Ni_{20}Mn_{20}$ (FCC) alloy, continuous off-equiatomic compositions of FCC $Al_pCo_qCr_rFe_sNi_tMn_u$ evolved, however, BCC or duplex phases were not observed in the starting microstructure of $Co_{20}Cr_{20}Fe_{20}Ni_{20}Mn_{20}$ alloy, similar to $Al_{48}Ni_{52}$ vs. $Co_{25}Cr_{25}Fe_{25}Ni_{25}$ diffusion couples. This observation suggests that the diffusion was significantly faster in FCC phase than BCC phase.

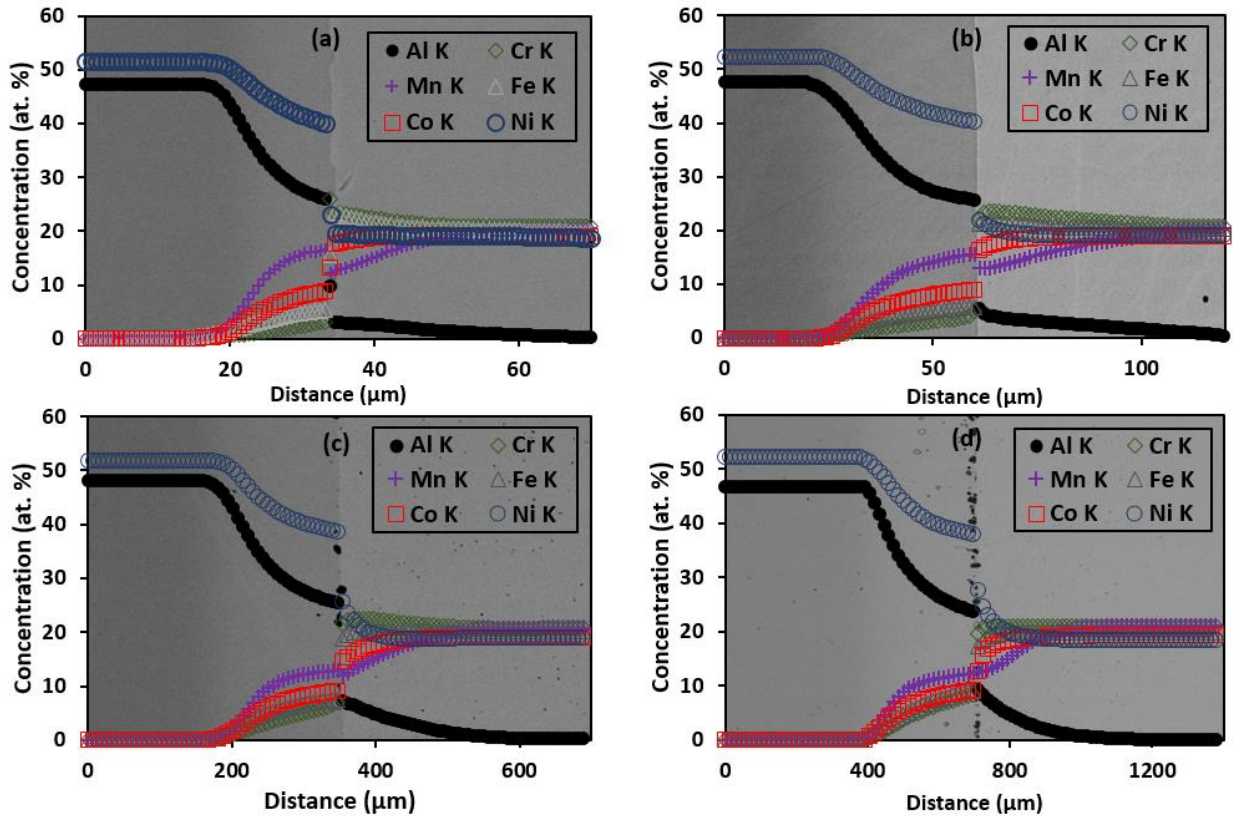


Figure 18. Concentration profiles superimposed on BSE micrographs of $\text{Al}_{48}\text{Ni}_{52}$ vs. $\text{Co}_{20}\text{Cr}_{20}\text{Ni}_{20}\text{Fe}_{20}\text{Mn}_{20}$ diffusion couples isothermally annealed at (a) 900°C for 240 hours, (b) 1000°C for 120 hours, (c) 1100°C for 48 hours, and (d) 1200°C for 24 hours.

Temperature dependent solubility limit of Al in $\text{Al}_x\text{CoCrFeNiMn}$ alloy was determined using the pseudo-binary phase diagram between Al and equiatomic CoCrFeNiMn alloy, as shown in Figure 19. Figure 20 compares the experimentally determined solubility limit of Al in off-equiatomic FCC $\text{Al}_p\text{Co}_q\text{Cr}_r\text{Fe}_s\text{Ni}_t\text{Mn}_u$ alloy, via diffusion couples, with the solubility limit of Al in equiatomic FCC $\text{Al}_x\text{CoCrFeNiMn}$ alloy, via phase diagram, and maximum solubility of Al in as-cast $\text{Al}_x\text{CoCrFeNiMn}$ (i.e. $x = 0.435$) alloy. Figure 20 depicts that the solubility limit of Al

determined via diffusion couples in $\text{Al}_p\text{Co}_q\text{Cr}_r\text{Fe}_s\text{Ni}_t\text{Mn}_u$ at 1100° and 1200°C is higher than solubility limit of Al in $\text{Al}_x\text{CoCrFeNiMn}$ alloy determined using phase diagram.

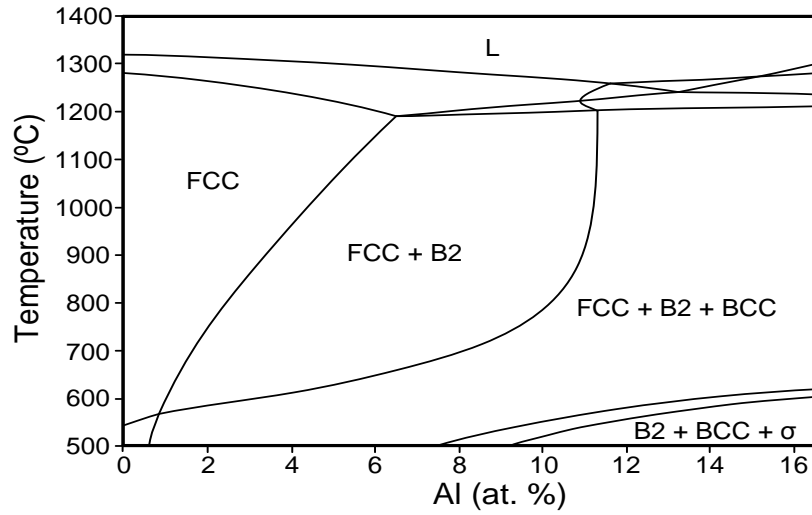


Figure 19. Pseudo-binary phase diagram between Al and equiatomic CoCrFeNiMn.

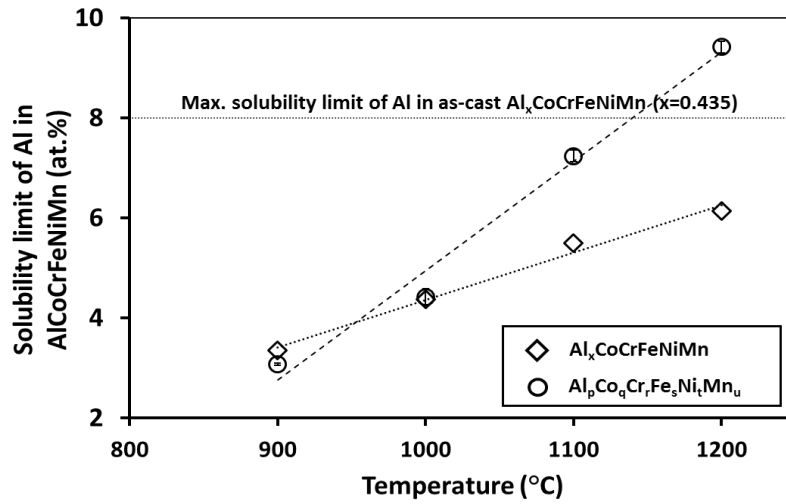


Figure 20. Comparison of maximum solubility limit of Al as a function of temperature in $\text{Al}_p\text{Co}_q\text{Cr}_r\text{Fe}_s\text{Ni}_t\text{Mn}_u$ (via. diffusion couple) and $\text{Al}_x\text{CoCrFeNiMn}$ (via. phase diagram) HEAs.

Figure 21 (a) compares the configurational entropy of composition corresponding to the maximum solubility limit of Al in $\text{Al}_p\text{Co}_q\text{Cr}_r\text{Fe}_s\text{Ni}_t\text{Mn}_u$ alloy and maximum solubility limit of Al in $\text{Al}_x\text{CoCrFeNiMn}$ alloy. For all temperatures, configurational entropy of off-equiatomic $\text{Al}_p\text{Co}_q\text{Cr}_r\text{Fe}_s\text{Ni}_t\text{Mn}_u$ alloy is lower than the configurational entropy of equiatomic $\text{Al}_x\text{CoCrFeNiMn}$ alloy. This suggests that the entropy contribution ($-T\Delta S_{\text{mix}}$) in minimizing the overall free energy for stabilizing of the FCC single phase in off-equiatomic $\text{Al}_p\text{Co}_q\text{Cr}_r\text{Fe}_s\text{Ni}_t\text{Mn}_u$ alloy is higher than the entropy contribution in equiatomic $\text{Al}_x\text{CoCrFeNiMn}$ alloy, i.e. $-T\Delta S_{\text{mix}}|_{\text{equiatomic alloy}} < -T\Delta S_{\text{mix}}|_{\text{off-equiatomic alloy}}$. Figure 21 (b) present the thermodynamic stability parameters, i.e. ΔH_{mix} , $-T\Delta S_{\text{mix}}$, and ΔG_{mix} , as a function of temperature for equiatomic $\text{Al}_x\text{CoCrFeNiMn}$ and off-equiatomic $\text{Al}_p\text{Co}_q\text{Cr}_r\text{Fe}_s\text{Ni}_t\text{Mn}_u$. The free energy of mixing (ΔG_{mix}) of $\text{Al}_p\text{Co}_q\text{Cr}_r\text{Fe}_s\text{Ni}_t\text{Mn}_u$ alloy is lower than the free energy of mixing of $\text{Al}_x\text{CoCrFeNiMn}$ at 1100°C and above temperatures. Higher thermodynamic stability of $\text{Al}_p\text{Co}_q\text{Cr}_r\text{Fe}_s\text{Ni}_t\text{Mn}_u$ alloy at 1100°C and above temperatures may be the possible reason for higher solubility of Al in off-equiatomic $\text{Al}_p\text{Co}_q\text{Cr}_r\text{Fe}_s\text{Ni}_t\text{Mn}_u$ alloy than in equiatomic $\text{Al}_x\text{CoCrFeNiMn}$ alloy. Enthalpy of mixing (ΔH_{mix}) plays a significant role in minimizing the overall free energy of off-equiatomic $\text{Al}_p\text{Co}_q\text{Cr}_r\text{Fe}_s\text{Ni}_t\text{Mn}_u$, in comparison to equiatomic $\text{Al}_x\text{CoCrFeNiMn}$, i.e. $\Delta H_{\text{mix}}|_{\text{equiatomic alloy}} > \Delta H_{\text{mix}}|_{\text{off-equiatomic alloy}}$ at 1100°C and above temperatures. This estimate can be drawn since entropy contribution ($-T\Delta S_{\text{mix}}$) is always lower in off-equiatomic $\text{Al}_p\text{Co}_q\text{Cr}_r\text{Fe}_s\text{Ni}_t\text{Mn}_u$ than in equiatomic $\text{Al}_x\text{CoCrFeNiMn}$. Aforementioned that off- equiatomic (i.e. lower ΔS_{mix}) compositions may also

exhibit the similar/higher stability than their possible equiatomic (i.e. highest $\Delta S_{\text{mix.}}$) counterparts at high temperature.

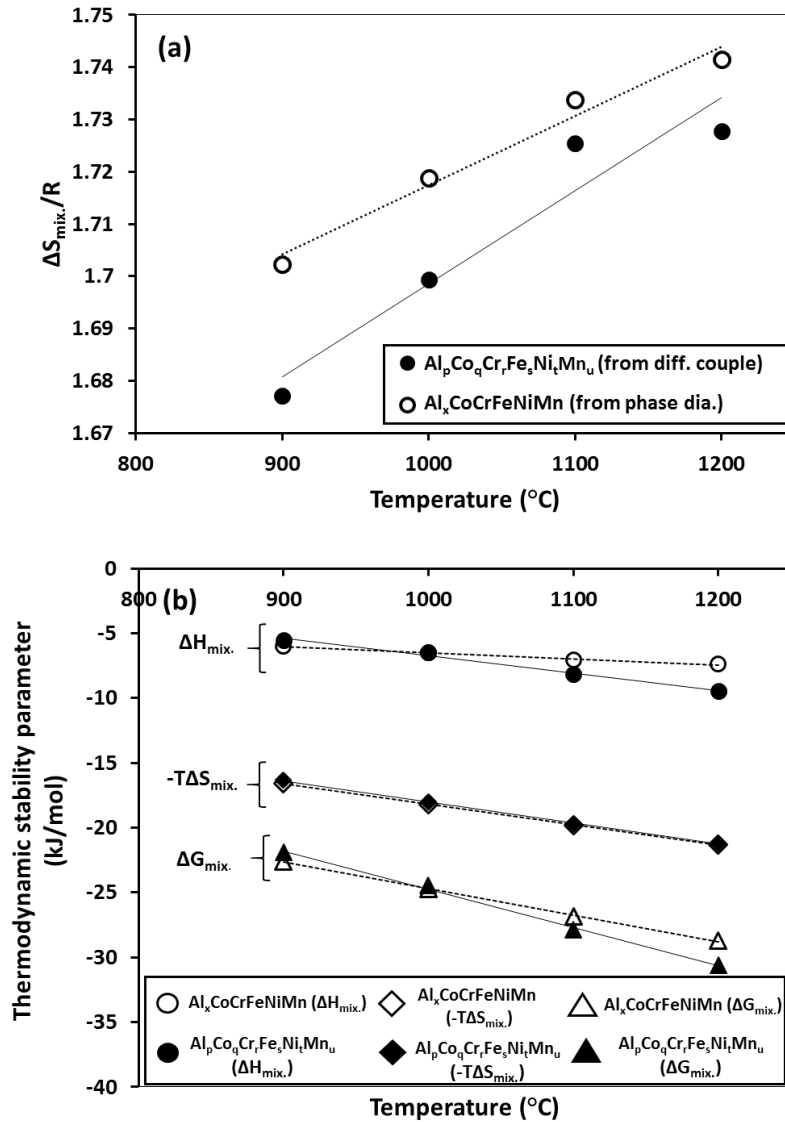


Figure 21. (a) Comparison of Entropy of mixing ($\Delta S_{\text{mix.}}/R$) in Al_pCo_qCr_rFe_sNi_t (using diffusion couple), and Al_xCoCrFeNi (using phase diagram) for the compositions corresponding to the maximum solubility limit of Al. (b) Comparison of thermodynamic parameters measured in the Al_pCo_qCr_rFe_sNi_t, and Al_xCoCrFeNi.

Figure 22 (a) compares the correlated configurational entropy as a function of temperature for the compositions corresponding to the maximum solubility limit of Al in $\text{Al}_p\text{Co}_q\text{Cr}_r\text{Fe}_s\text{Ni}_t\text{Mn}_u$ and the maximum solubility limit of Al in $\text{Al}_x\text{CoCrFeNiMn}$. At 1100°C and above temperatures, correlated configurational entropy of $\text{Al}_p\text{Co}_q\text{Cr}_r\text{Fe}_s\text{Ni}_t\text{Mn}_u$ is always lower than that of $\text{Al}_x\text{CoCrFeNiMn}$. Corresponding correlated free energy of mixing is also lower for $\text{Al}_p\text{Co}_q\text{Cr}_r\text{Fe}_s\text{Ni}_t\text{Mn}_u$ than the $\text{Al}_x\text{CoCrFeNiMn}$ at 1100°C and above temperatures, as shown in Figure 22 (b). Therefore, enthalpy of mixing (ΔH_{mix}) plays a significant role in minimizing the overall correlated free energy of off-equiatomic $\text{Al}_p\text{Co}_q\text{Cr}_r\text{Fe}_s\text{Ni}_t\text{Mn}_u$ alloy, in comparison to equiatomic $\text{Al}_x\text{CoCrFeNiMn}$ alloy.

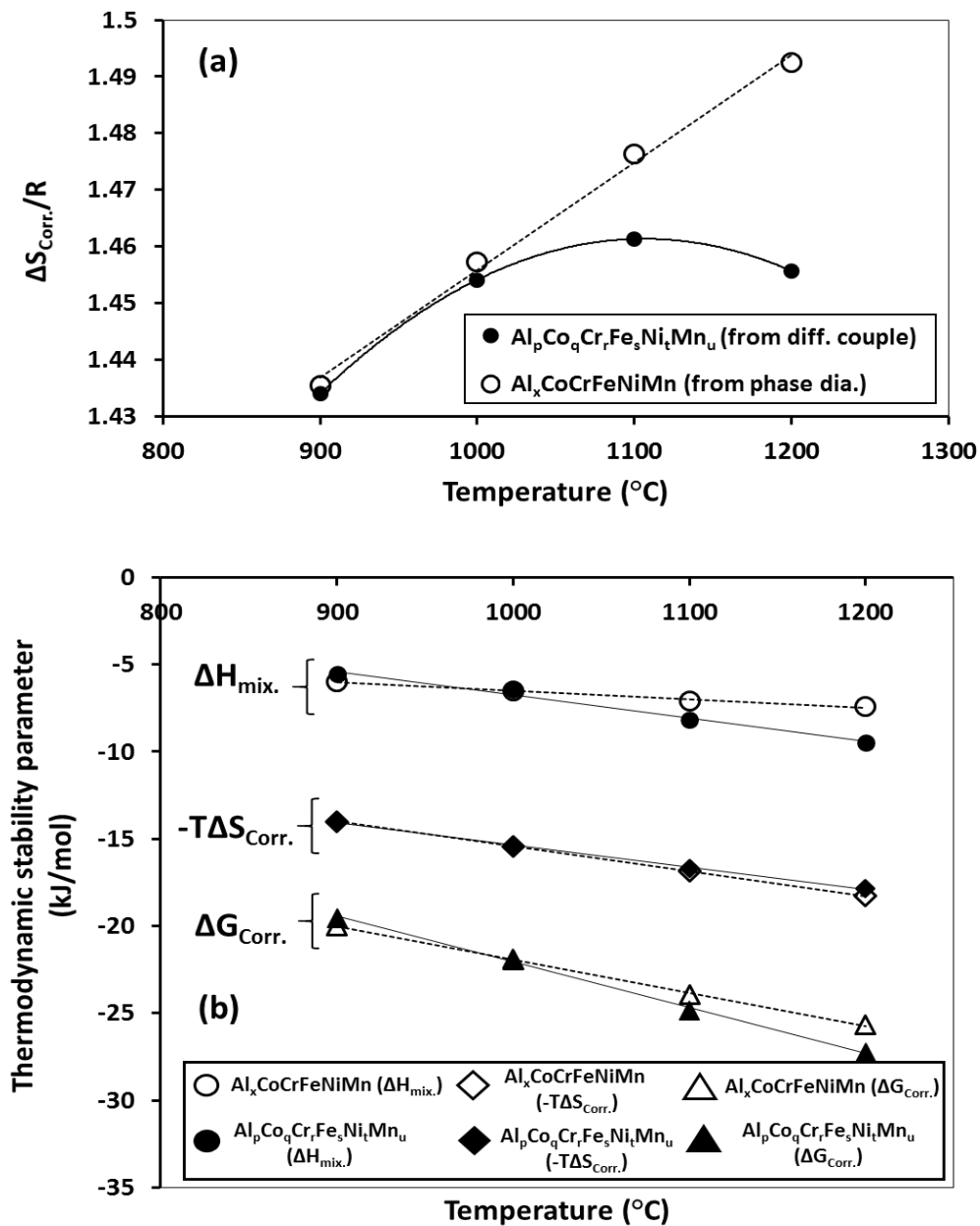


Figure 22. (a) Comparison of correlated entropy of mixing ($\Delta S_{\text{Corr.}}/R$) in $\text{Al}_p\text{Co}_q\text{Cr}_r\text{Fe}_s\text{Ni}_t\text{Mn}_u$ (using diffusion couple) and $\text{Al}_x\text{CoCrFeNiMn}$ (using phase diagram), (b) Comparison of correlated thermodynamic parameters measured in the $\text{Al}_p\text{Co}_q\text{Cr}_r\text{Fe}_s\text{Ni}_t\text{Mn}_u$ and $\text{Al}_x\text{CoCrFeNiMn}$

5.3 Role of Enthalpy of mixing

High entropy effect proposes that equiatomic alloys with random solid-solution microstructure has the highest entropy of mixing, exhibit the higher thermodynamic stability at high temperatures. Generally for transition metal HEAs, $|-T\Delta S_{\text{mix}}| > |\Delta H_{\text{mix}}|$, therefore entropic contribution is more significant at higher temperatures than enthalpy contribution towards the stability (ΔG_{mix}) of HEAs. This also referred to as *entropic stabilization* of an alloy which is typically achievable with minimum of four components in equal amount. Role of enthalpy is typically not discussed when comparing HEAs with similar constituent elements but different compositions as composition corresponding to higher entropy is presumed to be more stable than composition corresponding to the lower entropy.

With an exception to above discussion, compositions of off-equiatomic alloy corresponding to highest solubility limit for Al is thermodynamically observed to be more stable than equiatomic composition in Al-Co-Cr-Fe-Ni and Al-Co-Cr-Fe-Ni-Mn alloys at 1100°C and above temperatures. In these alloys, entropy of mixing always plays the vital role in stabilizing the single phase, as entropic contribution is significantly larger than enthalpy contribution towards the overall free energy of mixing as shown in Figure 16(b), Figure 17(b), Figure 21(b), and Figure 22(b). However, role of enthalpy of mixing cannot be neglected which resulted in higher thermodynamic stability of off-equiatomic alloy compositions than equiatomic alloys compositions. Therefore, it directly contradicts the general presumption that entropy is the sole contributor towards the higher thermodynamic stability of equiatomic HEAs. Enthalpy

contributions may be significant in some alloys and sometimes results in higher thermodynamic stability of off-equiatomic alloy compositions than their equiatomic counterparts.

At 1100°C and above temperatures, solubility limit of Al in off-equiatomic composition is higher than the solubility limit of Al in equiatomic composition. Binary pair enthalpy of mixing ($\Delta H_{ij}^{\text{mix}}$) of Al with other elements is strongly negative in comparison to $\Delta H_{ij}^{\text{mix}}$ values for other binary pair constituent elements in both Al-Co-Cr-Fe-Ni and Al-Co-Cr-Fe-Ni-Mn system, as shown in Table 7. Therefore, increase in amount of Al, at 1100°C and higher temperatures, in off-equiatomic alloys significant increases the magnitude of ΔH_{mix} of overall alloy composition in comparison to equiatomic alloy. Table 8 and Table 9 compares the variation in solubility limit of all elements in FCC $\text{Al}_p\text{Co}_q\text{Cr}_r\text{Fe}_s\text{Ni}_t$ and $\text{Al}_p\text{Co}_q\text{Cr}_r\text{Fe}_s\text{Ni}_t\text{Mn}_u$ alloys, respectively. It can be observed that solubility limit of Ni also increase while solubility limit of Co, Cr, Fe and Ni decreases with increases in temperature in both alloys. However, increase in amount of Ni, may not significantly influence the ΔH_{mix} of overall alloy, unless it has strong negative binary pair enthalpy of mixing ($\Delta H_{ij}^{\text{mix}}$) with other elements.

Table 7. Binary enthalpy of mixing calculated by Miedema's model for atomic pair between elements *i* and *j* in various Co-Cr-Fe-Ni based alloy systems.

Alloy systems							
AlCoCrFeNiMn		AlCoCrFeNi		CoCrFeNiMn		CoCrFeNiCu	
Binary Pairs (i-j)	$\Delta H_{ij}^{\text{mix}}$ (kJ/mol)	Binary Pairs (i-j)	$\Delta H_{ij}^{\text{mix}}$ (kJ/mol)	Binary Pairs (i-j)	$\Delta H_{ij}^{\text{mix}}$ (kJ/mol)	Binary Pairs (i-j)	$\Delta H_{ij}^{\text{mix}}$ (kJ/mol)
Al-Co	-19	Al-Co	-19	Mn-Co	-5	Cu-Co	6
Al-Cr	-10	Al-Cr	-10	Mn-Cr	2	Cu-Cr	12
Al-Fe	-11	Al-Fe	-11	Mn-Fe	0	Cu-Fe	13
Al-Ni	-22	Al-Ni	-22	Mn-Ni	-8	Cu-Ni	4
Al-Mn	-19	Co-Cr	-4	Co-Cr	-4	Co-Cr	-4
Mn-Co	-5	Co-Fe	-1	Co-Fe	-1	Co-Fe	-1
Mn-Cr	2	Co-Ni	0	Co-Ni	0	Co-Ni	0
Mn-Fe	0	Cr-Fe	-1	Cr-Fe	-1	Cr-Fe	-1
Mn-Ni	-8	Cr-Ni	-7	Cr-Ni	-7	Cr-Ni	-7
Co-Cr	-4	Fe-Ni	-2	Fe-Ni	-2	Fe-Ni	-2
Co-Fe	-1						
Co-Ni	0						
Cr-Fe	-1						
Cr-Ni	-7						
Fe-Ni	-2						

Table 8. Compositions of $\text{Al}_p\text{Co}_q\text{Cr}_r\text{Fe}_s\text{Ni}_t$ alloy corresponding to the maximum solubility limit of Al

Temperature (°C)	Composition corresponding to maximum solubility limit of Al (at. %)				
	Al	Cr	Fe	Co	Ni
900	4.08 (0.46)	25.83 (0.16)	24.86 (0.24)	22.25 (0.08)	22.98 (0.32)
1000	5.48 (0.29)	25.44 (0.21)	23.86 (0.19)	20.91 (0.10)	24.30 (0.23)
1100	8.57 (0.25)	25.19 (0.13)	20.72 (0.23)	17.65 (0.12)	27.85 (0.17)
1200	10.42 (0.27)	23.15 (0.37)	20.01 (0.14)	15.99 (0.15)	30.44 (0.15)

Table 9. Compositions of $\text{Al}_p\text{Co}_q\text{Cr}_r\text{Fe}_s\text{Ni}_t\text{Mn}_u$ alloy corresponding to the maximum solubility limit of Al

Temperature (°C)	Composition corresponding to maximum solubility limit of Al (at.%)					
	Al	Cr	Mn	Fe	Co	Ni
900	3.07 (0.02)	23.21 (0.34)	12.86 (0.14)	23.47 (0.04)	17.95 (0.27)	19.50 (0.16)
1000	4.39 (0.17)	23.09 (0.23)	12.78 (0.17)	21.36 (0.35)	16.79 (0.12)	21.65 (0.48)
1100	7.24 (0.12)	21.67 (0.18)	12.40 (0.34)	18.84 (0.06)	14.97 (0.19)	24.93 (0.37)
1200	9.42 (0.12)	19.43 (0.14)	12.48 (0.13)	17.12 (0.23)	13.25 (0.46)	28.30 (0.19)

Binary pair enthalpy of mixing ($\Delta H_{ij}^{\text{mix}}$) can provide an approximate estimate, if the addition of new element will form the solid solution in the existing single phase alloy. Equiatomic CoCrFeNi is a single phase HEA [65]. If the new element has a significant negative enthalpy of mixing with each of the other four existing component then overall alloy composition has a tendency to precipitate second phase (i.e. intermetallic compounds, second phase). On other hand, if new element has a significant positive enthalpy of mixing of all binary pairs then phase separation tendency will dominate. Table 7 compares the binary pair enthalpy of mixing calculated by Miedema's model for Al-Co-Cr-Fe-Ni-Mn, Al-Co-Cr-Fe-Ni, Co-Cr-Fe-Ni-Mn and Co-Cr-Fe-Ni-Cu alloys. It is evident from the Table 7 that addition of Al to CoCrFeNi or CoCrFeNiMn beyond solubility limit will result in formation of second phase while addition of Cu will result in phase separation (i.e. miscibility gap) and form two FCC phases [66]. Addition of Mn with the moderate binary pair enthalpy of mixing will maintain the overall single phase solid solution microstructure near equiatomic composition [65]. It is interesting to note that further increase in Al content in $\text{Al}_x\text{CoCrFeNi}$ ($x > 0.88$) or $\text{Al}_x\text{CoCrFeNiMn}$ ($x > 1.25$) will result in BCC structure

which had been attributed increase in lattice distortion due to large atomic radius of Al [67]. However, second phase BCC particles still exist in BCC matrix of $\text{Al}_x\text{CoCrFeNi}$ ($x > 0.88$) [68].

5.4 Application of Solid solution formation rules to off-equiatomic compositions generated in diffusion couples

High throughput combinatorial diffusion couple approach allows the study of many composition in a single experiment. To better understand the phase stability of various off-equiatomic $\text{Al}_x\text{Co}_p\text{Cr}_q\text{Fe}_r\text{Ni}_s$ and $\text{Al}_p\text{Co}_q\text{Cr}_r\text{Fe}_s\text{Ni}_t\text{Mn}_u$ compositions, results were compared against existing empirical phase selection rules pertaining to multi-component alloys, as described in section 3.3. Atomic size difference (δ) plays the important role for the formation of single phase solid solution in HEAs. Therefore, all the solid solution phase formation predictors are plotted against δ , as shown in Figure 23 and Figure 24. Figure 23 (a) and Figure 24 (a) shows the Ω - δ plot for the all off-equiatomic $\text{Al}_x\text{Co}_p\text{Cr}_q\text{Fe}_r\text{Ni}_s$ and $\text{Al}_p\text{Co}_q\text{Cr}_r\text{Fe}_s\text{Ni}_t\text{Mn}_u$ alloys. It can be noticed the Ω varies between 2 and 5 and δ varies between 0.006 and 0.046. Smaller mismatch ($\delta \leq 0.066$) in atomic size [53, 69] and $\Omega \geq 1.1$ [53] has been suggested as a criterion for forming solid solution in HEAs. Figure 23 (b) and Figure 24 (b) shows that $\Delta H_{\text{mix.}} - \delta$ plot, which suggests that $\Delta H_{\text{mix.}}$ for FCC AlCoCrFeNi alloys varies from -8.8 to -3.8 kJ/mol. Guo et al. [69] reported that ΔH_{mix} for single phase HEAs varies between -11.6 to 3.2 kJ/mol and corresponding δ values are small (< 0.066). VEC also plays an important role in determining structure of HEAs. Smaller values of VEC favors the formation of BCC phases while higher VEC favors the formation of FCC phases. Guo et al. [56] observed that for FCC HEAs, $\text{VEC} \geq 8.0$, however, Poletti & Battezzatti [70] suggested that $\text{VEC} > 7.5$. Figure 23 (c) and Figure 24 (c) shows that VEC of $\text{Al}_x\text{Co}_p\text{Cr}_q\text{Fe}_r\text{Ni}_s$ and

$\text{Al}_p\text{Co}_q\text{Cr}_r\text{Fe}_s\text{Ni}_t\text{Mn}_u$ alloys, respectively, varies between 7.6 and 8.25. In general, $\Delta\chi$ does not have the strong effect in determining the phases in HEAs. Small $\Delta\chi$ (≤ 0.175) favors the formation of solid solution [71], however many exceptions were also reported to this rule [72]. In present work, $\Delta\chi$ varies between 0.07 and 0.116, as shown in Figure 23 (d) and Figure 24 (d) for $\text{Al}_x\text{Co}_p\text{Cr}_q\text{Fe}_r\text{Ni}_s$ and $\text{Al}_p\text{Co}_q\text{Cr}_r\text{Fe}_s\text{Ni}_t\text{Mn}_u$ alloys, respectively.

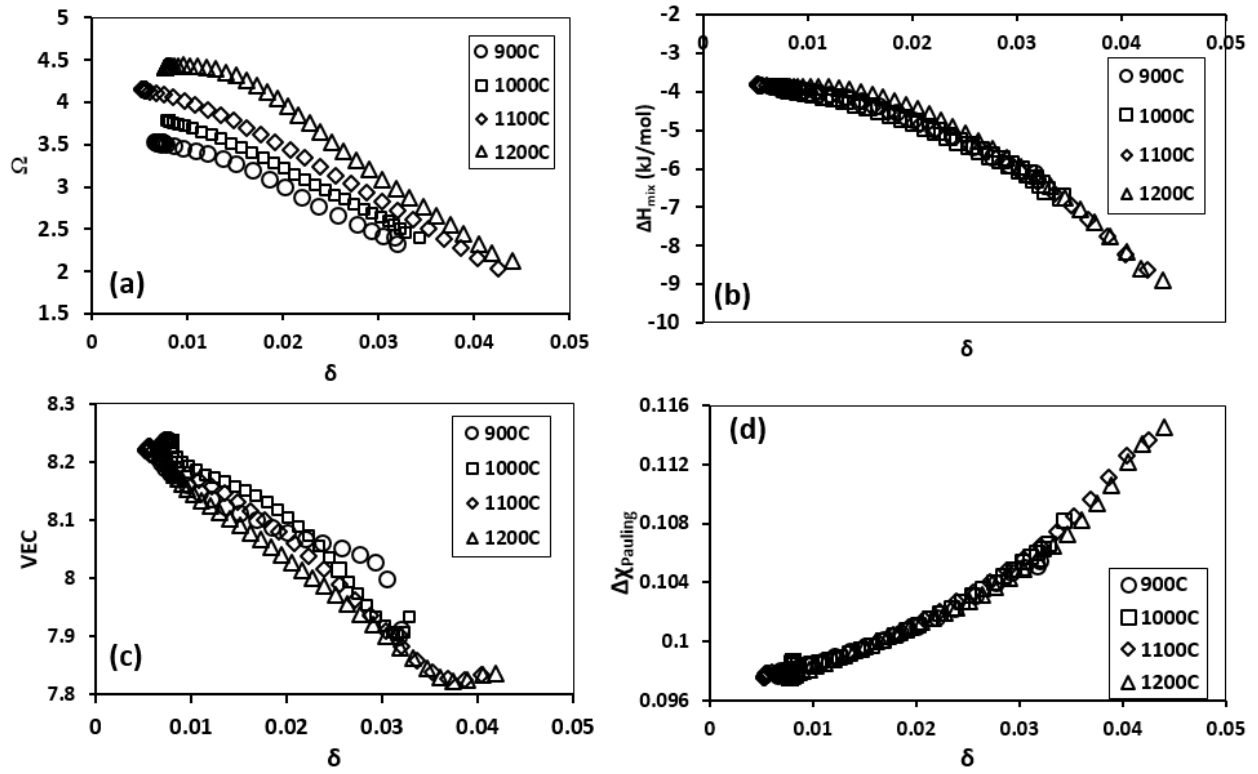


Figure 23. Application of solid-solubility predictors to the various off-equiatomic FCC $\text{Al}_p\text{Co}_q\text{Cr}_r\text{Fe}_s\text{Ni}_t$ generated in the diffusion couples. (a) Ω - δ , (b) ΔH_{mix} - δ , (c) VEC- δ , and (d) $\Delta\chi$ - δ plot.

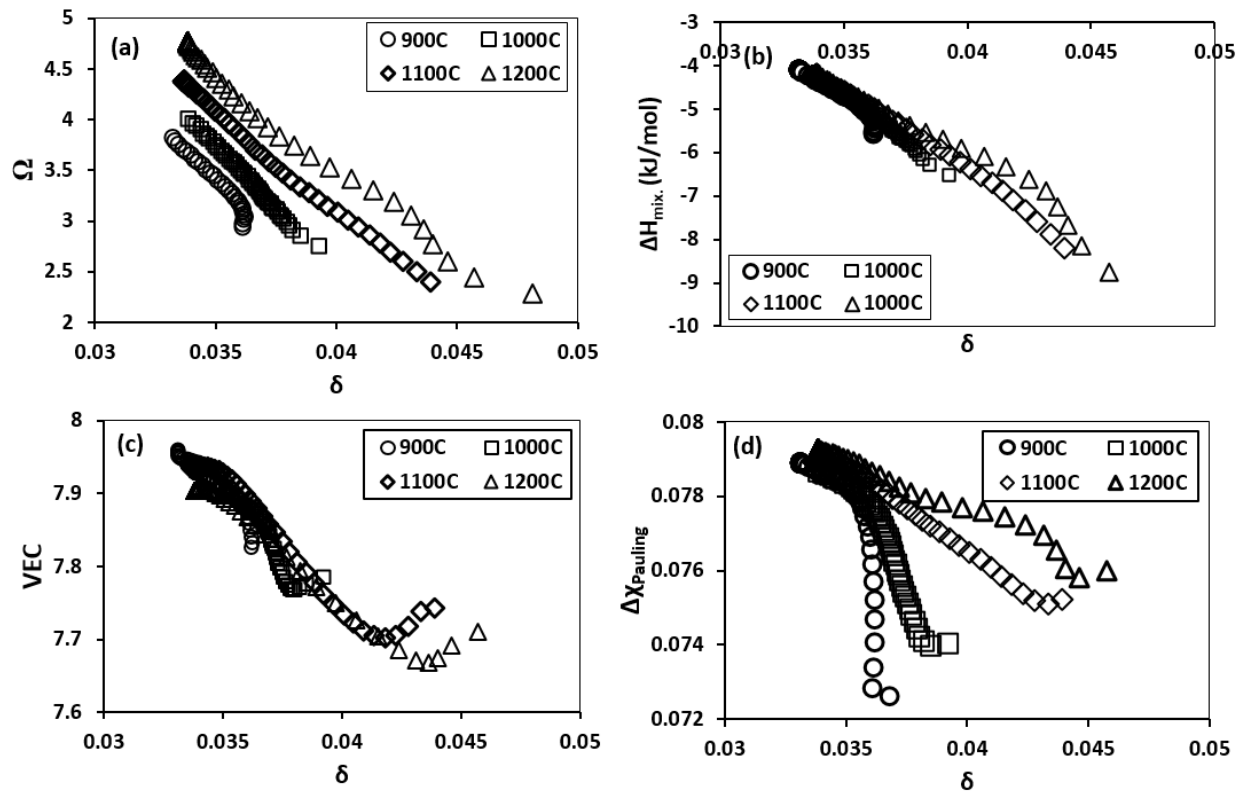


Figure 24. Application of solid-solubility predictors to the various off-equiatom FCC $\text{Al}_p\text{Co}_q\text{Cr}_r\text{Fe}_s\text{Ni}_t\text{Mn}_u$ generated in the diffusion couples. (a) Ω - δ , (b) ΔH_{mix} - δ , (c) VEC- δ , and (d) $\Delta\chi$ - δ plot.

CHAPTER 6 SLUGGISH DIFFUSION EFFECT

Aforementioned in chapter 2, diffusion is proposed to be anomalously slow in HEAs. Initially this hypothesis may mainly motivated by the secondary observations such as absence of low temperature phases in $\text{Al}_{0.5}\text{CoCrFeNiCu}$ upon slow cooling from high temperature [73], restricted growth of nano-crystals in as-cast $\text{Al}_x\text{CoCrFeNiCu}$ alloy [22], or AlCrMoSiTi film [23]. Superior diffusion barrier properties of AlMoNbSiTaTiVZr [74], AlCrTaTiNi , $(\text{AlCrTaTiNi})\text{N}$ [75], $(\text{AlMoNbSiTaTiVZr})_{50}\text{N}_{50}$ [76], $(\text{AlCrTaTiZr})\text{N}$ [77], AlMoNbSiTaTiVZr [74] also support sluggish diffusion hypothesis. Some alloys such as CoCrFeNiMn [78-80], $\text{Al}_{0.5}\text{CoCrFeNiCu}$ [81], $\text{Al}_{0.5}\text{CrCuFeNi}_2$ [82], FeCoNiCuMn [83] exhibit sluggish recrystallization kinetics also advocate towards sluggish diffusion behavior. These secondary observations supported the sluggish diffusion hypothesis, however does not prove that diffusion is indeed sluggish in all HEAs. Aforementioned, various studies [21, 25, 31-33, 35-37] has been carried out to determine the tracer diffusion coefficients. There has been no common consensus on the sluggish diffusion hypothesis: some studies reported that diffusion is indeed sluggish in HEAs while others did not. In potential engineering applications where diffusion may occur under the concentration gradients, interdiffusion coefficients may be more relevant. Limited studies [30, 32, 34] has been reported on the interdiffusion in HEAs, however no relevant comparison was made to elucidate the possible “sluggish” diffusion in HEAs.

In this chapter, sluggish diffusion effect was examined in single phase Co-Cr-Fe-Ni based transition metal high entropy alloys by measuring interdiffusion and tracer diffusion coefficients.

Average effective interdiffusion coefficients were measured for individual elements in Co-Cr-Fe-Ni, Co-Cr-Fe-Ni-Mn, Al-Co-Cr-Fe-Ni and Al-Co-Cr-Fe-Ni-Mn. Tracer diffusion coefficient of Ni was measured in face centered cubic Co-Cr-Fe-Ni, Co-Cr-Fe-Ni-Mn, and Al-Co-Cr-Fe-Ni. Diffusion coefficients in HEAs were compared with the conventional solvent-based multicomponent low entropy alloys to investigate sluggish diffusion effect. Results were analyzed with respect to the fluctuation in lattice potential energy of the system under study using potential energy fluctuation (PEF) model.

6.1 Measurement of average effective interdiffusion coefficients

6.1.1 Fe₅₀Cr₅₀ vs. Co₅₀Ni₅₀ quaternary diffusion couples

Figure 25 shows the concentration profiles superimposed on the BSE microstructure of Fe₅₀Cr₅₀ vs. Co₅₀Ni₅₀ diffusion couples isothermally annealed at 900°, 1000°, 1100°, and 1200°C for 120, 120, 48, and 48 hours, respectively. Two-phase region was observed in the interdiffusion zone of the diffusion couple annealed at 900°C, as shown in Figure 25(a). Interdiffusion zone consist of continuous intermetallic layer, with composition: 47.09 at.% Cr, 45.27 at.% Fe, 4.41 at.% Co and 3.23 at.% Ni, along with some Cr rich precipitates, with composition: 85.62 at.% Cr, 11.79 at.% Fe, 0.69 at.% Co and 1.91 at.% Ni). Other diffusion couples exhibited interphase boundary between BCC and FCC alloys with sharp changes in concentrations.

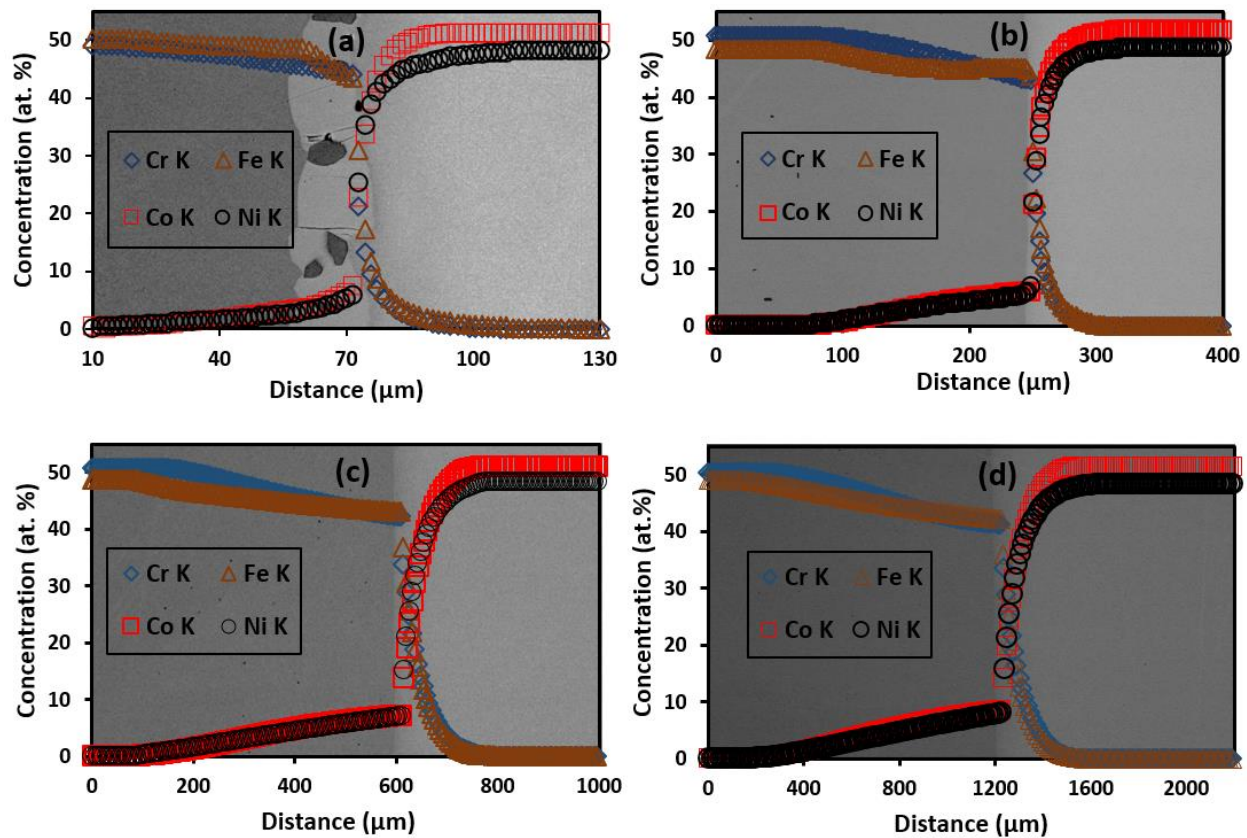


Figure 25. Concentration profiles superimposed on BSE micrographs of Fe₅₀Cr₅₀ vs. Co₅₀Ni₅₀ diffusion couples isothermally annealed at (a) 900°C for 120 hours, (b) 1000°C for 120 hours, (c) 1100°C for 48 hours, and (d) 1200°C for 48 hours

Table 10 reports the average effective interdiffusion coefficients, activation energies, and pre-exponential factor of Co, Cr, Fe and Ni in the starting BCC Fe₅₀Cr₅₀ and FCC Co₅₀Ni₅₀ alloy at 900, 1000, 1100, and 1200°C. Figure 26 shows the corresponding Arrhenius plot for the temperature dependence of average effective interdiffusion coefficients. Table 10 and Figure 26 shows that interdiffusion coefficients of Co, Cr, Fe and Ni were 1-2 order of magnitude higher in BCC phase, in comparison to FCC phase. It is noteworthy that after interdiffusion, equiatomic

composition of CoCrFeNi forms on the FCC side of the diffusion couple. Diffusion of Co and Ni in BCC FeCr alloys shows the limited solubility limit for Co and Ni.

Table 10. Average effective interdiffusion coefficients, activation energy and pre-exponential factor of Co, Cr, Fe, and Ni measured in FeCr (BCC) and CoNi (FCC) phases measured using Fe₅₀Cr₅₀ vs. Co₅₀Ni₅₀ diffusion couples

End member Alloy Diffusion couple	Temperature (°C)	\bar{D}_{Cr}^{eff} (m ² /s)	\bar{D}_{Fe}^{eff} (m ² /s)	\bar{D}_{Co}^{eff} (m ² /s)	\bar{D}_{Ni}^{eff} (m ² /s)
Fe ₅₀ Cr ₅₀	900	$5.35 (2.72) \times 10^{-16}$	$1.02 (0.44) \times 10^{-15}$	$7.23 (4.01) \times 10^{-16}$	$7.51 (3.86) \times 10^{-16}$
	1000	$1.14 (0.47) \times 10^{-14}$	$2.29 (1.00) \times 10^{-14}$	$1.66 (0.83) \times 10^{-14}$	$1.83 (0.87) \times 10^{-14}$
	1100	$1.66 (0.42) \times 10^{-13}$	$2.25 (0.76) \times 10^{-13}$	$2.24 (0.61) \times 10^{-13}$	$2.14 (0.63) \times 10^{-13}$
	1200	$7.98 (0.13) \times 10^{-13}$	$1.13 (0.05) \times 10^{-12}$	$9.70 (0.10) \times 10^{-13}$	$8.63 (0.29) \times 10^{-13}$
	Q (kJ/mol)	355.42	336.97	350.19	341.79
	D₀ (m²/s)	4.0829	1.2456	3.3791	1.5602
Co ₅₀ Ni ₅₀	900	$1.21 (0.63) \times 10^{-16}$	$1.25 (0.45) \times 10^{-16}$	$1.17 (0.65) \times 10^{-16}$	$1.27 (0.56) \times 10^{-16}$
	1000	$6.71 (3.77) \times 10^{-16}$	$7.32 (2.97) \times 10^{-16}$	$7.09 (3.82) \times 10^{-16}$	$7.26 (3.72) \times 10^{-16}$
	1100	$9.58 (1.03) \times 10^{-15}$	$7.96 (0.75) \times 10^{-15}$	$8.69 (0.97) \times 10^{-15}$	$9.14 (1.32) \times 10^{-15}$
	1200	$3.42 (0.04) \times 10^{-14}$	$2.84 (0.08) \times 10^{-14}$	$3.08 (0.10) \times 10^{-14}$	$3.30 (0.03) \times 10^{-14}$
	Q (kJ/mol)	281.18	268.13	276.19	275.94
	D₀ (m²/s)	3.45×10^{-4}	9.80×10^{-5}	2.10×10^{-4}	2.16×10^{-4}

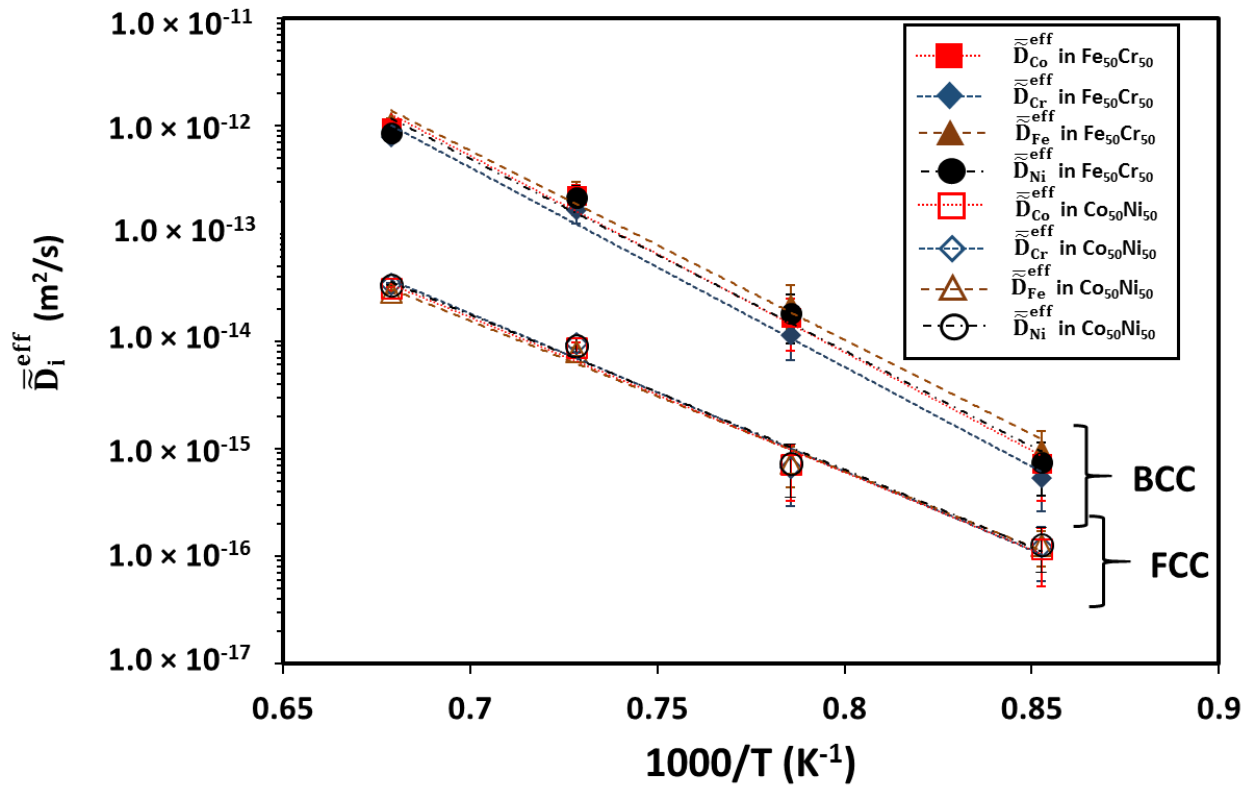


Figure 26. Temperature dependence of average effective interdiffusion coefficients for Co, Cr, Fe and Ni in BCC FeCr alloy and FCC CoNi measured using Fe₅₀Cr₅₀ vs. Co₅₀Ni₅₀ diffusion couples in temperature range from 900° to 1200°C.

6.1.2 Co₂₀Cr₂₇Fe₃₃Ni₂₀ vs Co₃₀Cr₂₀Fe₂₀Ni₃₀ quaternary diffusion couples

Figure 27 shows the concentration profiles superimposed on the BSE microstructure of Co₂₀Cr₂₇Fe₃₃Ni₂₀ vs Co₃₀Cr₂₀Fe₂₀Ni₃₀ diffusion couples annealed at 900°, 1000°, 1100°, and 1200°C for 240, 240, 240, and 48 hours, respectively. Interdiffusion zone in all the diffusion couples exhibited the single-phase microstructure without any interphase boundary. Diffusion

couples annealed at 1000°, 1100°, and 1200°C showed the formation of Kirkendall voids in the interdiffusion zone.

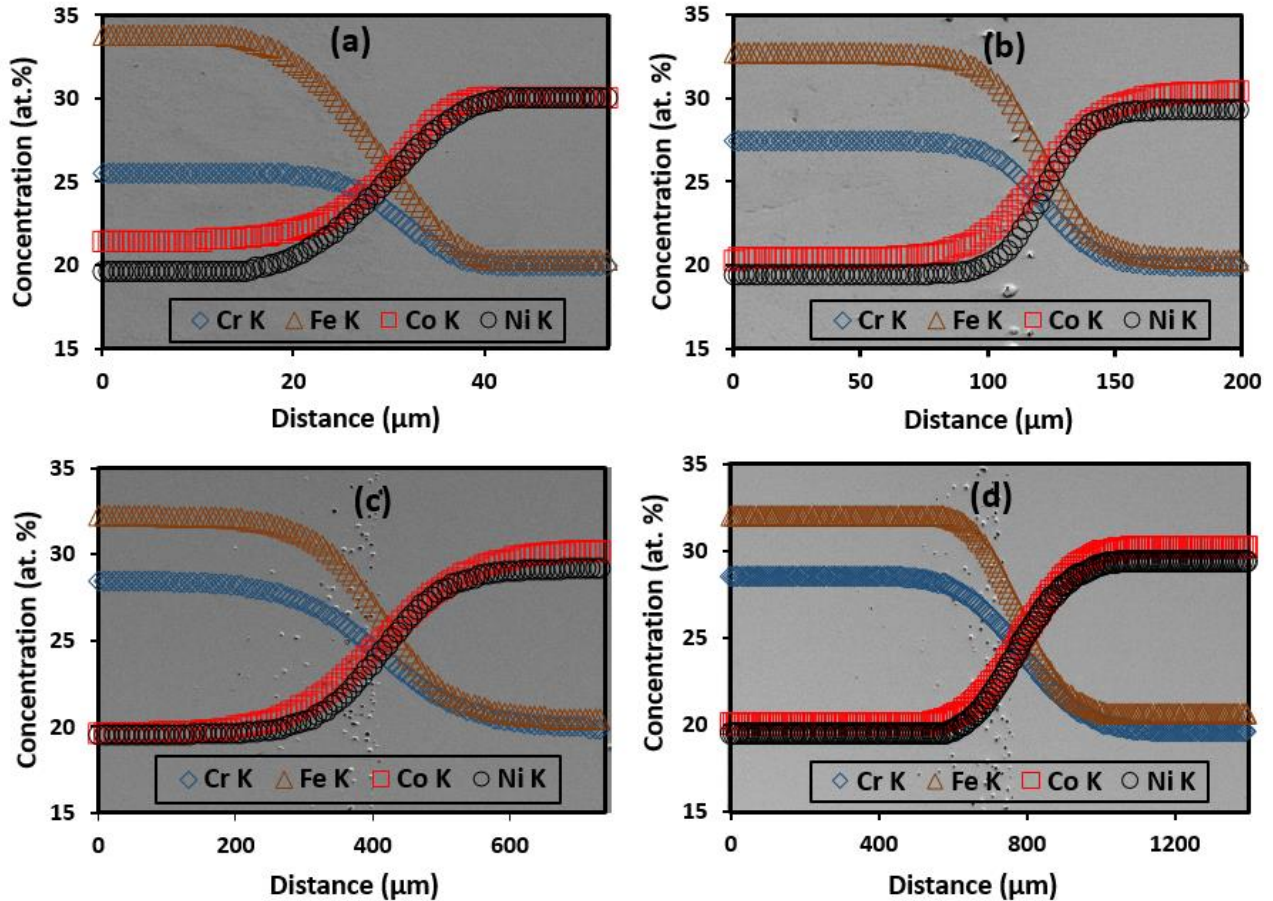


Figure 27. Concentration profiles superimposed on BSE micrographs of $\text{Co}_{20}\text{Cr}_{27}\text{Fe}_{33}\text{Ni}_{20}$ vs $\text{Co}_{30}\text{Cr}_{20}\text{Fe}_{20}\text{Ni}_{30}$ diffusion couples isothermally annealed at (a) 900°C for 240 hours, (b) 1000°C for 240 hours, (c) 1100°C for 240 hours, and (d) 1200°C for 48 hours.

Table 11 reports the average effective interdiffusion coefficients, activation energies, and pre-exponential factor of Co, Cr, Fe and Ni in CoCrFeNi alloy for the near equiatomic composition measured using $\text{Co}_{20}\text{Cr}_{27}\text{Fe}_{33}\text{Ni}_{20}$ vs $\text{Co}_{30}\text{Cr}_{20}\text{Fe}_{20}\text{Ni}_{30}$ diffusion couples at 900°, 1000°, 1100°, and

1200°C. Figure 28 shows the corresponding Arrhenius plot for the temperature dependence of average effective interdiffusion coefficients. In general, Cr is the fastest, and Ni is the slowest diffusing element in the CoCrFeNi alloy.

Table 11. Average effective interdiffusion coefficients, activation energy and pre-exponential factor of Co, Cr, Fe and Ni in CoCrFeNi alloy for the near equiatomic composition measured using Co₂₀Cr₂₇Fe₃₃Ni₂₀ vs Co₃₀Cr₂₀Fe₂₀Ni₃₀.

Temperature (°C)	\bar{D}_{Cr}^{eff} (m ² /s)	\bar{D}_{Fe}^{eff} (m ² /s)	\bar{D}_{Co}^{eff} (m ² /s)	\bar{D}_{Ni}^{eff} (m ² /s)
900	$1.68 (0.92) \times 10^{-17}$	$1.81(0.41) \times 10^{-17}$	$1.73 (0.67) \times 10^{-17}$	$1.37 (0.36) \times 10^{-17}$
1000	$2.52 (0.51) \times 10^{-16}$	$2.21 (0.29) \times 10^{-16}$	$2.09 (0.68) \times 10^{-16}$	$1.62 (0.33) \times 10^{-16}$
1100	$7.45 (0.69) \times 10^{-15}$	$4.37 (0.27) \times 10^{-15}$	$5.88 (0.15) \times 10^{-15}$	$4.09 (0.33) \times 10^{-15}$
1200	$4.41 (0.49) \times 10^{-14}$	$3.05 (0.31) \times 10^{-14}$	$3.11 (0.27) \times 10^{-14}$	$2.41 (0.13) \times 10^{-14}$
\bar{Q}_i^{eff} (kJ/mol)	388.46	362.94	371.38	368.41
$\bar{D}_{0,i}^{eff}$ (m ² /s)	3.0495	0.2319	0.53012	0.307

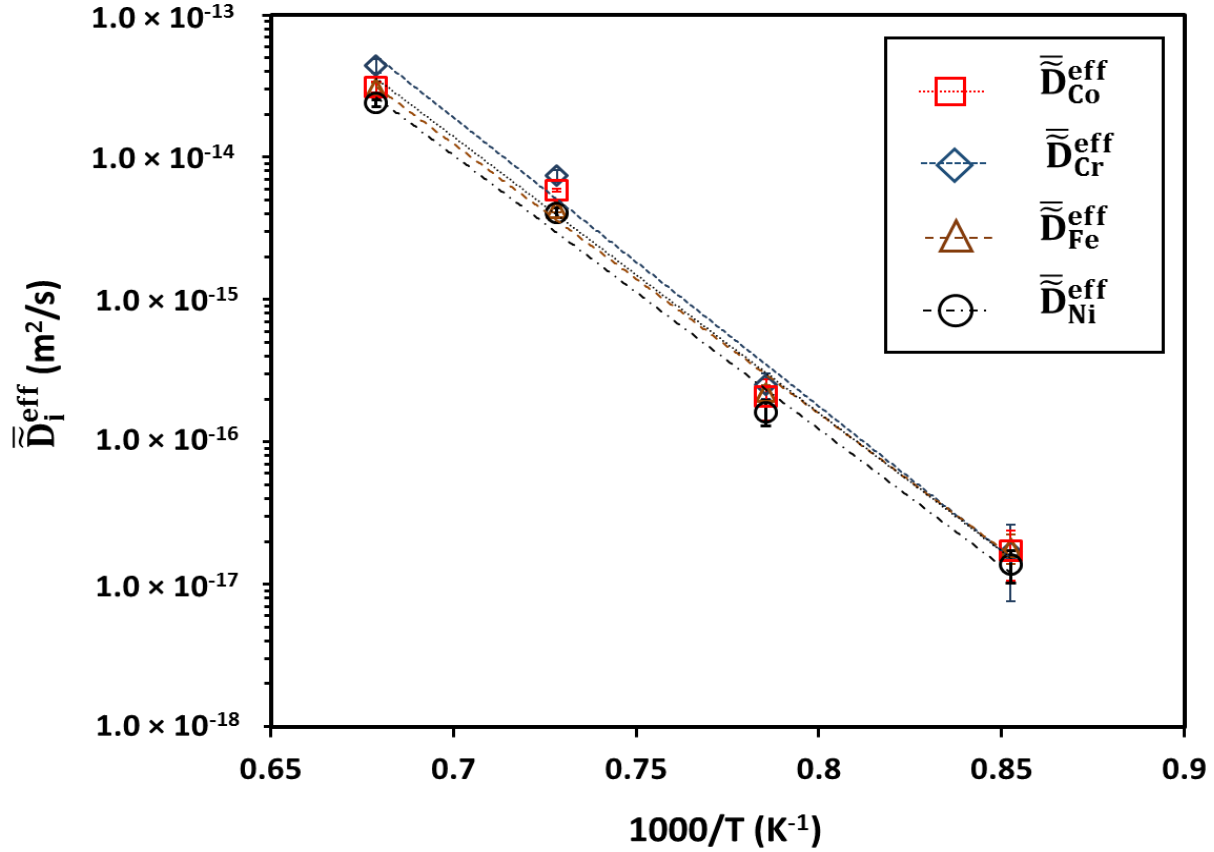


Figure 28. Temperature dependence of average effective interdiffusion coefficients for Co, Cr, Fe and Ni in $Co_{20}Cr_{27}Fe_{33}Ni_{20}$ vs $Co_{30}Cr_{20}Fe_{20}Ni_{30}$ diffusion couples in temperature range from 900° to 1200°C.

6.1.3 $Co_{25}Cr_{25}Ni_{25}Fe_{15}Mn_{10}$ vs $Co_{15}Cr_{15}Ni_{15}Fe_{25}Mn_{30}$ quinary diffusion couples

Figure 29 shows the concentration profiles superimposed on the microstructure of $Co_{25}Cr_{25}Ni_{25}Fe_{15}Mn_{10}$ vs $Co_{15}Cr_{15}Ni_{15}Fe_{25}Mn_{30}$ diffusion couples isothermally annealed at 900°, 1000°, 1100°, and 1200°C for 120, 120, 48, and 48 hours, respectively. Interdiffusion zone in all the diffusion couples exhibited the single-phase microstructure without any interphase boundary.

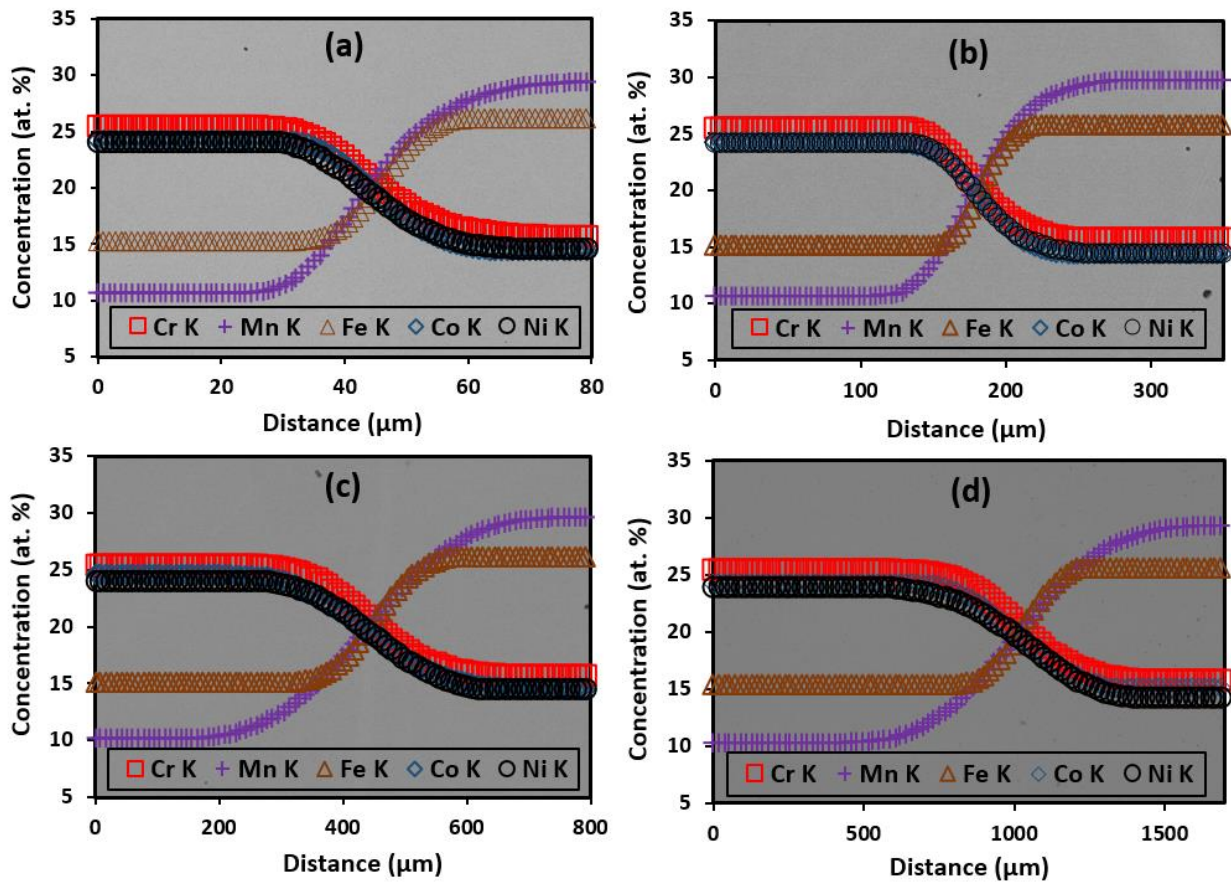


Figure 29. Concentration profiles superimposed on BSE micrographs of $\text{Co}_{25}\text{Cr}_{25}\text{Ni}_{25}\text{Fe}_{15}\text{Mn}_{10}$ vs $\text{Co}_{15}\text{Cr}_{15}\text{Ni}_{15}\text{Fe}_{25}\text{Mn}_{30}$ diffusion couples isothermally annealed at (a) 900°C for 120 hours, (b) 1000°C for 120 hours, (c) 1100°C for 48 hours, and (d) 1200°C for 48 hours.

Table 12. Average effective interdiffusion coefficients, activation energy and pre-exponential factor of Co, Cr, Fe and Ni in CoCrFeNiMn alloy for the near equiatomic composition measured using Co₂₅Cr₂₅Ni₂₅Fe₁₅Mn₁₀ vs Co₁₅Cr₁₅Ni₁₅Fe₂₅Mn₃₀ diffusion couples.

Temperature (°C)	\bar{D}_{Mn}^{eff} (m ² /s)	\bar{D}_{Cr}^{eff} (m ² /s)	\bar{D}_{Fe}^{eff} (m ² /s)	\bar{D}_{Co}^{eff} (m ² /s)	\bar{D}_{Ni}^{eff} (m ² /s)
900	$1.21 (0.08) \times 10^{-16}$	$8.06 (0.85) \times 10^{-17}$	$3.31 (0.99) \times 10^{-17}$	$6.23 (1.06) \times 10^{-17}$	$8.98 (1.86) \times 10^{-17}$
1000	$1.83 (0.13) \times 10^{-15}$	$7.26 (0.19) \times 10^{-16}$	$3.30 (0.48) \times 10^{-16}$	$7.71 (0.72) \times 10^{-16}$	$9.40 (1.40) \times 10^{-16}$
1100	$2.96 (0.12) \times 10^{-14}$	$1.60 (0.08) \times 10^{-14}$	$6.04 (2.01) \times 10^{-15}$	$1.58 (0.54) \times 10^{-14}$	$1.60 (0.46) \times 10^{-14}$
1200	$1.53 (0.09) \times 10^{-13}$	$8.58 (1.30) \times 10^{-14}$	$3.12 (0.56) \times 10^{-14}$	$8.03 (1.51) \times 10^{-14}$	$9.09 (0.13) \times 10^{-14}$
\bar{Q}_i^{eff} (kJ/mol)	348.86	344.62	337.13	352.68	338.96
$\bar{D}_{0,i}^{eff}$ (m ² /s)	0.4204	0.1520	0.0305	0.2965	0.1008

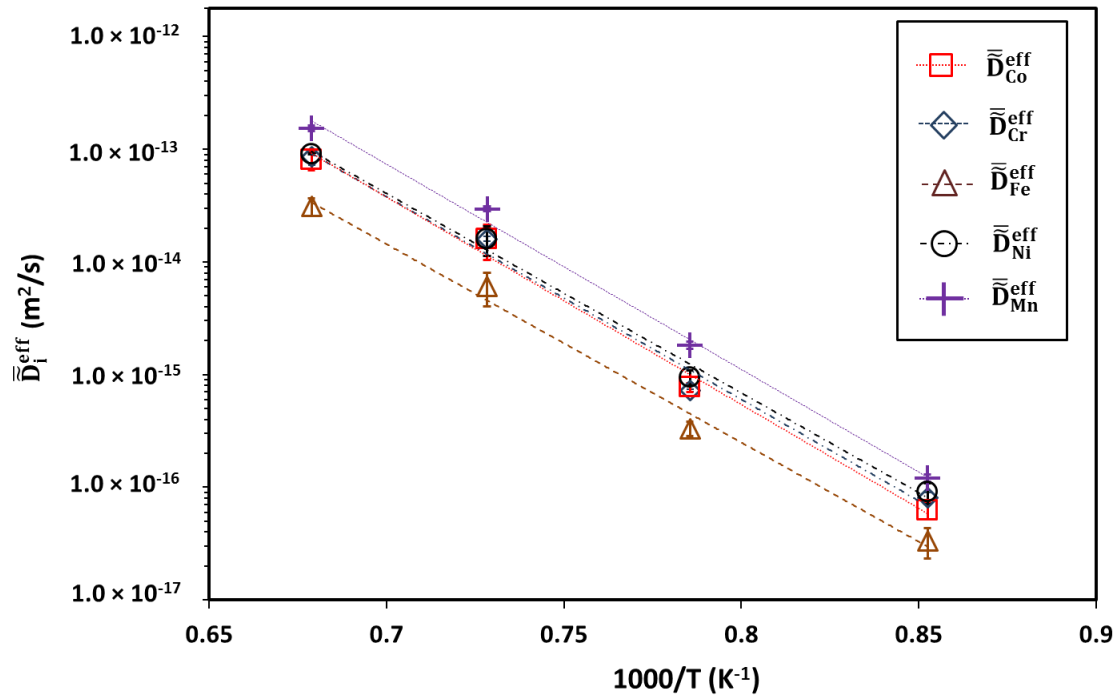


Figure 30. Temperature dependence of average effective interdiffusion coefficients for Co, Cr, Fe, Ni, and Mn in $Co_{25}Cr_{25}Ni_{25}Fe_{15}Mn_{10}$ vs $Co_{15}Cr_{15}Ni_{15}Fe_{25}Mn_{30}$ diffusion couples in temperature range from 900 to 1200°C.

Table 12 reports the average effective interdiffusion coefficients, activation energies, and pre-exponential factor of Co, Cr, Fe, Ni, and Mn in CoCrFeNiMn alloy for the near equiatomic composition measured using $Co_{25}Cr_{25}Ni_{25}Fe_{15}Mn_{10}$ vs $Co_{15}Cr_{15}Ni_{15}Fe_{25}Mn_{30}$ diffusion couples at 900, 1000, 1100, and 1200°C. Figure 30 shows the corresponding Arrhenius plot for the temperature dependence of average effective interdiffusion coefficients. In general, Mn is the fastest, and Fe is the slowest diffusing element in the CoCrFeNiMn alloy.

6.1.4 $\text{Al}_6\text{Co}_{19}\text{Cr}_{28}\text{Fe}_{28}\text{Ni}_{19}$ vs. $\text{Al}_6\text{Co}_{28}\text{Cr}_{19}\text{Fe}_{19}\text{Ni}_{28}$ quinary diffusion couples

Figure 31 shows the concentration profiles superimposed on the microstructure of $\text{Al}_6\text{Co}_{19}\text{Cr}_{28}\text{Fe}_{28}\text{Ni}_{19}$ vs. $\text{Al}_6\text{Co}_{28}\text{Cr}_{19}\text{Fe}_{19}\text{Ni}_{28}$ diffusion couples isothermally annealed at 900°C , 1000°C , 1100°C , and 1200°C for 240, 120, 48, and 24 hours, respectively. Interdiffusion zone in all the diffusion couples exhibited the single-phase microstructure without any interphase boundary.

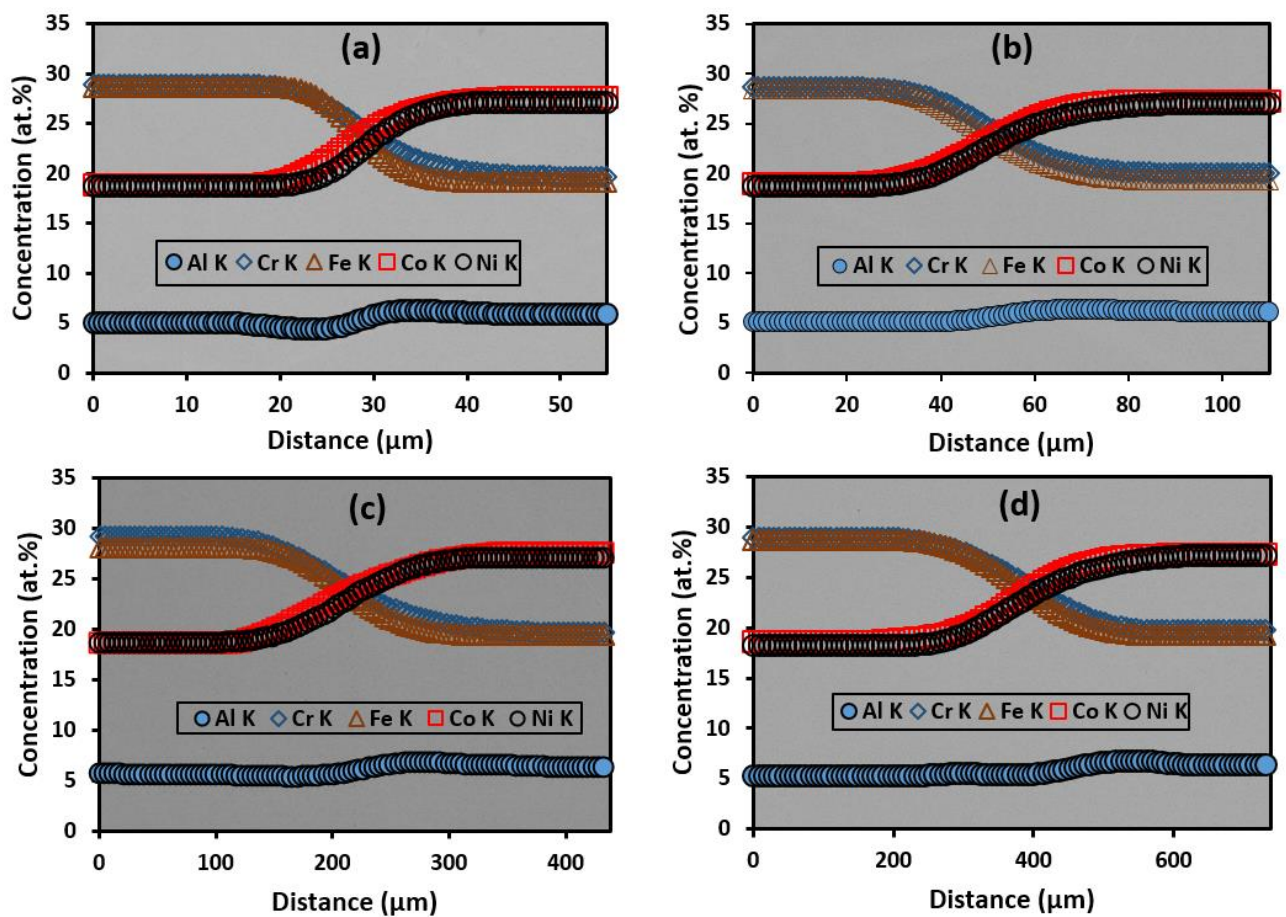


Figure 31. Concentration profiles superimposed on BSE micrographs of $\text{Al}_6\text{Co}_{19}\text{Cr}_{28}\text{Fe}_{28}\text{Ni}_{19}$ vs. $\text{Al}_6\text{Co}_{28}\text{Cr}_{19}\text{Fe}_{19}\text{Ni}_{28}$ diffusion couples isothermally annealed at (a) 900°C for 240 hours, (b) 1000°C for 120 hours, (c) 1100°C for 48 hours, and (d) 1200°C for 24 hours.

Table 13. Average effective interdiffusion coefficients, activation energy and pre-exponential factor of Al, Co, Cr, Fe and Ni in Al_{0.25}CoCrFeNi alloy composition measured using Al₆Co₁₉Cr₂₈Fe₂₈Ni₁₉ vs. Al₆Co₂₈Cr₁₉Fe₁₉Ni₂₈ diffusion couples.

Temperature (°C)	\bar{D}_{Al}^{eff} (m ² /s)	\bar{D}_{Cr}^{eff} (m ² /s)	\bar{D}_{Fe}^{eff} (m ² /s)	\bar{D}_{Co}^{eff} (m ² /s)	\bar{D}_{Ni}^{eff} (m ² /s)
900	$-2.95 (0.82) \times 10^{-16}$	$3.42 (0.41) \times 10^{-17}$	$1.76 (0.19) \times 10^{-17}$	$3.96 (0.80) \times 10^{-17}$	$3.32 (0.82) \times 10^{-17}$
1000	$-3.05 (0.43) \times 10^{-16}$	$3.73 (0.15) \times 10^{-16}$	$2.17 (0.21) \times 10^{-16}$	$3.94 (0.46) \times 10^{-16}$	$3.49 (0.18) \times 10^{-16}$
1100	$-2.49 (1.49) \times 10^{-14}$	$7.38 (0.91) \times 10^{-15}$	$3.95 (0.50) \times 10^{-15}$	$8.09 (0.99) \times 10^{-15}$	$6.33 (0.74) \times 10^{-15}$
1200	$-5.12 (3.35) \times 10^{-14}$	$3.63 (0.17) \times 10^{-14}$	$2.33 (0.42) \times 10^{-14}$	$3.67 (0.51) \times 10^{-14}$	$3.03 (0.32) \times 10^{-14}$
\bar{Q}_i^{eff} (kJ/mol)	-	343.62	351.60	338.29	335.72
$\bar{D}_{0,i}^{eff}$ (m ² /s)	-	0.0628	0.0739	0.0418	0.0276

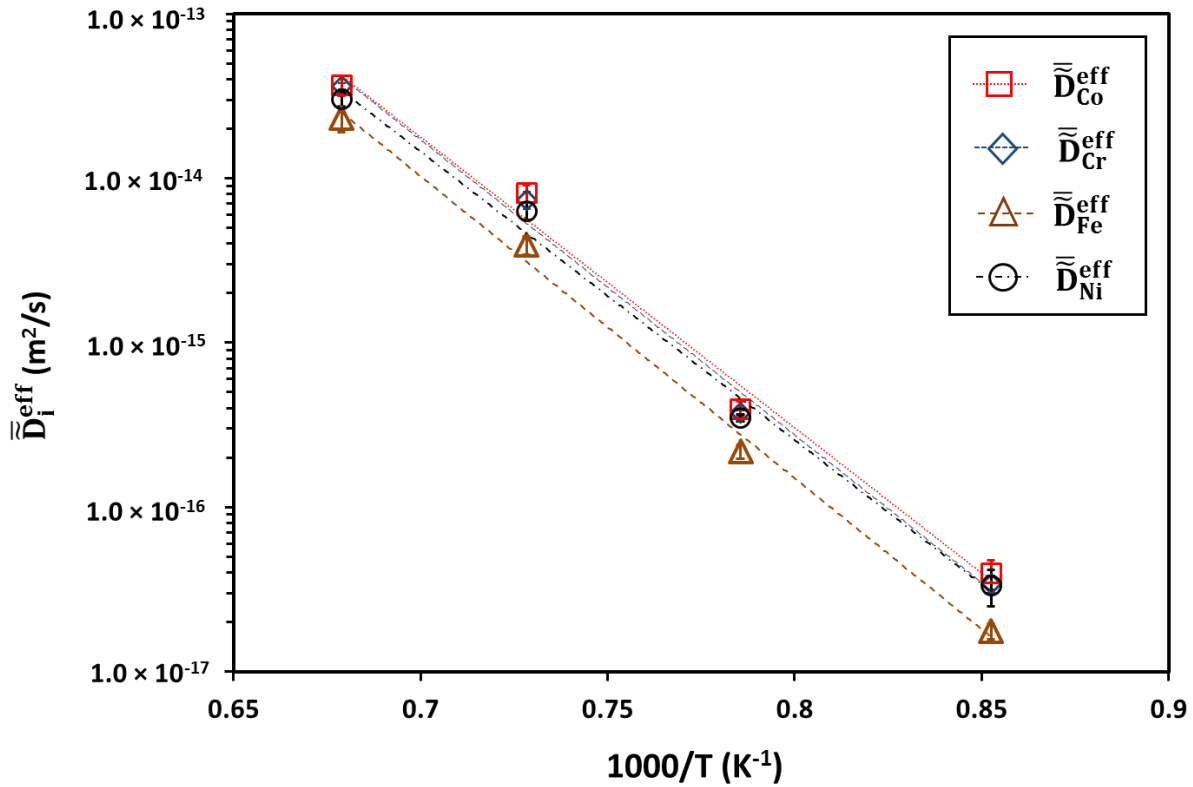


Figure 32. Temperature dependence of average effective interdiffusion coefficients for Co, Cr, Fe and Ni in $Al_6Co_{19}Cr_{28}Fe_{28}Ni_{19}$ vs. $Al_6Co_{28}Cr_{19}Fe_{19}Ni_{28}$ diffusion couples in temperature range from 900° to 1200°C.

Table 13 reports the average effective interdiffusion coefficients, activation energies, and pre-exponential factor of Co, Cr, Fe, Ni, and Mn in $Al_{0.25}CoCrFeNi$ alloy composition measured using $Al_6Co_{19}Cr_{28}Fe_{28}Ni_{19}$ vs. $Al_6Co_{28}Cr_{19}Fe_{19}Ni_{28}$ diffusion couples at 900°, 1000°, 1100°, and 1200°C. Figure 32 shows the corresponding Arrhenius plot for the temperature dependence of average effective interdiffusion coefficients. Al exhibits the negative interdiffusion coefficient at all temperature which represents the strong negative values of off-diagonal interdiffusion

coefficients i.e. strong thermodynamic interaction of Al with other elements. In general, Co is the fastest, and Fe is the slowest diffusing element in the $\text{Al}_{0.25}\text{CoCrFeNi}$ alloy.

6.1.5 $\text{Al}_{48}\text{Ni}_{52}$ vs. $\text{Co}_{25}\text{Cr}_{25}\text{Fe}_{25}\text{Ni}_{25}$ quinary diffusion couples

Figure 13 shows the concentration profiles superimposed on the BSE micrograph of $\text{Al}_{48}\text{Ni}_{52}$ vs. $\text{Co}_{25}\text{Cr}_{25}\text{Fe}_{25}\text{Ni}_{25}$ diffusion couples isothermally annealed at 900° , 1000° , 1100° , and 1200°C for 240, 120, 48, and 24 hours, respectively. Aforementioned, FCC side of the diffusion couple did not develop BCC or duplex phase suggesting that diffusion is significantly faster in FCC phase.

Table 14 reports the average effective interdiffusion coefficients, activation energies, and pre-exponential factor of Al, Co, Cr, Fe, and Ni, in BCC Al-Co-Cr-Fe-Ni alloy formed in the $\text{Al}_{48}\text{Ni}_{52}$ end member and FCC Al-Co-Cr-Fe-Ni alloy formed in the $\text{Co}_{25}\text{Cr}_{25}\text{Fe}_{25}\text{Ni}_{25}$ end member, after interdiffusion in $\text{Al}_{48}\text{Ni}_{52}$ vs. $\text{Co}_{25}\text{Cr}_{25}\text{Fe}_{25}\text{Ni}_{25}$ diffusion couples. Figure 33 and Figure 34 shows the corresponding Arrhenius plot for the temperature dependence of average effective interdiffusion coefficients in FCC Al-Co-Cr-Fe-Ni and BCC Al-Co-Cr-Fe-Ni, respectively. Ni and Cr exhibits the negative interdiffusion coefficient in FCC Al-Co-Cr-Fe-Ni alloy which represents the strong negative values of off-diagonal interdiffusion coefficients i.e. strong thermodynamic interaction with other elements. All elements have similar order of magnitude for interdiffusion coefficients in FCC and BCC Al-Co-Cr-Fe-Ni alloys. In general, Al has the highest diffusivity in both FCC and BCC phases at 1100°C and above temperatures.

Table 14. Average effective interdiffusion coefficients, activation energy and pre-exponential factor of Al, Co, Cr, Fe and Ni in BCC Al₄₈Ni₅₂ and FCC Co₂₅Cr₂₅Fe₂₅Ni₂₅ end member alloy measured using Al₄₈Ni₅₂ vs Co₂₅Cr₂₅Fe₂₅Ni₂₅ diffusion couples.

End member Alloy Diffusion couple	Temperature (°C)	\bar{D}_{Al}^{eff} (m ² /s)	\bar{D}_{Cr}^{eff} (m ² /s)	\bar{D}_{Fe}^{eff} (m ² /s)	\bar{D}_{Co}^{eff} (m ² /s)	\bar{D}_{Ni}^{eff} (m ² /s)
Al ₄₈ Ni ₅₂	900	$1.93 (0.10) \times 10^{-16}$	$7.79 (1.70) \times 10^{-17}$	$1.20 (0.19) \times 10^{-16}$	$1.53 (0.06) \times 10^{-16}$	$-1.97 (0.81) \times 10^{-17}$
	1000	$1.88 (0.14) \times 10^{-15}$	$1.10 (0.24) \times 10^{-15}$	$1.34 (0.13) \times 10^{-15}$	$1.33 (0.16) \times 10^{-15}$	$5.01 (2.02) \times 10^{-16}$
	1100	$3.96 (0.03) \times 10^{-14}$	$2.49 (0.06) \times 10^{-14}$	$3.19 (0.09) \times 10^{-14}$	$3.34 (0.04) \times 10^{-14}$	$8.87 (1.38) \times 10^{-15}$
	1200	$1.84 (0.03) \times 10^{-13}$	$1.24 (0.03) \times 10^{-13}$	$1.45 (0.04) \times 10^{-13}$	$1.63 (0.09) \times 10^{-13}$	$6.99 (1.34) \times 10^{-14}$
	Q (kJ/mol)	339.71	363.49	352.10	346.61	-
	D₀ (m²/s)	0.2326	1.1475	0.5233	0.3515	-
Co ₂₅ Cr ₂₅ Fe ₂₅ Ni ₂₅	900	$7.33 (1.06) \times 10^{-17}$	$4.36 (3.03) \times 10^{-17}$	$3.02 (1.70) \times 10^{-16}$	$9.87 (2.83) \times 10^{-17}$	$2.99 (2.17) \times 10^{-16}$
	1000	$9.31 (1.77) \times 10^{-16}$	$3.96 (1.19) \times 10^{-16}$	$1.44 (1.48) \times 10^{-15}$	$9.06 (0.60) \times 10^{-16}$	$-2.20 (0.58) \times 10^{-15}$
	1100	$2.13 (0.02) \times 10^{-14}$	$-2.67 (1.09) \times 10^{-14}$	$1.06 (0.78) \times 10^{-14}$	$1.46 (0.18) \times 10^{-14}$	$-1.25 (0.24) \times 10^{-14}$
	1200	$1.01 (0.02) \times 10^{-13}$	$-5.22 (1.62) \times 10^{-14}$	$3.53 (0.58) \times 10^{-14}$	$6.94 (1.00) \times 10^{-14}$	$-5.95 (2.15) \times 10^{-14}$
	Q (kJ/mol)	357.42	-	233.71	322.67	-
	D₀ (m²/s)	0.5707	-	7.0×10^{-6}	0.0209	-

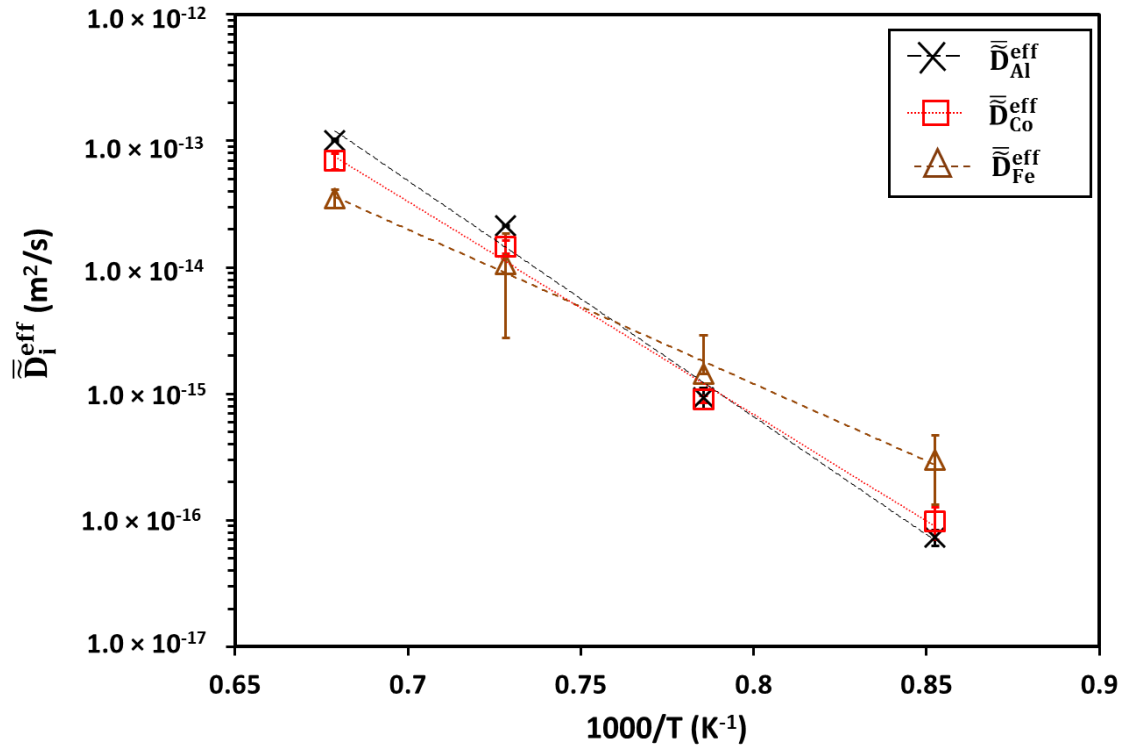


Figure 33. Temperature dependence of average effective interdiffusion coefficients for Co, Cr, Fe and Ni in FCC $Co_{25}Cr_{25}Fe_{25}Ni_{25}$ end member alloy measured using $Al_{48}Ni_{52}$ vs. $Co_{25}Cr_{25}Fe_{25}Ni_{25}$ diffusion couples in temperature range from 900 to 1200°C.

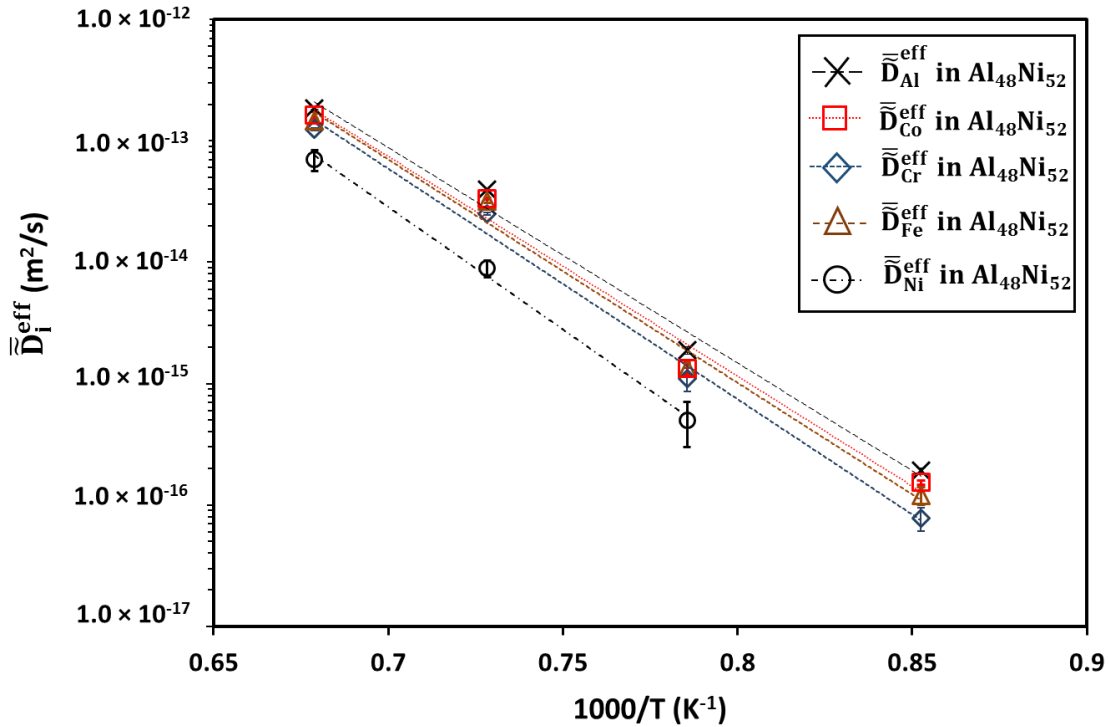


Figure 34. Temperature dependence of average effective interdiffusion coefficients for Al, Co, Cr, Fe and Ni in BCC Al₄₈Ni₅₂ end member measured using Al₄₈Ni₅₂ vs. Co₂₅Cr₂₅Fe₂₅Ni₂₅ diffusion couples in temperature range from 900° to 1200°C

6.1.6 Al₄₈Ni₅₂ vs. Co₂₀Cr₂₀Fe₂₀Ni₂₀Mn₂₀ senary diffusion couples

Figure 18 shows the concentration profiles superimposed on the BSE micrograph of Al₄₈Ni₅₂ vs. Co₂₀Cr₂₀Fe₂₀Ni₂₀Mn₂₀ diffusion couples isothermally annealed at 900°, 1000°, 1100°, and 1200°C for 240, 120, 48, and 24 hours, respectively. Aforementioned, FCC side of the diffusion couple did not develop BCC or duplex phase suggesting that diffusion is significantly faster in FCC phase, similar to Al₄₈Ni₅₂ vs. Co₂₅Cr₂₅Fe₂₅Ni₂₅ diffusion couples.

Table 15 reports the average effective interdiffusion coefficients, activation energies, and pre-exponential factor of Al, Co, Cr, Fe, Ni, and Mn in BCC Al-Co-Cr-Fe-Ni-Mn alloy formed in

the $\text{Al}_{48}\text{Ni}_{52}$ end member and FCC Al-Co-Cr-Fe-Ni-Mn alloy formed in the $\text{Co}_{20}\text{Cr}_{20}\text{Fe}_{20}\text{Ni}_{20}\text{Mn}_{20}$ end member, after interdiffusion in $\text{Al}_{48}\text{Ni}_{52}$ vs. $\text{Co}_{20}\text{Cr}_{20}\text{Fe}_{20}\text{Ni}_{20}\text{Mn}_{20}$ diffusion couples. Figure 35 and Figure 36 shows the corresponding Arrhenius plot for the temperature dependence of average effective interdiffusion coefficients in FCC Al-Co-Cr-Fe-Ni-Mn alloy and BCC Al-Co-Cr-Fe-Ni-Mn alloy, respectively. In general, Al has the highest diffusivity in both FCC and BCC phases at 1100°C and above temperatures. Unlike in $\text{Fe}_{50}\text{Cr}_{50}$ vs. $\text{Co}_{50}\text{Ni}_{50}$ diffusion couples wherein interdiffusion coefficients of Co, Cr, Fe and Ni were 1-2 order of magnitude higher in BCC phase, in comparison to FCC phase, in $\text{Al}_{48}\text{Ni}_{52}$ vs. $\text{Co}_{20}\text{Cr}_{20}\text{Fe}_{20}\text{Ni}_{20}\text{Mn}_{20}$ interdiffusion elements (i.e. Al, Co, Cr, Fe, Ni and Mn) has similar order of magnitude of interdiffusion coefficients in FCC and BCC Al-Co-Cr-Fe-Ni-Mn alloy, similar to $\text{Al}_{48}\text{Ni}_{52}$ vs. $\text{Co}_{25}\text{Cr}_{25}\text{Fe}_{25}\text{Ni}_{25}$ diffusion couples.

Table 15. Average effective interdiffusion coefficients, activation energy and pre-exponential factor of Al, Co, Cr, Fe, Ni, and Mn in BCC Al₄₈Ni₅₂ and FCC Co₂₀Cr₂₀Fe₂₀Ni₂₀Mn₂₀ end member alloy measured using Al₄₈Ni₅₂ vs Co₂₀Cr₂₀Fe₂₀Ni₂₀Mn₂₀ diffusion couples.

End member Alloy Diffusion couple	Temperature (°C)	\bar{D}_{Al}^{eff} (m ² /s)	\bar{D}_{Cr}^{eff} (m ² /s)	\bar{D}_{Fe}^{eff} (m ² /s)	\bar{D}_{Co}^{eff} (m ² /s)	\bar{D}_{Ni}^{eff} (m ² /s)	\bar{D}_{Mn}^{eff} (m ² /s)
Al ₄₈ Ni ₅₂	900	$3.66 (0.98) \times 10^{-17}$	$3.50 (0.99) \times 10^{-17}$	$4.22 (1.30) \times 10^{-17}$	$3.23 (0.92) \times 10^{-17}$	$3.34 (1.18) \times 10^{-17}$	$3.51 (1.04) \times 10^{-17}$
	1000	$5.30 (0.25) \times 10^{-16}$	$4.42 (0.60) \times 10^{-16}$	$5.85 (0.23) \times 10^{-16}$	$4.95 (0.43) \times 10^{-16}$	$4.91 (0.31) \times 10^{-16}$	$4.90 (0.25) \times 10^{-16}$
	1100	$2.93 (0.02) \times 10^{-14}$	$2.24 (0.18) \times 10^{-14}$	$2.82 (0.12) \times 10^{-14}$	$2.74 (0.13) \times 10^{-14}$	$2.65 (0.09) \times 10^{-14}$	$3.05 (0.02) \times 10^{-14}$
	1200	$1.83 (0.0) \times 10^{-13}$	$1.46 (0.08) \times 10^{-13}$	$1.65 (0.07) \times 10^{-13}$	$1.82 (0.01) \times 10^{-13}$	$1.75 (0.04) \times 10^{-13}$	$2.05 (0.03) \times 10^{-13}$
	Q (kJ/mol)	425.34	415.45	412.37	430.00	426.42	432.99
	D₀ (m²/s)	263.07	88.86	82.45	377.58	269.29	534.40
Co ₂₀ Cr ₂₀ Fe ₂₀ Ni ₂₀ Mn ₂₀	900	$2.48 (0.70) \times 10^{-16}$	$5.94 (2.06) \times 10^{-17}$	$5.43 (2.17) \times 10^{-17}$	$7.64 (1.21) \times 10^{-17}$	$4.20 (1.85) \times 10^{-17}$	$1.40 (0.23) \times 10^{-16}$
	1000	$2.10 (0.94) \times 10^{-15}$	$1.63 (0.28) \times 10^{-15}$	$5.90 (2.23) \times 10^{-16}$	$4.16 (1.92) \times 10^{-16}$	$3.60 (0.89) \times 10^{-16}$	$1.78 (0.59) \times 10^{-15}$
	1100	$4.08 (0.16) \times 10^{-14}$	$2.38 (0.74) \times 10^{-14}$	$3.36 (1.18) \times 10^{-15}$	$9.06 (0.79) \times 10^{-15}$	$4.27 (2.20) \times 10^{-15}$	$3.40 (0.28) \times 10^{-14}$
	1200	$1.73 (0.13) \times 10^{-13}$	$1.90 (0.80) \times 10^{-13}$	$4.46 (1.90) \times 10^{-14}$	$4.17 (0.87) \times 10^{-14}$	$3.06 (1.10) \times 10^{-14}$	$1.90 (0.16) \times 10^{-13}$
	Q (kJ/mol)	325.08	387.68	312.77	315.02	318.84	353.68
	D₀ (m²/s)	0.0658	11.948	0.0041	0.0063	0.0057	0.7387

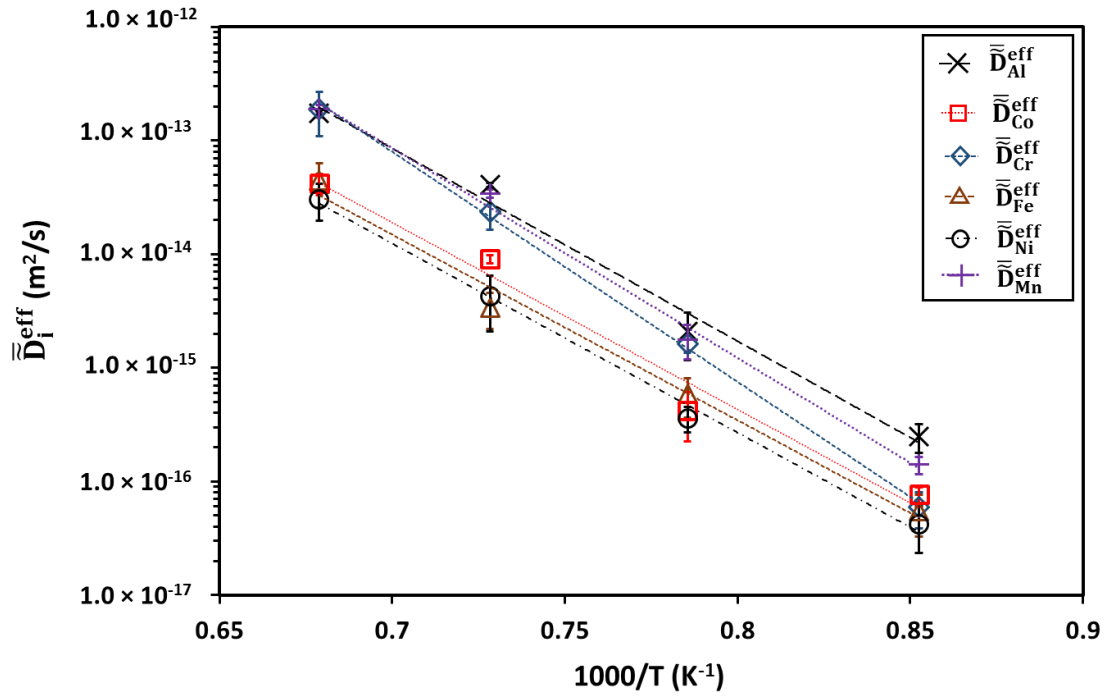


Figure 35. Temperature dependence of average effective interdiffusion coefficients for Al, Co, Cr, Fe, Ni, and Mn in FCC $\text{Co}_{20}\text{Cr}_{20}\text{Fe}_{20}\text{Ni}_{20}\text{Mn}_{20}$ end member alloy measured using $\text{Al}_{48}\text{Ni}_{52}$ vs. $\text{Co}_{20}\text{Cr}_{20}\text{Fe}_{20}\text{Ni}_{20}\text{Mn}_{20}$ diffusion couples in temperature range from 900° to 1200°C .

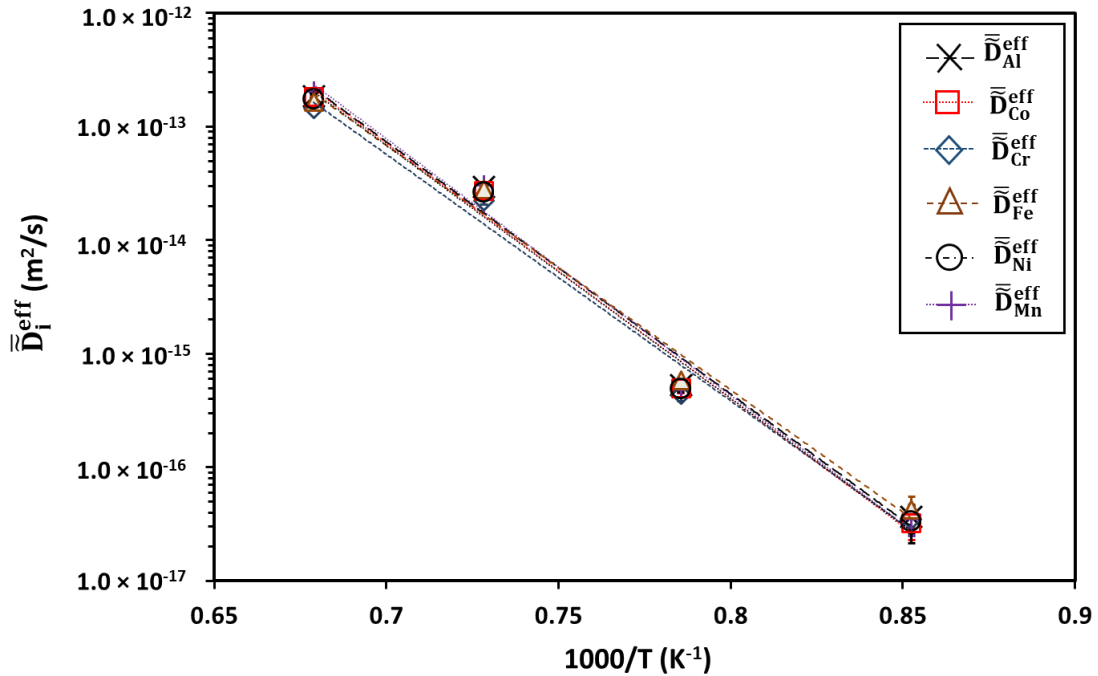


Figure 36. Temperature dependence of average effective interdiffusion coefficients for Al, Co, Cr, Fe, Ni, and Mn in BCC Al₄₈Ni₅₂ end member alloy measured using Al₄₈Ni₅₂ vs. Co₂₀Cr₂₀Fe₂₀Ni₂₀Mn₂₀ diffusion couples in temperature range from 900 to 1200°C.

6.2 Comparison of interdiffusion coefficients

Figure 37 compares the average effective interdiffusion coefficients for all elements in FCC alloys determined in present study. Diffusion of Co is the fastest in quinary off-equiatomic AlCoCrFeNi or near-equiatomic CoCrFeNiMn alloy and slowest in CoCrFeNi alloy. Diffusion of Cr is the fastest in senary off-equiatmic AlCoCrFeNiMn alloy and slowest in quaternary near-equiatomic CoCrFeNi alloy. Diffusion of Fe is fastest in off-equiatomic quinary AlCoCrFeNi alloy

and slowest in near-equiatomic CoCrFeNi. Diffusion of Ni is fastest in near equiatomic CoCrFeNiMn and slowest in near-equiatomic CoCrFeNi alloy. Diffusion of Al is faster in off-equiatomic senary AlCoCrFeNiMn alloy than off-equiatomic quinary AlCoCrFeNiMn alloy. Diffusion of Mn is slightly faster in off-equiatomic senary AlCoCrFeNiMn alloy than equiatomic CoCrFeNiMn alloy. Therefore, a reduction in the magnitude of interdiffusion coefficients was not observed for all individual components in higher component FCC alloy system in comparison to lower component FCC alloy system.

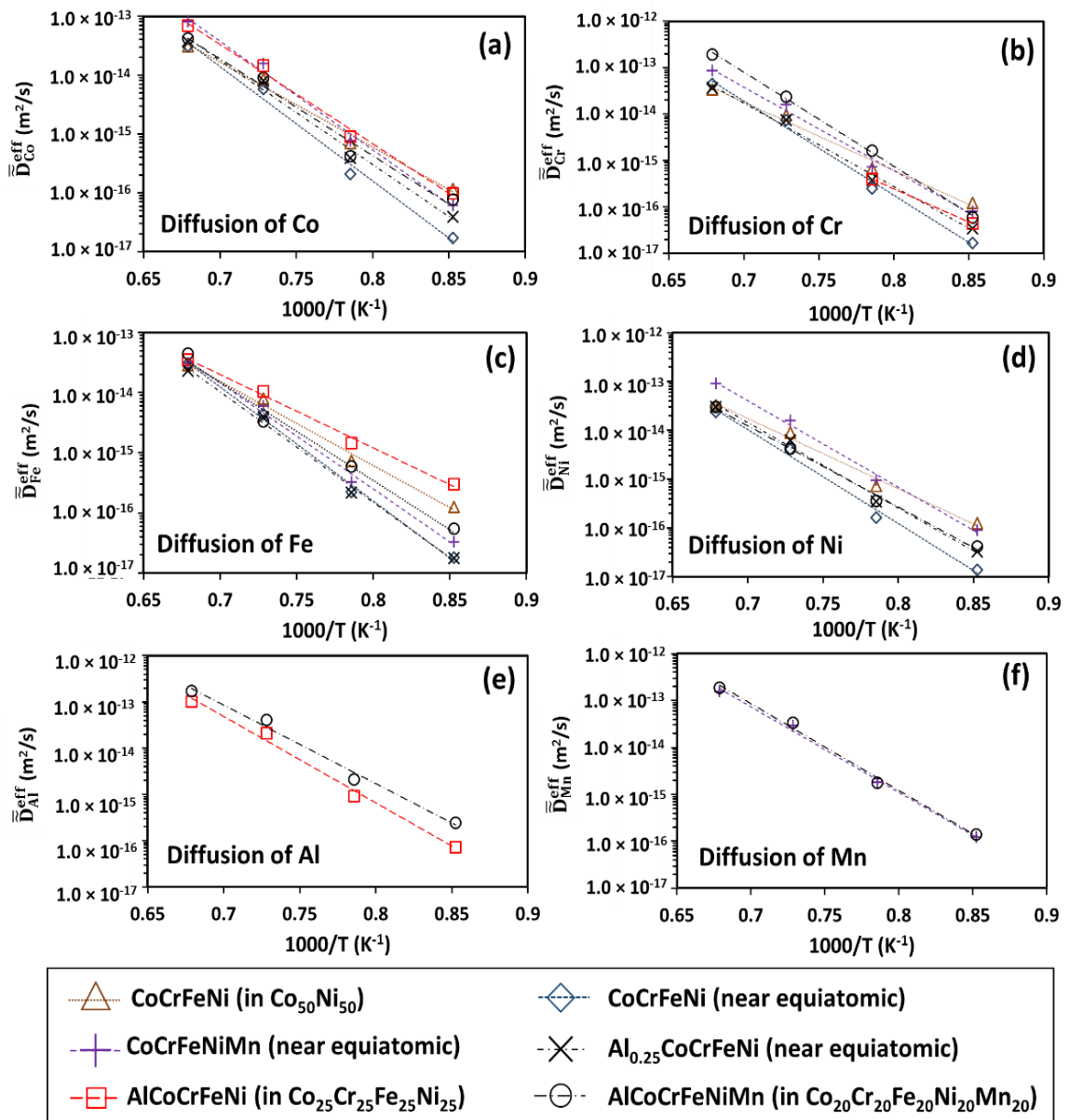


Figure 37. Comparison of average effective interdiffusion coefficients of (a) Co, (b) Cr, (c) Fe, (d) Ni, (e) Al, and (f) Mn in various FCC alloys

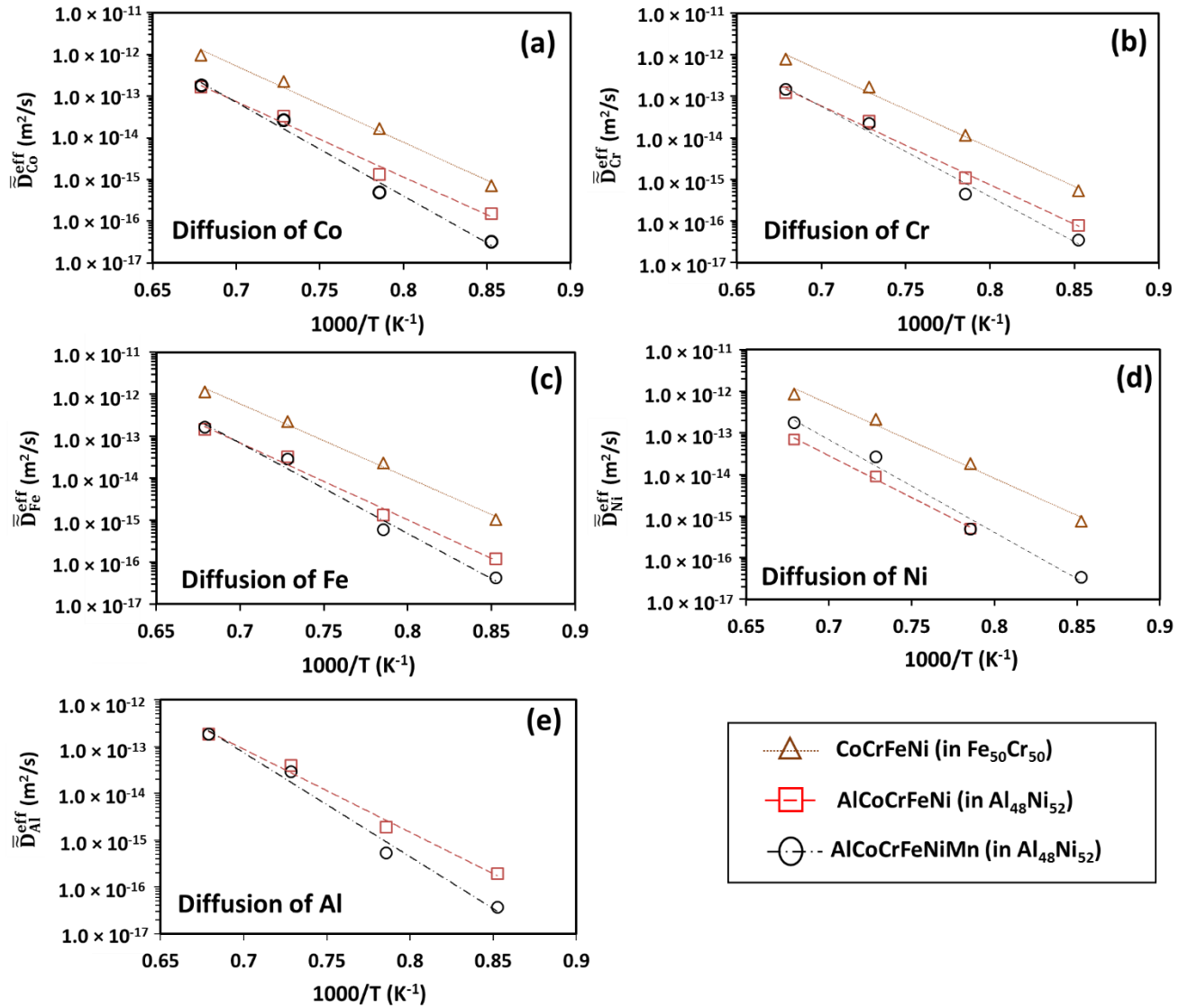


Figure 38. Comparison of average effective interdiffusion coefficients of (a) Co, (b) Cr, (c) Fe, (d) Ni, and (e) Al in various BCC alloys

Figure 38 compares the average effective interdiffusion coefficients for all elements in BCC alloys determined in present study. Diffusion of Co, Cr, Fe and Ni is approximately an order of

magnitude higher in off-equiatomic quaternary CoCrFeNi alloy than in off equiatomic quinary AlCoCrFeNi and off equiatomic senary AlCoCrFeNiMn alloy. Diffusion of Co, Cr and Fe is the slowest in off equiatomic senary AlCoCrFeNiMn alloy. Diffusion of Al is higher in off-equiatomic quinary AlCoCrFeNi than off-equiatomic senary AlCoCrFeNiMn alloy. This is in compliance with sluggish diffusion effect. However, diffusion of Ni is slowest in off-equiatomic quinary AlCoCrFeNi alloy. Therefore, sluggish diffusion effect is largely obeyed by diffusion of elements in BCC alloys.

Table 16 compares the average effective interdiffusion coefficients of Fe, Cr and Ni determined from concentration profiles reported by Duh and Dayananda [84], on either side of the Matano plane with the average effective interdiffusion coefficients measured in quaternary CoCrFeNi alloys and quinary CoCrFeNiMn and Al_{0.25}CoCrFeNi alloys. Diffusion coefficient of Cr is higher in quaternary CoCrFeNi alloys and quinary CoCrFeNiMn and Al_{0.25}CoCrFeNi alloys in comparison to ternary FeCrNi alloy. Diffusion coefficient of Fe is higher in quinary CoCrFeNiMn alloy than ternary FeCrNi alloy. Thus far, a notable reduction in interdiffusion coefficients of Fe, Cr or Ni was not observed with addition of Co, Mn, or Ni in FeCrNi alloy.

Table 16. Comparison of average effective interdiffusion coefficients of Fe, Cr, and Ni at 1100°C in FeCrNi alloy with average effective interdiffusion coefficients of Cr, Fe, Co, and Ni in CoCrFeNi, CoCrFeNiMn and Al_{0.25}CoCrFeNi alloys.

Element <i>i</i>	CrFeNi		CoCrFeNi	CoCrFeNiMn	Al _{0.25} CoCrFeNi
	Cr _{32.1} Fe _{15.8} Ni _{52.1} to Cr _{16.1} Fe _{33.5} Ni _{50.4}	Cr _{16.1} Fe _{33.5} Ni _{50.4} to Cr ₀ Fe ₅₂ Ni ₄₈	Co ₂₀ Cr ₂₇ Fe ₃₃ Ni ₂₀ to Co ₃₀ Cr ₂₀ Fe ₂₀ Ni ₃₀	Co ₂₅ Cr ₂₅ Ni ₂₅ Fe ₁₅ Mn ₁₀ to Co ₁₅ Cr ₁₅ Ni ₁₅ Fe ₂₅ Mn ₃₀	Al ₆ Co ₁₉ Cr ₂₈ Fe ₂₈ Ni ₁₉ to Al ₆ Co ₂₈ Cr ₁₉ Fe ₁₉ Ni ₂₈
	$\bar{D}_{i,L}^{eff}$ (m ² /s)	$\bar{D}_{i,R}^{eff}$ (m ² /s)	\bar{D}_i^{eff} (m ² /s)	\bar{D}_i^{eff} (m ² /s)	\bar{D}_i^{eff} (m ² /s)
Cr	6.50 x 10 ⁻¹⁵	6.18 x 10 ⁻¹⁵	7.45 (0.69) × 10 ⁻¹⁵	1.60 (0.08) × 10 ⁻¹⁴	7.38 (0.91) × 10 ⁻¹⁵
Fe	5.35 x 10 ⁻¹⁵	5.47 x 10 ⁻¹⁵	4.37 (0.27) × 10 ⁻¹⁵	6.04 (2.01) × 10 ⁻¹⁵	3.95 (0.50) × 10 ⁻¹⁵
Co	–	–	5.88 (0.15) × 10 ⁻¹⁵	1.58 (0.54) × 10 ⁻¹⁴	8.09 (0.99) × 10 ⁻¹⁵
Ni	2.20 x 10 ⁻¹⁶ (Uphill diffusion)	1.72 x 10 ⁻¹⁵	4.09 (0.33) × 10 ⁻¹⁵	1.60 (0.46) × 10 ⁻¹⁴	6.33 (0.79) × 10 ⁻¹⁵

6.3 Measurement of Tracer diffusion coefficient

6.3.1 Tracer diffusion coefficient of Ni in quaternary CoCrFeNi alloy

Tracer diffusion coefficients of Ni (D_{Ni}^*) in near equiatomic quaternary CoCrFeNi alloy was measured using “sandwich” thin film diffusion couple, in the temperature range from 900° to 1000°C using Belova *et al.* [46] approach and Gaussian distribution function, as described in section 2.3.2. Figure 39 shows the Spike profile of Ni superimposed on the interdiffusion profile, and Gaussian fitted difference of Spike and interdiffusion profile. Table 17 compares the measured tracer diffusion coefficient of Ni in present study with the independent measurement performed by Vaidya *et al.* [25] using ⁶³Ni₂₈ radiotracers.

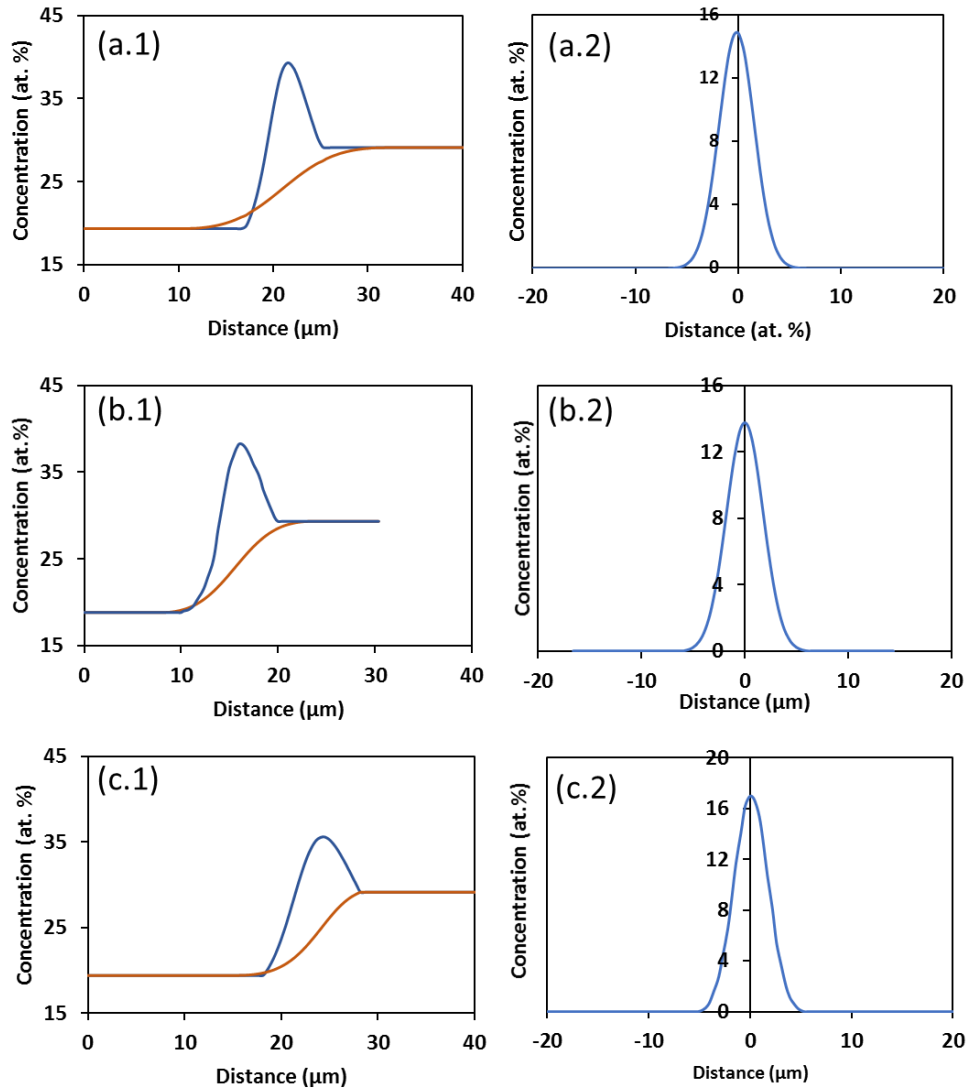


Figure 39. Concentration profiles in CoCrFeNi system. (a.1) Spike profile at 900°C superimposed on the interdiffusion profile of Ni, (a.2) corresponding Gaussian fitted subtracted profile in (a.1). (b.1) Spike profile at 950°C superimposed on the interdiffusion profile of Ni, (b.2) corresponding Gaussian fitted subtracted profile in (b.1). (c.1) Spike profile at 1000°C superimposed on the interdiffusion profile of Ni, (c.2) corresponding Gaussian fitted subtracted profile in (c.1)

Table 17. Tracer diffusion coefficient of Ni in CoCrFeNi alloy.

T (°C)	1000/T (K ⁻¹)	Present study			Vaidya et al.		
		D (m ² /s)	D _o (m ² /s)	Q (kJ/mol)	D (m ² /s)	D _o (m ² /s)	Q (kJ/mol)
900	0.853	1.43 × 10 ⁻¹⁷	9.6 × 10 ⁻⁸	220.8	6.62 × 10 ⁻¹⁸	2.0 × 10 ⁻⁶	257.8
950	0.818	3.51 × 10 ⁻¹⁷			1.95 × 10 ⁻¹⁷		
1000	0.786	8.46 × 10 ⁻¹⁷			5.28 × 10 ⁻¹⁷		

6.3.2 Tracer diffusion coefficient of Ni in quinary CoCrFeNiMn alloy

Tracer diffusion coefficients of Ni (D_{Ni}^*) in near equiatomic quaternary CoCrFeNiMn alloy was measured using “sandwich” thin film diffusion couple. Figure 40 shows the Spike profile of Ni superimposed on the interdiffusion profile, and Gaussian fitted difference of Spike and interdiffusion profile at all temperatures. Table 18 compares the measured tracer diffusion coefficient of Ni in present study with the independent measurement performed by Vaidya *et al.* [25] using ⁶³Ni₂₈ radiotracers.

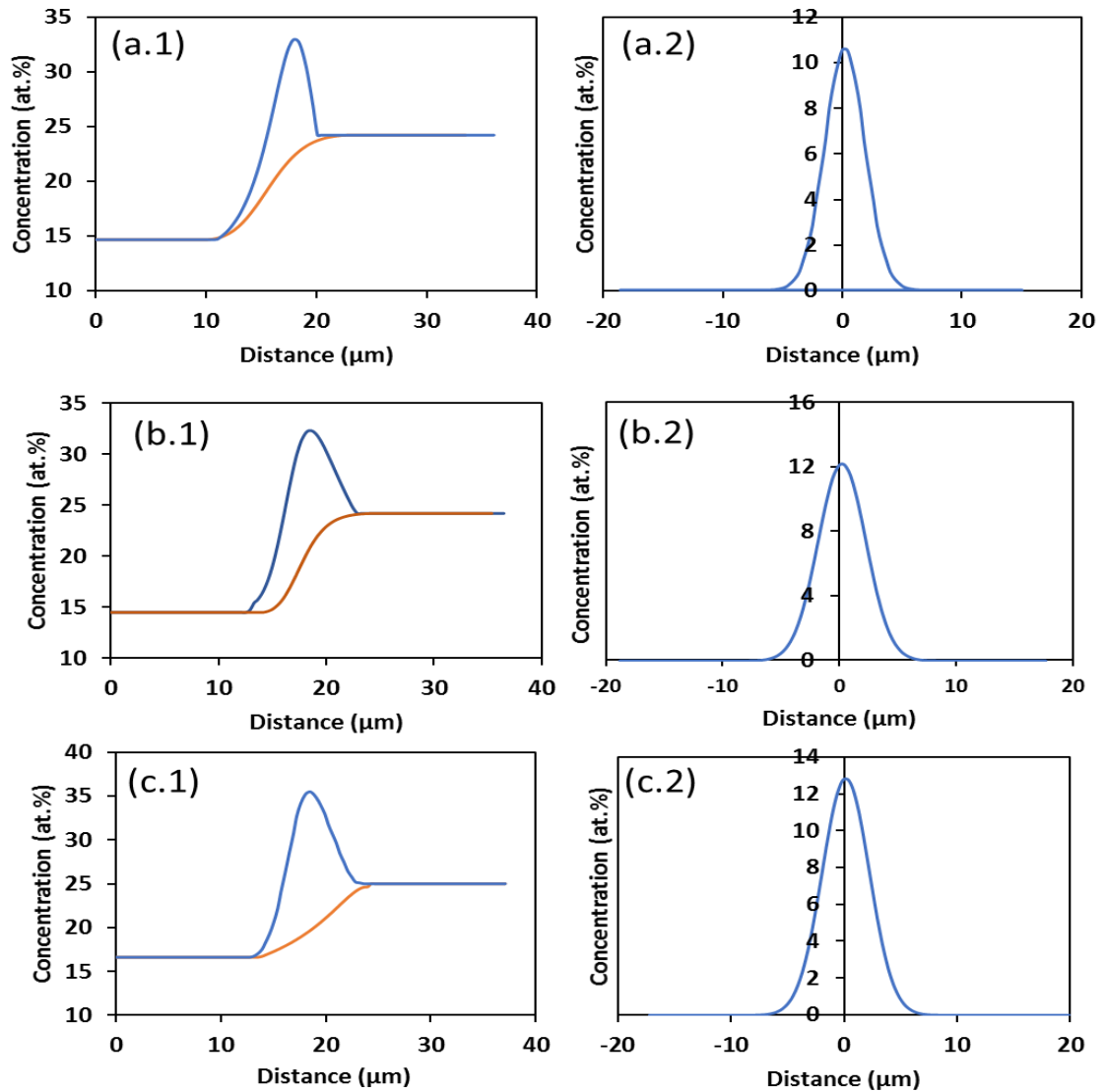


Figure 40. Concentration profiles in CoCrFeNiMn system. (a.1) Spike profile at 900°C superimposed on the interdiffusion profile of Ni, (a.2) corresponding Gaussian fitted subtracted profile in (a.1). (b.1) Spike profile at 950°C superimposed on the interdiffusion profile of Ni, (b.2) corresponding Gaussian fitted subtracted profile in (b.1). (c.1) Spike profile at 1000°C superimposed on the interdiffusion profile of Ni, (c.2) corresponding Gaussian fitted subtracted profile in (c.1)

Table 18. Tracer diffusion coefficient of Ni in CoCrFeNiMn alloy.

T (°C)	1000/T (K ⁻¹)	Present study			Vaidya et al.		
		D (m ² /s)	D ₀ (m ² /s)	Q (kJ/mol)	D (m ² /s)	D ₀ (m ² /s)	Q (kJ/mol)
900	0.853	2.86 × 10 ⁻¹⁷	2.83 × 10 ⁻⁴	292.0	1.80 × 10 ⁻¹⁷	6.2 × 10 ⁻⁴	303.9
950	0.818	9.22 × 10 ⁻¹⁷			6.45 × 10 ⁻¹⁷		
1000	0.786	3.01 × 10 ⁻¹⁷			2.08 × 10 ⁻¹⁷		

6.3.3 Tracer diffusion coefficient of Ni in quinary Al_{0.25}CoCrFeNi alloy

Tracer diffusion coefficients of Ni (D_{Ni}^*) in near equiatomic quaternary Al_{0.25}CoCrFeNi alloy was measured using “sandwich” thin film diffusion couple. Figure 41 shows the Spike profile of Ni superimposed on the interdiffusion profile, and Gaussian fitted difference of Spike and interdiffusion profile at all temperatures. Tracer diffusion coefficient of Ni determined in present study is outlined in Table 19.

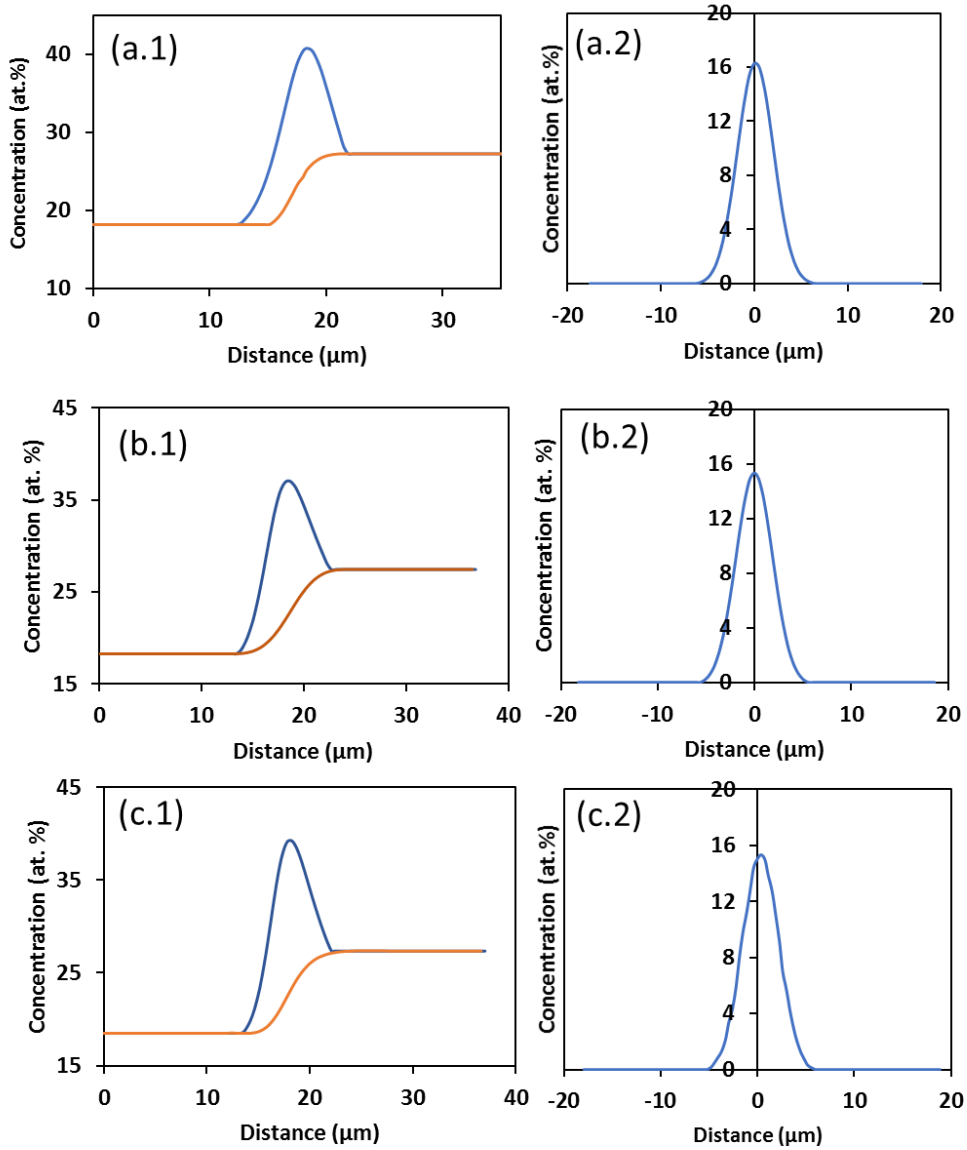


Figure 41. Concentration profiles in $\text{Al}_{0.25}\text{CoCrFeNi}$ system. (a.1) Spike profile at 900°C superimposed on the interdiffusion profile of Ni, (a.2) corresponding Gaussian fitted subtracted profile in (a.1). (b.1) Spike profile at 950°C superimposed on the interdiffusion profile of Ni, (b.2) corresponding Gaussian fitted subtracted profile in (b.1). (c.1) Spike profile at 1000°C superimposed on the interdiffusion profile of Ni, (c.2) corresponding Gaussian fitted subtracted profile in (c.1)

Table 19. Tracer diffusion coefficient of Ni in Al_{0.25}CoCrFeNi

T (°C)	1000/T (K ⁻¹)	Present study		
		D (m ² /s)	D ₀ (m ² /s)	Q (kJ/mol)
900	0.853	3.72 × 10 ⁻¹⁷	3.4 × 10 ⁻⁸	201.7
950	0.818	7.36 × 10 ⁻¹⁷		
1000	0.786	1.90 × 10 ⁻¹⁶		

6.4 Comparison of Tracer diffusion coefficient of Ni in various FCC alloys

Figure 42 compares the tracer diffusion coefficient of Ni in quaternary CoCrFeNi, quinary CoCrFeNiMn and Al_{0.25}CoCrFeNi alloys for near equiatomic composition, measured in present study. Comparison suggests that tracer diffusion coefficient of Ni is lower in quaternary CoCrFeNi in comparison to tracer diffusion coefficient of Ni in CoCrFeNiMn or Al_{0.25}CoCrFeNi alloys. Figure 43 compares the tracer diffusion coefficient of Ni in FCC alloys i.e. pure Ni (Self diffusion) [85], Fe-45.3Ni [86], Fe-15Cr-20Ni [87], CoCrFeNiMn_{0.5} [21], CoCrFeNi and CoCrFeNiMn [25]. Comparison of tracer diffusion coefficient of Ni in Figure 43, clearly shows that increasing number of component in an alloys system can not be correlated with the sluggish diffusion kinetics, otherwise, Ni self diffusion should be the fastest and diffusion of Ni in CoCrFeNiMn/Al_{0.25}CoCrFeNi should be the slowest. Contrary to sluggish diffusion effect, tracer diffusion of Ni is the fastest quinary CoCrFeNiMn/Al_{0.25}CoCrFeNi alloys.

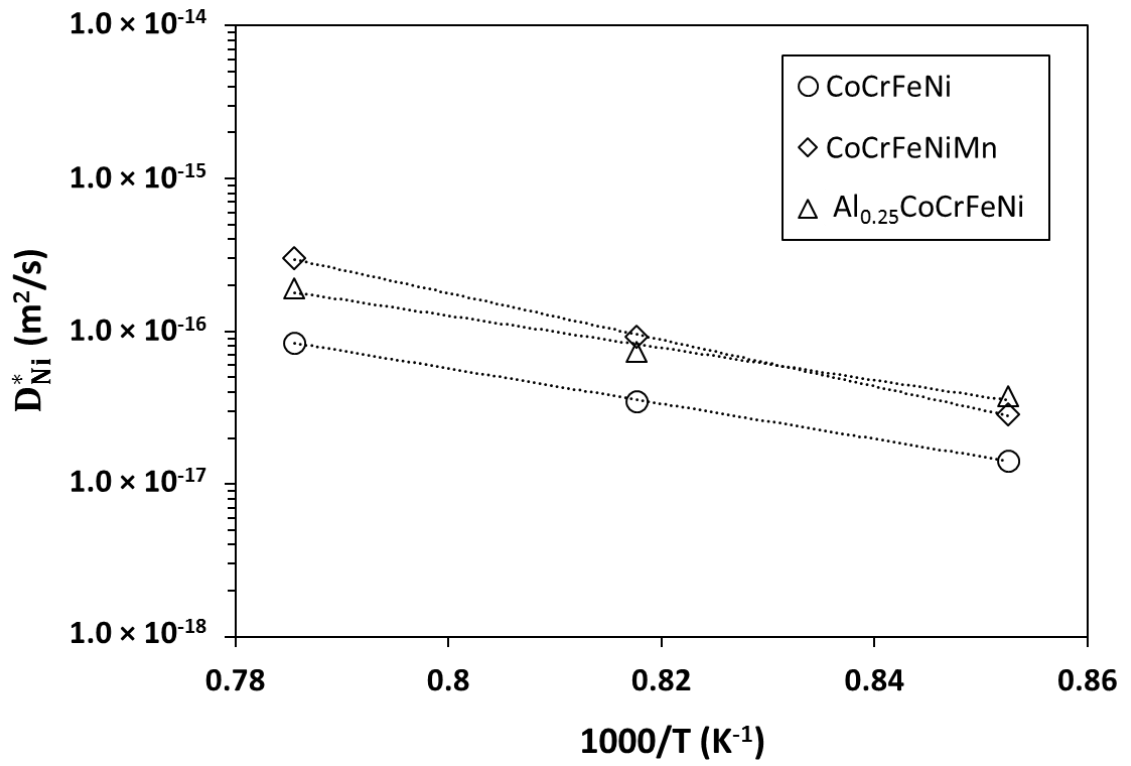


Figure 42. Comparison of tracer diffusion coefficient of Ni in CoCrFeNi, CoCrFeNiMn and Al_{0.25}CoCrFeNi alloys measured in present study

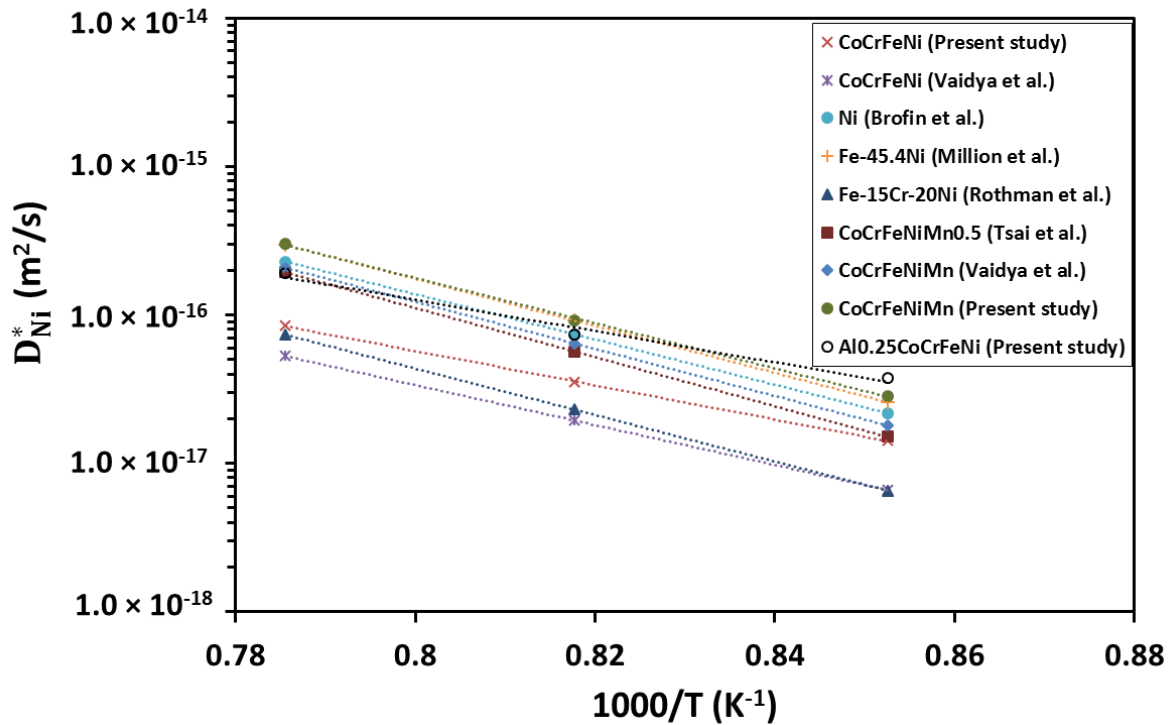


Figure 43. Comparison of tracer diffusion coefficient of Ni in various FCC alloys as a function of temperature.

6.5 Potential Energy Fluctuation and Excess Entropy

It has been postulated that HEAs may exhibit larger fluctuations in potential energy of lattice sites in comparison solvent based conventional alloys (i.e. low entropy alloys), which may result in anomalously slow diffusion in HEAs [21]. It has also been suggested that in solvent based conventional alloys or pure metals, potential energy of each lattice site is approximately equal, however, HEAs exhibit larger variation in potential energy of lattice sites due to which atoms are

relatively more stable in some sites, which tends to form atomic traps (low lattice potential energy sites). These highly stable atomic sites (i.e. atomic traps), results in slowing the rate of diffusion [21].

Figure 44 shows the fluctuation in potential energy (p) as a function of excess entropy (S_E/R), based on Equation 23. Excess entropy decreases with an increase in fluctuation in potential energy. As per Equation 24, correlated entropy would decrease with an increase in excess entropy. Therefore, a larger fluctuation in potential energy (p), which give rise to deeper potential energy traps to impede diffusion, would lower the correlated configurational entropy. Alternatively, overall lower correlated configurational entropy should result in sluggish diffusion, which contradicts the original postulation that HEAs should exhibit the sluggish diffusion.

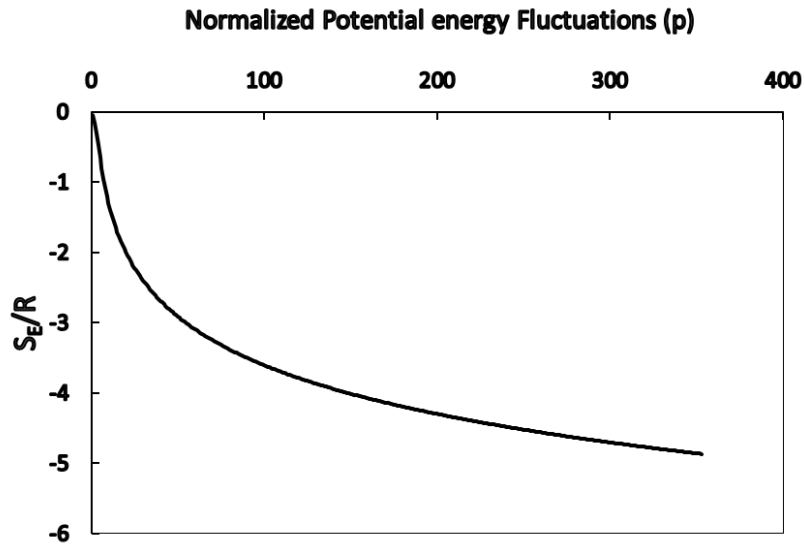


Figure 44. Excess entropy as a function of normalized potential energy fluctuations.

Excess entropy and correlated entropy of the Al, Co, Cr, Fe, Ni, Mn based binary, ternary, quaternary and quinary alloys were calculated using Equation 23 and Equation 25, respectively. Table 20 reports the atomic radius and bulk modulus of the various elements used for calculating normalized energy fluctuation due to intrinsic residual strain (p_e), given by Equation 26. Binary enthalpy of mixing of element i and j (ΔH_{ij}^{mix}) is estimated by the Miedema's macroscopic model for liquid binary alloy [51]. In addition to Table 7, Table 21 also reports the binary enthalpy of mixing of other binary-pairs relevant to the present study for the determination of normalized energy fluctuation due to chemical bond misfit (p_c), given by Equation 27. Based on regular solution model, enthalpy of mixing of solid solution in multi-component system (e.g., HEA) can be determined by [54, 88, 89] Equation 30.

Table 22 reports the calculated correlated and excess entropy at 1000°C for all possible alloys of equiatomic binary derivatives of Co-Cr-Fe-Ni-Mn system, i.e. CrFeNi, CoCrFeNi, CoCrFeNiMn and few other amorphous alloys (CuHfNiTiZr, CuHfCoTiZr, CuBeNiTiZr, Vitreloy 4 (V4)).

Table 20. Atomic radius and bulk modulus of various elements

Element	Atomic Radius (Å)	Bulk Modulus (GPa)
Al	1.4317	76
Co	1.2510	180
Cr	1.2491	160
Fe	1.2412	170
Ni	1.2459	180
Mn	1.3500	120
Cu	1.2780	140
Ti	1.4615	110
Hf	1.5775	110
Zr	1.6025	91
Be	1.1280	130

Table 21. Binary enthalpy of mixing calculated by Miedema's model for atomic pair between element i and j [52].

Binary Pairs ($i-j$)	Cu-Hf	Cu-Ni	Cu-Ti	Cu-Zr	Hf-Ni	Hf-Ti	Hf-Zr	Ni-Ti	Ni-Zr	Ti-Zr
$\Delta H_{ij}^{\text{mix}}$ (kJ/mol)	-17	4	-9	-23	-42	0	0	-35	-49	0
Binary Pairs ($i-j$)	Cu-Co	Hf-Co	Co-Ti	Co-Zr	Cu-Be	Be-Ni	Be-Ti	Be-Zr	Cu-Cr	Cu-Fe
$\Delta H_{ij}^{\text{mix}}$ (kJ/mol)	6	-35	-28	-41	0	-4	-30	-43	12	13

Table 22. Thermodynamic parameters measured at 1000°C for equiatomic alloy composition

Alloys	$\Delta S_{\text{mix}}/R$	S_{Corr}/R	S_E/R	p	ΔH_{mix} (KJ/mol)	ΔG_{mix} (KJ/mol)	ΔG_{Corr} (KJ/mol)
CrMn	0.6931	0.6183	-0.0749	1.372	2	-5.34	-4.54
CrFe	0.6931	0.6926	-0.0006	0.117	-1	-8.34	-8.33
CrCo	0.6931	0.6931	-3.4×10^{-5}	0.028	-4	-11.34	-11.34
CrNi	0.6931	0.6931	-9.6×10^{-5}	0.048	-7	-14.34	-14.34
MnFe	0.6931	0.6100	-0.0836	1.453	0	-7.34	-6.45
MnCo	0.6931	0.6215	-0.0716	1.340	-5	-12.34	-11.57
MnNi	0.6931	0.6140	-0.0791	1.412	-8	-15.34	-14.50
FeCo	0.6931	0.6922	-0.0009	0.150	-1	-8.34	-8.33
FeNi	0.6931	0.6929	-0.0002	0.072	-2	-9.34	-9.33
CoNi	0.6931	0.6928	-0.0003	0.079	0	-7.34	-7.33
FeCrNi	1.0986	1.0710	-0.0276	0.820	-4.44	-16.07	-15.78
CoCrFeNi	1.3863	1.3568	-0.0295	0.849	-3.75	-18.42	-18.11
Al _{0.25} CoCrFeNi	1.5285	1.3034	-0.2250	2.497	-6.75	-22.93	-20.55
CoCrFeNiMn	1.6094	1.4499	-0.1595	2.057	-4.16	-21.19	-19.51
CoCrFeNiCu	1.6094	1.5090	-0.1004	1.601	3.20	-13.83	-12.77
CuHfNiTiZr	1.6094	0.7670	-0.8424	6.222	-27.36	-44.39	-35.48
CuHfCoTiZr	1.6094	0.8053	-0.8041	5.967	-23.52	-40.55	-32.04
CuBeNiTiZr	1.6094	0.7651	-0.8444	6.235	-30.24	-47.27	-38.34
Zr _{46.75} Ti _{8.25} Cu _{7.5} Ni ₁₀ Be _{27.5} (V4)	1.3409	0.5050	-0.8359	6.178	-38.92	-53.11	-44.27

Figure 45 schematically illustrates the difference in potential energy landscape (PEL) of low entropy alloys, high entropy alloys and amorphous alloys. In solid solution based low entropy alloys, configurational entropy is low and PEL is relatively smooth. PEL in high entropy alloys is characterized by some undulations with few low potential energy sites i.e. atomic traps. Formation of amorphous alloys is generally attributed to the very rugged PEL, with large number of low

potential energy sites, where glass transition occurs by trapping the atoms into low potential energy sites. Figure 46 shows the magnitude of normalized potential energy fluctuation in FeNi, FeCrNi, CoCrFeNi, CoCrFeNiMn, Al_{0.25}CoCrFeNi and Viterloy 4. Comparison suggest that amorphous alloy i.e. Viterloy 4 exhibits significantly higher fluctuation in lattice potential energy in comparison to crystalline alloys including high entropy alloys.

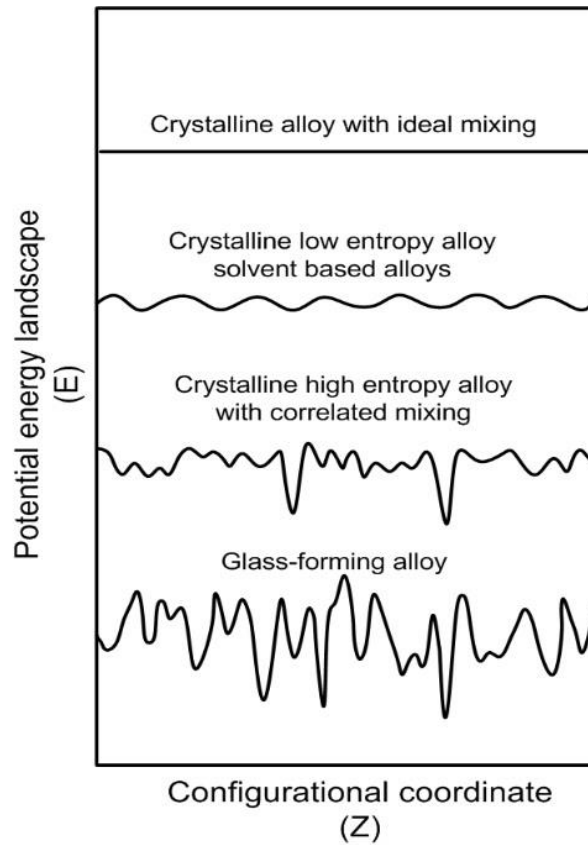


Figure 45. Schematic illustration of the potential energy landscape (PEL) for ideal mixing, low entropy alloys, high entropy alloy and glass forming alloy.

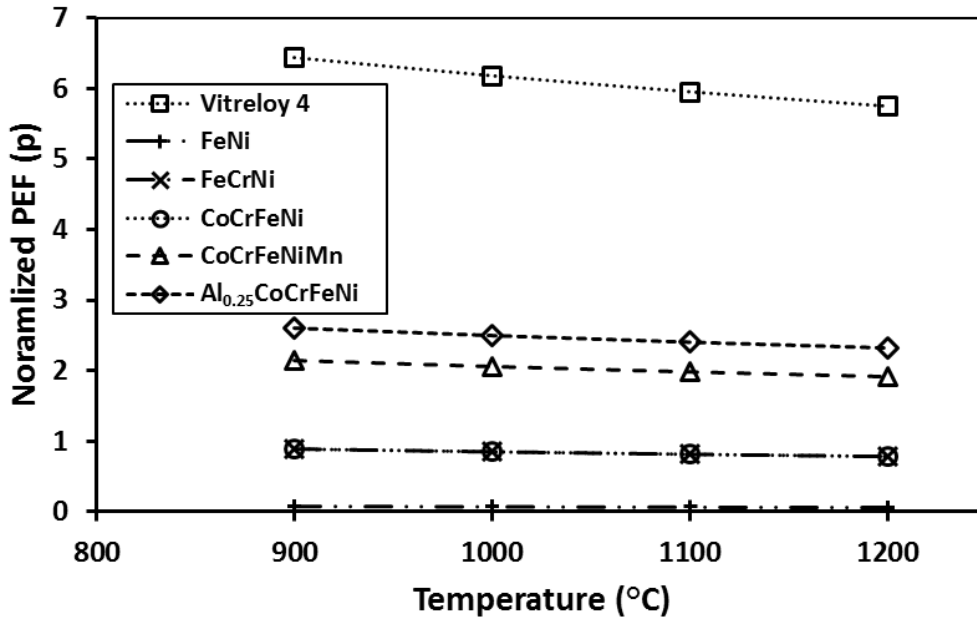


Figure 46. Normalized potential energy fluctuation as a function of temperature in FeNi, FeCrNi, CoCrFeNi, CoCrFeNiMn, Al_{0.25}CoCrFeNi and Viterloy 4

Normalized potential energy fluctuation ($p = \Delta E/k_B T$) in equiatomic FeCrNi and CoCrFeNi is approximately equal and less than 1. When $p < 1$, thermal energy fluctuation ($k_B T$) is more than potential energy fluctuations (ΔE), and so atoms have enough energy to come out of low potential traps. Therefore, ideally diffusion should be fast in such systems. However, when $p > 1$, as in case of CoCrFeNi and Al_{0.25}CoCrFeNi alloys, potential energy fluctuations outweighs the thermal energy fluctuations, and consequently, configurational entropy starts to drop significantly. Therefore, ideally diffusion should be slow in such systems. Experimentally, diffusion of Ni in CoCrFeNi is slower than that in CoCrFeNiMn and Al_{0.25}CoCrFeNi, and no significant lowering of tracer diffusion coefficients of Ni was observed.

Larger p implies to the larger magnitude of difference between smallest and largest potential energy sites may not be overcome by thermal fluctuations. In case of equiatomic CoCrFeNiMn or Al_{0.25}CoCrFeNi alloy, potential energy fluctuation is twice the thermal energy fluctuations, however average effective interdiffusion coefficients are approximately same and Therefore, number of low potential energy sites is insignificant to impede the diffusion of atoms. Atomic diffusion in such case, may only be sluggish if the number of low potential energy sites are high. In amorphous alloys, large magnitude of fluctuation in potential energy results in higher probability of an atom getting trapped into low energy site. Consequently, configurational entropy of the system decreases as alloy system cannot explore all the microstates. Furthermore, due to significant correlation effect (atomic size mismatch and chemical bond misfit) configurational entropy of the system reduces to approximately 50% of the ideal value. Knorr *et al.* [90] determined the tracer diffusion of Ni in Viterloy 4 (Zr_{46.75}Ti_{8.25}Cu_{7.5}Ni₁₀Be_{27.5}) via radiotracer experiments and observed that Ni tracer diffusion follows the following Arrhenius relationship in temperature range from 555 to 680 K:

$$D \text{ (m}^2\text{/s)} = 4.32 \times 10^3 \exp\left(-\frac{266 \text{ kJ/mol}}{RT}\right) \quad (37)$$

Tracer diffusivity of Ni has been extrapolated to high temperature for comparison with the present data. Figure 47 compares the tracer diffusion coefficient of Ni in Viteloy 4 with tracer diffusion coefficient of Ni in CoCrFeNi, CoCrFeNiMn, and Al_{0.25}CoCrFeNi alloys. Tracer diffusion coefficient of Ni in Viteloy 4 is significantly higher than tracer diffusion coefficient of Ni in CoCrFeNi, CoCrFeNiMn, and Al_{0.25}CoCrFeNi alloys. Figure 48 compares the tracer diffusion

coefficient at 1000°C as a function normalized potential energy fluctuation (p) in CoCrFeNi, CoCrFeNiMn, Al_{0.25}CoCrFeNi, and Vitreloy 4. Vitreloy 4 with the highest potential energy fluctuation exhibits the highest Ni tracer diffusivity. This means that number of low potential energy sites in Vitreloy 4 may not be sufficient enough to slow down the overall diffusion phenomena.

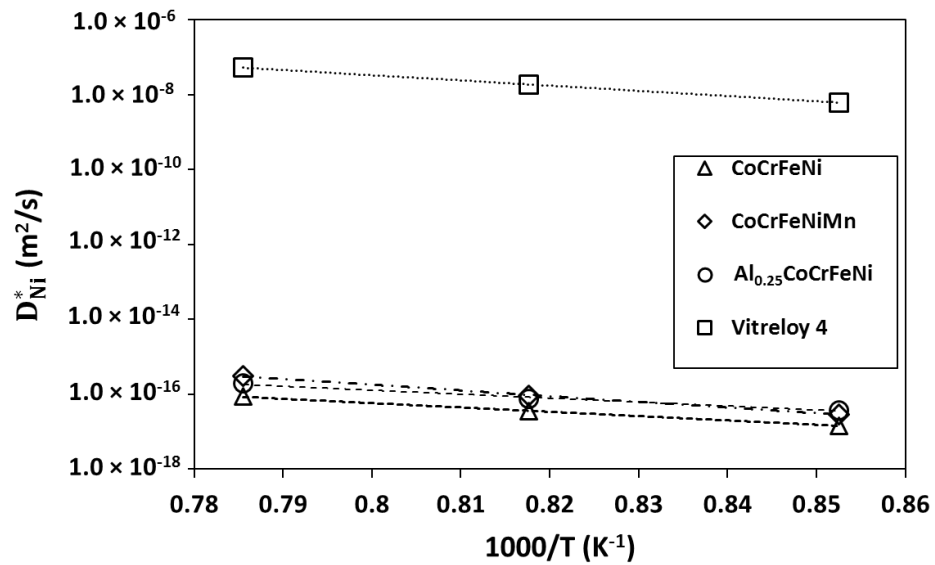


Figure 47. Tracer diffusion coefficient as a function of temperature in CoCrFeNi, CoCrFeNiMn, Al_{0.25}CoCrFeNi and Vitreloy4.

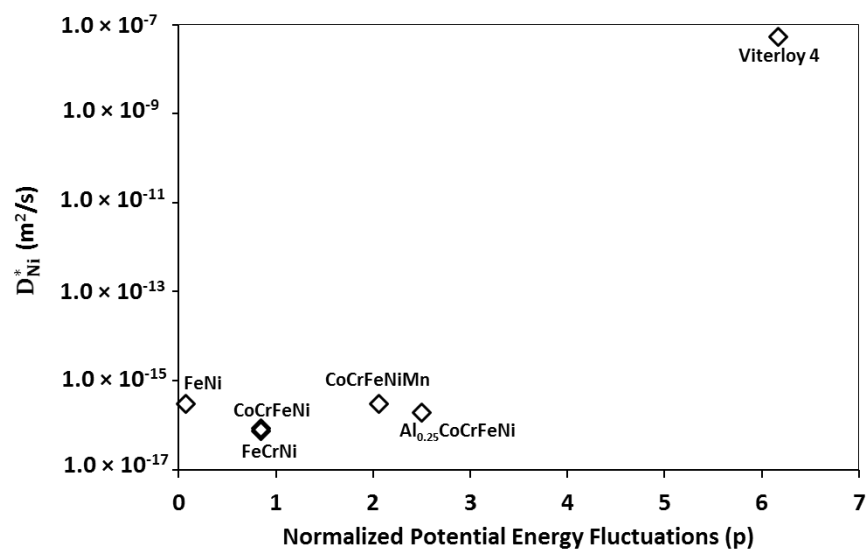


Figure 48. Tracer diffusion coefficient as a function normalized potential energy fluctuation (p) in CoCrFeNi, CoCrFeNiMn, Al_{0.25}CoCrFeNi and Viterloy4.

CHAPTER 7 SUMMARY AND CONCLUSIONS

7.1 High Entropy Effect

High entropy “core” effect was investigated in FCC Al-Co-Cr-Fe-Ni and Al-Co-Cr-Fe-Ni-Mn alloys by examining the off-equiatomic compositions, generated within the concentration profiles in solid-to-solid diffusion couple, i.e. $\text{Al}_{48}\text{Ni}_{52}$ vs. $\text{Co}_{25}\text{Cr}_{25}\text{Fe}_{25}\text{Ni}_{25}$ and $\text{Al}_{48}\text{Ni}_{52}$ vs. $\text{Co}_{20}\text{Cr}_{20}\text{Fe}_{20}\text{Ni}_{20}\text{Mn}_{20}$, annealed in temperature range from 900° to 1200°C . Maximum solubility limit of Al in face centered cubic off-equiatomic Al-Co-Cr-Fe-Ni and Al-Co-Cr-Fe-Ni-Mn alloys was determined as a function of temperature. Solubility limit of Al in off-equiatomic $\text{Al}_p\text{Co}_q\text{Cr}_r\text{Fe}_s\text{Ni}_t$ and $\text{Al}_p\text{Co}_q\text{Cr}_r\text{Fe}_s\text{Ni}_t\text{Mn}_u$ alloys was compared to the solubility limit of Al in equiatomic $\text{Al}_x\text{CoCrFeNi}$ and $\text{Al}_x\text{CoCrFeNiMn}$ alloys, respectively, determined using calculated equilibrium pseudo-binary phase diagram. Maximum solubility of Al in off-equiatomic $\text{Al}_p\text{Co}_q\text{Cr}_r\text{Fe}_s\text{Ni}_t$ and $\text{Al}_p\text{Co}_q\text{Cr}_r\text{Fe}_s\text{Ni}_t\text{Mn}_u$ alloys was observed to be higher than that in equiatomic $\text{Al}_x\text{CoCrFeNi}$ and $\text{Al}_x\text{CoCrFeNiMn}$ alloy at temperature of 1100°C or above temperature. Correspondingly, free energy of mixing for off-equiatomic $\text{Al}_p\text{Co}_q\text{Cr}_r\text{Fe}_s\text{Ni}_t$ and $\text{Al}_p\text{Co}_q\text{Cr}_r\text{Fe}_s\text{Ni}_t\text{Mn}_u$ alloys was determined to be lower than that of equiatomic $\text{Al}_x\text{CoCrFeNi}$ and $\text{Al}_x\text{CoCrFeNiMn}$ alloys at temperature of 1100°C or above. In other words, contribution of enthalpy of mixing was more significant in achieving higher thermodynamic stability in off-equiatomic alloy than equiatomic alloy, as entropic contribution was always higher for equiatomic alloy. Compositions of off-equiatomic $\text{Al}_p\text{Co}_q\text{Cr}_r\text{Fe}_s\text{Ni}_t$ and $\text{Al}_x\text{CoCrFeNiMn}$ alloys generated in

the diffusion couple were observed to follow the existing empirical rule for the formation of single phase in high entropy alloys.

7.2 Sluggish Diffusion Effect

Sluggish diffusion “core” effect was investigated by measuring interdiffusion coefficients of individual elements in Co-Cr-Fe-Ni, Co-Cr-Fe-Ni-Mn, Al-Co-Cr-Fe-Ni and Al-Co-Cr-Fe-Ni-Mn alloys and tracer diffusion coefficient of Ni in near equiatomic CoCrFeNi, CoCrFeNiMn, and Al_{0.25}CoCrFeNi. Both interdiffusion and tracer diffusion coefficients were compared with relevant low entropy alloy system from literature. A reduction in the magnitude of interdiffusion coefficients was not observed for all individual components in higher component alloy system. Similarly, tracer diffusion of Ni in higher component system was in fact higher than tracer diffusion of Ni in some low entropy system. Overall, sluggish diffusion effect was not observed in present study. Using potential energy fluctuation model, normalized potential energy fluctuation was measured in all the relevant system. It was hypothesized that diffusion is sluggish in systems which exhibit higher fluctuation in lattice potential energy. However, present study do not support this argument. In order to validate the present observation an extreme case from literature was investigated, where the potential energy fluctuation is significantly higher than alloys investigated in present study. Potential energy fluctuations in Vitreloy 4 is 3-6 times higher than alloys investigated in present study, but the tracer diffusion of Ni in Vitreloy 4 is significantly higher than tracer diffusion of Ni in alloys investigated in present study, when compared at same temperature. This clearly suggests that diffusion phenomena could not be always correlated with

the lattice potential fluctuations in an alloy. Therefore, to determine the nature of diffusion number of low potential sites have more significant impact than overall difference in energy of the highest and the lowest potential energy site.

7.3 Overall Conclusion

This study experimentally validates that two of the four initially proposed core effects cannot be generalized for all the high entropy alloys. Contrary to high entropy effect, off-equiatomic (i.e. low entropy of mixing) alloys may exhibit the lower free energy at high temperature than their equiatomic (i.e. higher entropy of mixing) counterparts. Although, entropic contribution towards the overall free energy is always higher in equiatomic alloys than off-equiatomic alloys, enthalpy contribution may become significant in off-equiatomic alloy which may impart higher thermodynamic stability than equiatomic alloys. Diffusion is not always slow in alloys with higher configurational entropy in comparison to alloys with low configurational entropy. Correspondingly, potential energy fluctuation may not be an important factor to determine the nature of diffusion in alloys. Rather, fraction of low potential energy sites could be a possible predictor to determine the nature of diffusion in alloys.

APPENDIX A: X-RAY DIFFRACTION AND COMPOSITION OF ALLOYS

A.1 Compositions of alloys

The actual compositions of the five alloys were examined by X-ray energy dispersive spectroscopy (XEDS) equipped on a Zeiss™ Ultra 55 field emission scanning electron microscope (FE-SEM). For the XEDS analysis, 15 random measurements were performed on each sample so as to obtain the average value with standard deviation. Table 23 outline the compositions of the alloys prepared via arc-melting.

Table 23. Compositions and lattice parameter of the alloys prepared for present study

System	Alloy	Al (at.%)	Co (at.%)	Cr (at. %)	Fe (at.%)	Ni (at.%)	Mn (at.%)
Binary	Fe ₅₀ Cr ₅₀	-	-	50.62 (0.53)	49.39 (0.61)	-	-
	Co ₅₀ Ni ₅₀	-	51.45 (0.36)	-	-	48.57 (0.42)	-
	Al ₄₈ Ni ₅₂	48.10 (0.29)	-	-	-	51.90 (0.34)	-
Quaternary	Co ₂₅ Cr ₂₅ Fe ₂₅ Ni ₂₅	-	24.73 (0.2)	25.77 (0.36)	25.28 (0.23)	24.22 (0.19)	-
	Co ₂₀ Cr ₂₇ Fe ₃₃ Ni ₂₀	-	20.44 (0.49)	27.35 (1.27)	32.70 (0.74)	19.47 (0.11)	-
	Co ₃₀ Cr ₂₀ Fe ₂₀ Ni ₃₀	-	28.85 (0.31)	19.76 (0.35)	20.82 (0.61)	29.57 (0.27)	-
Quinary	Co ₂₀ Cr ₂₀ Ni ₂₀ Fe ₂₀ Mn ₂₀	-	19.21 (0.19)	20.59 (0.26)	20.14 (0.24)	19.18 (0.17)	20.91 (0.23)
	Co ₂₅ Cr ₂₅ Fe ₁₅ Ni ₂₅ Mn ₁₀	-	24.58 (0.62)	25.53 (0.24)	15.19 (0.31)	23.94 (0.52)	10.78 (0.09)
	Co ₁₅ Cr ₁₅ Fe ₂₅ Ni ₁₅ Mn ₃₀	-	14.68 (0.29)	15.62 (0.10)	25.51 (0.19)	14.21 (0.17)	30.00 (0.29)
	Al ₆ Co ₁₉ Cr ₂₈ Fe ₂₈ Ni ₁₉	5.37 (0.21)	18.81 (0.19)	28.81 (0.13)	28.39 (0.20)	18.58 (0.18)	-
	Al ₆ Co ₂₈ Cr ₁₉ Fe ₁₉ Ni ₂₈	6.21 (0.26)	27.50 (0.18)	19.88 (0.14)	19.29 (0.14)	27.13 (0.20)	-

A.2 X-ray diffraction of alloys

X-ray diffraction was used to determine crystal structure and confirm the single phase (solid solutions) in the alloys prepared via arc-melting. Figure 49 through Figure 59 shows the X-ray diffraction patterns for all the alloys examined in this study. All alloys exhibit the single phase (i.e. solid-solution) microstructure with simple crystal structures i.e FCC or BCC, based on X-ray diffraction pattern. Table 24 reports the lattice parameter and crystal structure of all alloys after homogenization heat treatment.

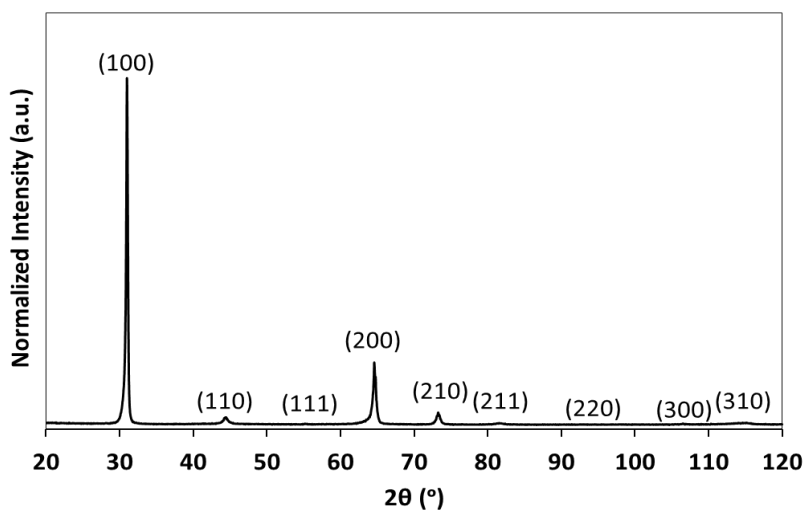


Figure 49. X-ray diffraction pattern of Al₄₈Ni₅₂ alloy.

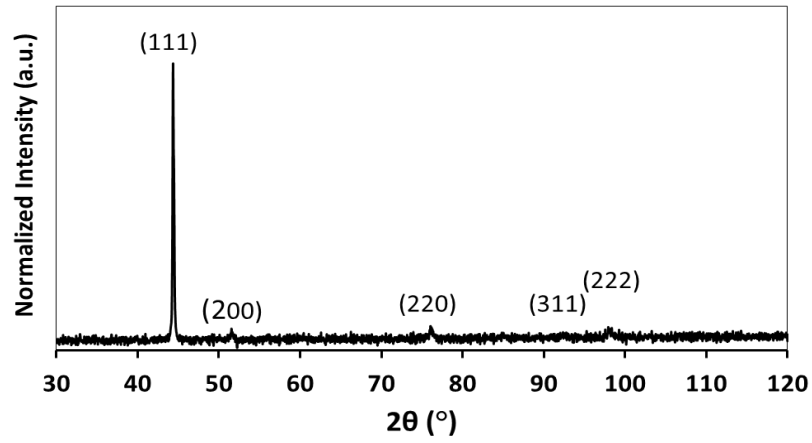


Figure 50. X-ray diffraction pattern of Co₅₀Ni₅₀ alloy.

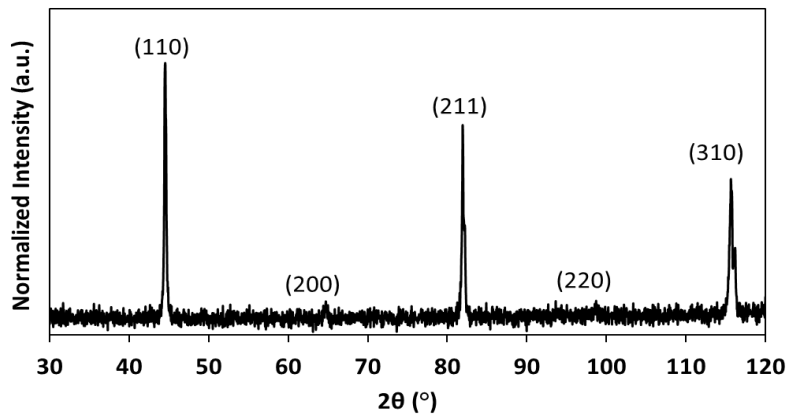


Figure 51. X-ray diffraction pattern of Fe₅₀Cr₅₀ alloy.

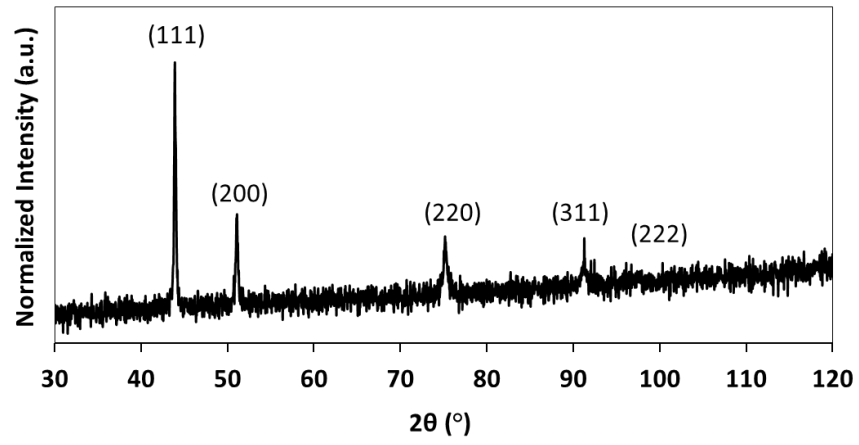


Figure 52. X-ray diffraction pattern of $\text{Co}_{25}\text{Cr}_{25}\text{Fe}_{25}\text{Ni}_{25}$ alloy.

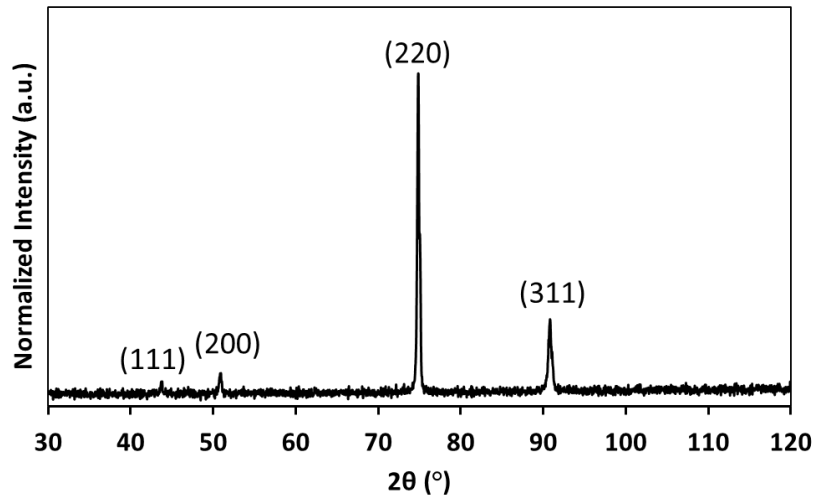


Figure 53. X-ray diffraction pattern of $\text{Co}_{20}\text{Cr}_{27}\text{Fe}_{33}\text{Ni}_{20}$ alloy.

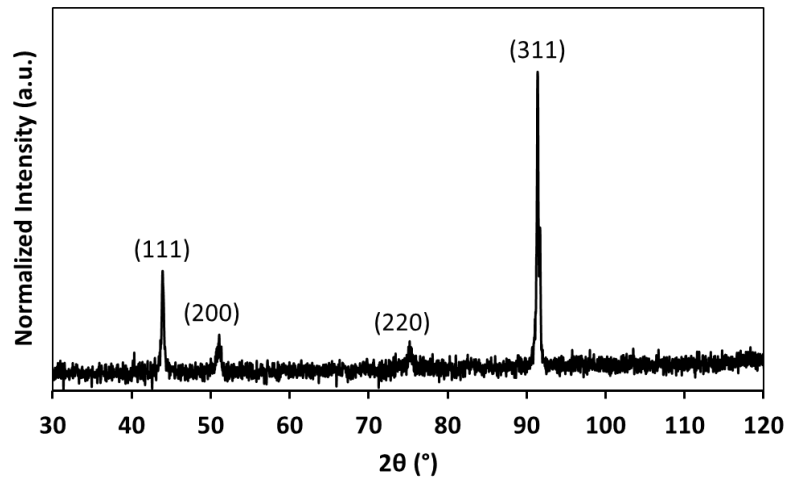


Figure 54. X-ray diffraction pattern of $\text{Co}_{30}\text{Cr}_{20}\text{Fe}_{20}\text{Ni}_{30}$ alloy.

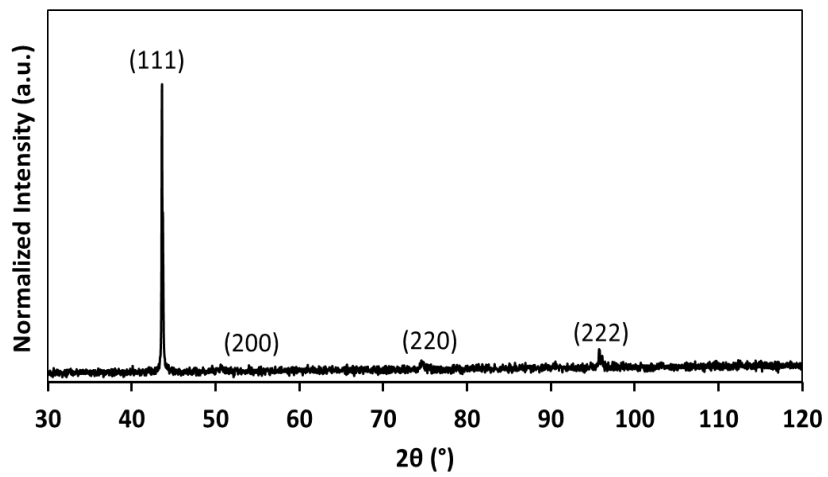


Figure 55. X-ray diffraction pattern $\text{Co}_{20}\text{Cr}_{20}\text{Fe}_{20}\text{Ni}_{20}\text{Mn}_{20}$ alloy.

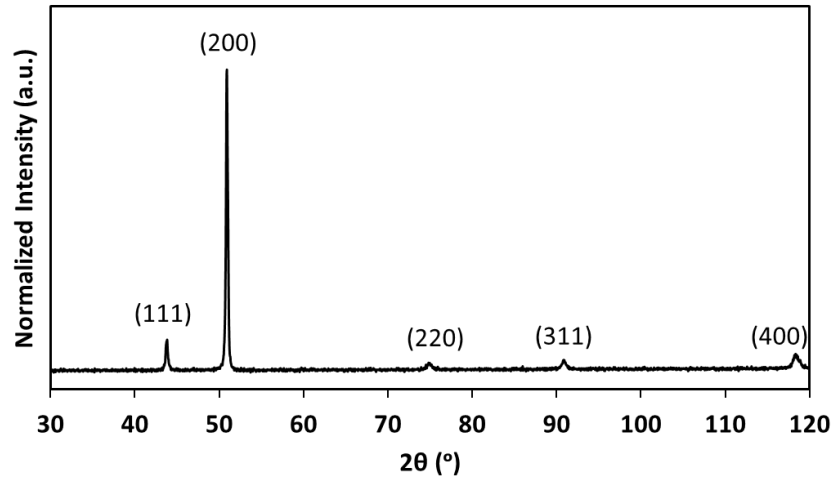


Figure 56. X-ray diffraction pattern of $\text{Co}_{25}\text{Cr}_{25}\text{Ni}_{25}\text{Fe}_{15}\text{Mn}_{10}$ alloy.

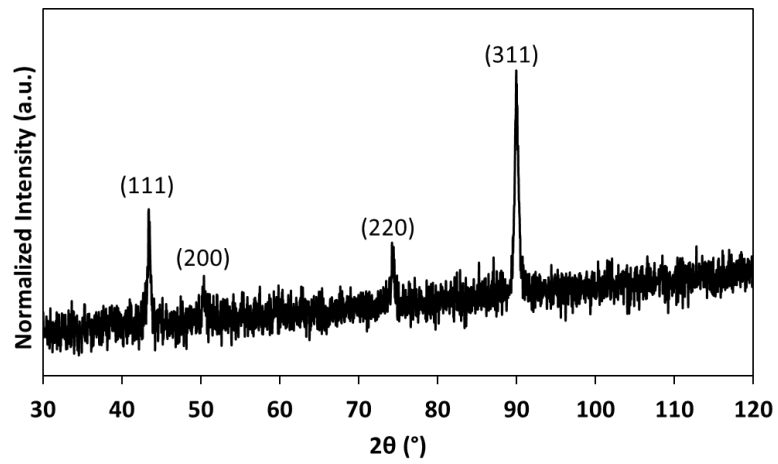


Figure 57. X-ray diffraction pattern of $\text{Co}_{25}\text{Cr}_{25}\text{Ni}_{25}\text{Fe}_{15}\text{Mn}_{10}$ alloy.

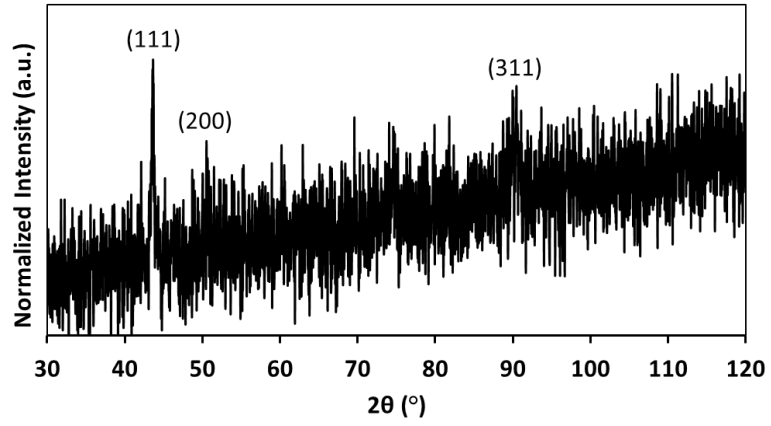


Figure 58. X-ray diffraction pattern of Al₆Co₂₈Cr₁₉Fe₁₉Ni₂₈ alloy.

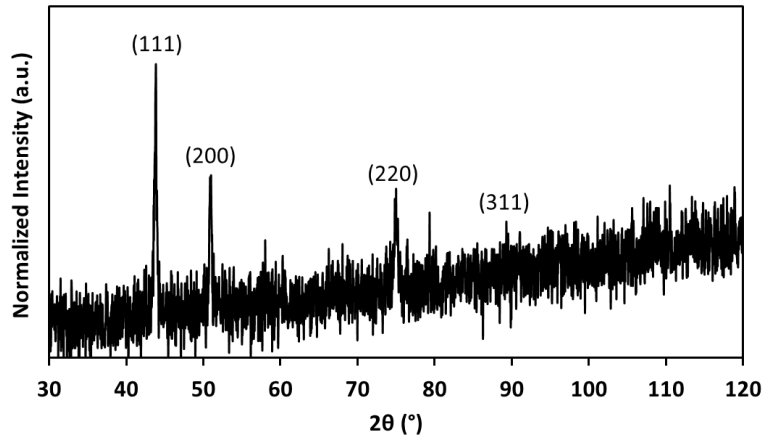


Figure 59. X-ray diffraction pattern of Al₆Co₂₈Cr₁₉Fe₁₉Ni₂₈ alloy.

Table 24. Lattice parameters and crystal structure of the alloys determined using X-ray diffraction

System	Alloy	Lattice parameters (Å)	Crystal structure
Binary	Fe ₅₀ Cr ₅₀	2.88 (0.00)	BCC (B2)
	Co ₅₀ Ni ₅₀	3.54 (0.00)	FCC (L1 ₂)
	Al ₄₈ Ni ₅₂	2.89 (0.00)	BCC (B2)
Quaternary	Co ₂₅ Cr ₂₅ Fe ₂₅ Ni ₂₅	3.58 (0.00)	FCC (L1 ₂)
	Co ₂₀ Cr ₂₇ Fe ₃₃ Ni ₂₀	3.59 (0.00)	FCC (L1 ₂)
	Co ₃₀ Cr ₂₀ Fe ₂₀ Ni ₃₀	3.57 (0.00)	FCC (L1 ₂)
Quinary	Co ₂₀ Cr ₂₀ Ni ₂₀ Fe ₂₀ Mn ₂₀	3.60 (0.01)	FCC (L1 ₂)
	Co ₂₅ Cr ₂₅ Fe ₁₅ Ni ₂₅ Mn ₁₀	3.58 (0.00)	FCC (L1 ₂)
	Co ₁₅ Cr ₁₅ Fe ₂₅ Ni ₁₅ Mn ₃₀	3.61 (0.00)	FCC (L1 ₂)
	Al ₆ Co ₁₉ Cr ₂₈ Fe ₂₈ Ni ₁₉	3.61 (0.01)	FCC (L1 ₂)
	Al ₆ Co ₂₈ Cr ₁₉ Fe ₁₉ Ni ₂₈	3.58 (0.01)	FCC (L1 ₂)

APPENDIX B: LIST OF PUBLICATIONS AND PRESENTATION

B.1 Publications

1. **A. Mehta**, Y.H. Sohn “Interdiffusion, solubility limit, role of entropy in FCC AlCoCrFeNiMn alloys”, in preparation.
2. **A. Mehta**, Y.H. Sohn “Interdiffusion, solubility limit, role of entropy in FCC AlCoCrFeNi alloys”, in preparation.
3. **A. Mehta**, I.V. Belova, G.E. Murch , Y.H. Sohn, “Formalism to measure tracer diffusion coefficients in multicomponent alloys, including High entropy alloys, using radioactive isotope free sandwich diffusion couple experiments”, in preparation.
4. R. Newell, **A. Mehta**, D.D. Keiser Jr., Y.H. Sohn “Phase reversion kinetics of thermally decomposed ($\alpha + \gamma'$) phases to γ -phase in U-10 wt.% Mo alloy”, Journal of Nuclear Materials (2019) submitted.
5. R. Newell, **A. Mehta**, Y.J. Park, D.D. Keiser Jr., Y.H. Sohn, “Microstructural characteristics of plasma sprayed, electroplated, and roll-bonded Zr diffusion barriers in hot isostatic pressed low enriched U-10 wt.% Mo monolithic fuel plates”, Journal of Nuclear Materials (2019) submitted.
6. **A. Mehta**, J. Dickson, R. Newell, D.D. Keiser, Jr., Y.H. Sohn, “Interdiffusion and reaction between Al and Zr in temperature range of 425° to 475°C”, Journal of Phase Equilibria and Diffusion (2019).
7. R. Newell, Z. Wang, I. Arias, **A. Mehta**, Y.H. Sohn, S.J. Florczyk, “Direct contact cytotoxicity evaluation of CoCrFeNi-based multi-principal element alloys”, 2018, Journal of Functional Biomaterials, 9 (4), 59.
8. L. Zhou, **A. Mehta**, B. McWilliams, K. Cho, Y.H. Sohn “Microstructure, Precipitates and Mechanical Properties of Powder Bed Fused Inconel 718 Before and After Heat Treatment”, Journal of Materials Science & Technology, (2019).
9. E. Schulz, **A. Mehta**, S.H. Park, Y.H. Sohn “Effects of Marker Size and Distribution on the Development of Kirkendall Voids, and Coefficients of Interdiffusion and Intrinsic Diffusion”, Journal of Phase Equilibria and Diffusion (2019).
10. E. Schulz, **A. Mehta**, I.V. Belova, G.E. Murch, Y.H. Sohn, “Simultaneous Measurements of Isotope-free Tracer Diffusion Coefficients and Interdiffusion Coefficients in Cu-Ni System”, Journal of Phase Equilibria and Diffusion 39 (2018), pp. 862-869.
11. **A. Mehta**, N. Eriksson, R. Newell, L. Zhou, E. Schulz, W. Sprowes, F. Betancor, Y. Park, D.D. Keiser, Jr., Y.H. Sohn, “Phase Transformations and Microstructural Development in the U-10 wt.% Mo Alloy with Varying Zr Content After Heat Treatments Relevant to the Monolithic Fuel Plate Fabrication Process”, Metallurgical and Materials Transactions A 50 (2019) pp 72-96.
12. L. Zhou, **A. Mehta**, E. Schulz, B. McWilliams, K. Cho, Y.H. Sohn, “Microstructure, Precipitates and Hardness of Selectively Laser melted AlSi10Mg alloy before and after heat treatment”, Materials Characterization 143 (2018) pp. 5-17.

13. R. Newell, **A. Mehta**, Y. Park, D.D. Keiser, Jr., Y.H. Sohn, "Interdiffusion, Reactions, and Phase Transformations Observed during Fabrication of Low Enriched Uranium Monolithic Fuel System for Research and Test Reactors," *Defects and Diffusion Forum*, 383 (2018) pp. 10-16.
14. **A. Mehta**, L. Zhou, E.A. Schulz, D.D. Keiser, Jr., J.I. Cole, Y.H. Sohn, "Microstructural Characterization of AA6061 vs. AA6061 HIP Bonded Cladding-Cladding Interface," *Journal of Phase Equilibria and Diffusion*, 39 (2018), pp. 246-254.
15. Y. Park, R. Newell, **A. Mehta**, D.D. Keiser Jr., Y.H. Sohn, "Interdiffusion and reaction between U and Zr", *Journal of Nuclear Materials*, 502 (2018) pp. 42-50.
16. L. Zhou, **A. Mehta**, K. Cho, Y.H. Sohn, "Composition-dependent interdiffusion coefficient, reduced elastic modulus and hardness in γ -, γ' - and β -phases in the Ni-Al system", *Journal of Alloys and Compounds*, 727 (2017) pp. 153-162.
17. R. Newell, **A. Mehta**, Y. Park, D.D. Keiser, Jr., Y.H. Sohn, "Relating diffusion couple experiment results to observed as-fabricated microstructures in low-enriched U-10wt.% Mo monolithic fuel plates", *Defects and Diffusion Forum*, 375 (2017) pp. 18-28.
18. R. Newell, Y. Park, **A. Mehta**, , D.D. Keiser, Jr., Y.H. Sohn, "Mechanical properties examined by nanoindentation for selected phases relevant to the development of monolithic uranium-molybdenum metallic fuels", *Journal of Nuclear Materials*, 487 (2017) pp. 443-452.
19. L. Zhou, **A. Mehta**, A. Giri, K. Cho, Y.H. Sohn "Martensitic transformation and mechanical properties of $\text{Ni}_{49+x}\text{Mn}_{36-x}\text{In}_{15}$ ($x=0, 0.5, 1.0, 1.5$ and 2.0) alloys", *Materials Science & Engineering: A*, 646 (2015) pp 57-65.
20. **A. Mehta**, P. Chakraborty, R. K. Fotedar, E. Rajendrakumar, "Lab scale development of lead-lithium eutectic alloy by MHD stirring technique", *Fusion Science and Technology*, 65 (2014) pp 299-307.

B.2 Conference Presentations

1. **A. Mehta**, L. Zhou, Y.H. Sohn, “Diffusion in FCC AlCoCrFeNi high entropy alloys”, TMS 2019, March 10-14, 2019 , San Antonio (TX), USA.
2. **A. Mehta**, N. Eriksson, R. Newell, L. Zhou, E. Schulz, W. Sprowes, F. Betancor, Y. Park, D.D. Keiser, Jr., Y.H. Sohn, “Microstructural evolution and Phase Transformations in U-10 wt.% Mo Alloy with Varying Zr Content After Heat Treatments Relevant to the Monolithic Fuel Plate Fabrication Process”, TMS 2019, March 10-14, 2019 , San Antonio (TX), USA.
3. H. Hyer, L. Zhou, **A. Mehta**, Y.H. Sohn, “Microstructure and Hardness Evaluation of Al Alloys After a Single Laser Scan in Powder Bed Fusion”, TMS 2019, March 10-14, 2019 , San Antonio (TX), USA
4. R. Newell, **A. Mehta**, Y.J. Park, D.D. Keiser, Jr. (*Presenter*), Y.H. Sohn, “Microstructural characteristics of Zr diffusion barriers applied via electroplating, plasma spraying, and co-rolling in low enriched U-10wt.%Mo monolithic fuel plates after HIP, ”, NuMat 2018, Oct 14-18, 2018 Seattle (WA), USA.
5. **A. Mehta**, N. Eriksson, R. Newell, L. Zhou, E. Schulz, W. Sprowes, F. Betancor, Y. Park, D.D. Keiser, Jr. (*Presenter*), Y.H. Sohn, “Phase Transformations and Microstructural Development in the U-10 wt.% Mo Alloy with Varying Zr Content After Heat Treatments Relevant to the Monolithic Fuel Plate Fabrication Process”, NuMat 2018, Oct 14-18, 2018 Seattle (WA), USA.
6. **Mehta**, E. Schulz, I.V. Belova, G.E. Murch, Y.H. Sohn, “Simultaneous measurement of tracer and interdiffusion coefficients via isotope free diffusion couple experiments for Cu-Ni and Co-Cr-Fe-Ni alloys”, MS&T 2018, Oct 14-18, 2018 Columbus (OH), USA.
7. R. Newell, Z. Wang, I. Arias, **A. Mehta**, Y.H. Sohn, S.J. Florczyk, “Direct contact cytotoxicity evaluation of CoCrFeNi-based multi-principal element alloys,” SFB 2018, April 11-14, 2018, Atlanta (GA), USA.
8. L. Zhou, **A. Mehta**, Y.H. Sohn, “Microstructure and Mechanical properties of selectively laser melted IN718 alloy before and after heat treatment,” TMS 2018, March 11-15, 2018, Phoenix (AZ), USA.
9. **A. Mehta**, L. Zhou, Y.H. Sohn, “Diffusion in CoCrFeNi based high entropy alloys”, TMS 2018, March 11-15, 2018, Phoenix (AZ), USA.
10. E. Schulz, **A. Mehta**, I.V. Belova, G.E Murch, Y.H. Sohn, “Experimental demonstration of simultaneous measurement of isotope free tracer and interdiffusion coefficients”, MS&T 2017, Oct 8-12, 2017 Pittsburgh (PA), USA.
11. L. Zhou, **A. Mehta**, E. Schulz, B. McWilliams, K. Cho, Y.H. Sohn, “Microstructure, Precipitates and Hardness of Selectively Laser melted AlSi10Mg alloy before and after heat treatment”, MS&T 2017, Oct 8-12, 2017 Pittsburgh (PA), USA.

12. **A. Mehta**, L. Zhou, E. Schulz, D.D. Keiser, Jr., J.I. Cole, Y.H. Sohn, "Microstructural Characterization of AA6061 vs. AA6061 HIP Bonded Cladding-Cladding Interface," TMS-2017 146th Annual Meeting & Exhibition, Feb 26-March 2, 2017, San Diego, CA
13. E. Schulz, **A. Mehta**, I.V. Belova, Y.H. Sohn, "Simultaneous measurement of Isotope-Free Tracer and Interdiffusion Coefficients". TMS-2017 146th Annual Meeting & Exhibition, Feb 26-March 2, 2017, San Diego, CA
14. **A. Mehta**, Y. Park, D.D. Keiser, Jr., Y.H. Sohn, "Interdiffusion and Reaction between Al vs. X (X = Zr, Mo, U) diffusion Couples", 2016 TMS Annual Meeting & Exhibition, February 14-18, 2016, Nashville, Tennessee, USA.
15. K. Cho, A. Giri, F. Kellogg, C. Hofmeister, C. Kammerer, L. Zhou, E. Schulz, **A. Mehta**, Y.H. Sohn, "Progress Towards Development of Nanostructured Magnesium Alloys and Composites: Understanding of Magnesium Strengthening by Solid Solutioning and Grain Size Reduction," Invited Presentation at the Symposium on Bulk Processing of Nanostructured Powders and Nanopowders by Consolidation, TMS 2016, February 14-18, 2016, Nashville, Tennessee, USA.
16. **A. Mehta**, Y. Park, D.D. Keiser, Y.H. Sohn "Interdiffusion and Reaction in Al vs. Zr and Al vs. Mo Solid-to-solid Diffusion Couples", MS&T 2015, Oct 5 -8, 2015, Columbus OH.
17. **A. Mehta**, D.D. Keiser, Y.H. Sohn "Interdiffusion and Reaction in Binary Al vs. Zr and Ternary Al-Si vs. Zr Diffusion Couples", Hume-Rothery Award Symposium: Multicomponent Alloy Metallurgy, the Bridge from Materials Science to Materials Engineering, TMS 2015,, March 15-19, 2015, Orlando, FL.
18. **A. Mehta**, D.D. Keiser, Y.H. Sohn, "Interdiffusion and Reaction in Binary Al vs. Zr and Ternary Al-Si vs. Zr Diffusion Couples", Annual Joint Symposium & Exhibition of the Florida chapter of the American Vacuum Society (FLAVS), March 9-10, 2015, Orlando, FL.
19. **A. Mehta**, P. Chakraborty, R.K. Fotedar, E. Rajandrakumar, "Lab scale development of lead lithium eutectic alloy by MHD stirring technique" for second IAEA -ITER technical meeting on analysis of ITER Materials and Technologies, Dec 11-13, 2012, Gandhinagar, India.
20. **A. Mehta**, P. Chakraborty, R.K. Fotedar, E. Rajandrakumar, "Progress in development of lead-lithium eutectic alloy in India" during Indo-Russian workshop for LLCB TBM development held at Institute for Plasma Research, Nov 29-30, 2011, Gandhinagar, India.

LIST OF REFERENCES

1. Zhang, Y., et al., *Microstructures and properties of high-entropy alloys*. Progress in Materials Science, 2014. **61**: p. 1-93.
2. Yeh, J.W., et al., *Nanostructured high-entropy alloys with multiple principal elements: novel alloy design concepts and outcomes*. Advanced Engineering Materials, 2004. **6**(5): p. 299-303.
3. Cantor, B., et al., *Microstructural development in equiatomic multicomponent alloys*. Materials Science and Engineering: A, 2004. **375**: p. 213-218.
4. Yeh, J.W., *High-entropy multielement alloys*. 2002, Patent US 2002/0159914 A1.
5. Murty, B., J.-W. Yeh, and S. Ranganathan, *High-entropy alloys*. 2014: Butterworth-Heinemann.
6. Miracle, D. and O. Senkov, *A critical review of high entropy alloys and related concepts*. Acta Materialia, 2017. **122**: p. 448-511.
7. Cheng, K.-H., et al. *Recent progress in multi-element alloy and nitride coatings sputtered from high-entropy alloy targets*. in *Annales de chimie*. 2006. Lavoisier.
8. Ranganathan, S., *Alloyed pleasures: multimetallic cocktails*. Current science, 2003. **85**(5): p. 1404-1406.
9. Pickering, E. and N. Jones, *High-entropy alloys: a critical assessment of their founding principles and future prospects*. International Materials Reviews, 2016. **61**(3): p. 183-202.
10. He, Q., Y. Ye, and Y. Yang, *The configurational entropy of mixing of metastable random solid solution in complex multicomponent alloys*. Journal of Applied Physics, 2016. **120**(15): p. 154902.
11. Yeh, J.W., *Recent progress in high entropy alloys*. Ann. Chim. Sci. Mat, 2006. **31**(6): p. 633-648.
12. Wang, W.R., et al., *Effects of Al addition on the microstructure and mechanical property of Al_xCoCrFeNi high-entropy alloys*. Intermetallics, 2012. **26**: p. 44-51.
13. He, J., et al., *Effects of Al addition on structural evolution and tensile properties of the FeCoNiCrMn high-entropy alloy system*. Acta Materialia, 2014. **62**: p. 105-113.
14. Guo, Y., et al., *A superfine eutectic microstructure and the mechanical properties of CoCrFeNiMo_x high-entropy alloys*. Journal of Materials Research, 2018: p. 1-8.
15. Zhang, F., et al., *An understanding of high entropy alloys from phase diagram calculations*. Calphad, 2014. **45**: p. 1-10.

16. Otto, F., et al., *Relative effects of enthalpy and entropy on the phase stability of equiatomic high-entropy alloys*. Acta Materialia, 2013. **61**(7): p. 2628-2638.
17. Ruiz-Yi, B., et al., *The Different Roles of Entropy and Solubility in High Entropy Alloy Stability*. ACS combinatorial science, 2016. **18**(9): p. 596-603.
18. Yeh, J.-W., *Alloy Design Strategies and Future Trends in High-Entropy Alloys*. JOM, 2013. **65**(12): p. 1759-1771.
19. Tsai, M.-H. and J.-W. Yeh, *High-entropy alloys: a critical review*. Materials Research Letters, 2014. **2**(3): p. 107-123.
20. Yeh, J.-W., *Physical metallurgy of high-entropy alloys*. Jom, 2015. **67**(10): p. 2254-2261.
21. Tsai, K.Y., M.H. Tsai, and J.W. Yeh, *Sluggish diffusion in Co–Cr–Fe–Mn–Ni high-entropy alloys*. Acta Materialia, 2013. **61**(13): p. 4887-4897.
22. Tong, C.-J., et al., *Microstructure characterization of Al_xCoCrCuFeNi high-entropy alloy system with multiprincipal elements*. Metallurgical and Materials Transactions A, 2005. **36**(4): p. 881-893.
23. Chang, H.-W., et al., *Influence of substrate bias, deposition temperature and post-deposition annealing on the structure and properties of multi-principal-component (AlCrMoSiTi) N coatings*. Surface and Coatings Technology, 2008. **202**(14): p. 3360-3366.
24. Jones, N., et al., *Phase evolution in an Al 0.5 CrFeCoNiCu High Entropy Alloy*. Intermetallics, 2016. **71**: p. 43-50.
25. Vaidya, M., et al., *Ni tracer diffusion in CoCrFeNi and CoCrFeMnNi high entropy alloys*. Journal of Alloys and Compounds, 2016. **688**: p. 994-1001.
26. Zhao, S., Y. Osetsky, and Y. Zhang, *Preferential diffusion in concentrated solid solution alloys: NiFe, NiCo and NiCoCr*. Acta Materialia, 2017. **128**: p. 391-399.
27. Middleburgh, S., et al., *Segregation and migration of species in the CrCoFeNi high entropy alloy*. Journal of Alloys and Compounds, 2014. **599**: p. 179-182.
28. Mattsson, A.E. and W. Kohn, *An energy functional for surfaces*. The Journal of Chemical Physics, 2001. **115**(8): p. 3441-3443.
29. Huang, K.H. and J.W. yeh, *A Study on Multicomponent Alloy Systems Containing Equal-mole Elements*. Master's Thesis (National Tsing Hua University, Hsinchu, Taiwan), 1996.
30. Kulkarni, K. and G.P.S. Chauhan, *Investigations of quaternary interdiffusion in a constituent system of high entropy alloys*. AIP Advances, 2015. **5**(9): p. 097162.
31. Beke, D. and G. Erdélyi, *On the diffusion in high-entropy alloys*. Materials Letters, 2016. **164**: p. 111-113.

32. Dąbrowa, J., et al., *Interdiffusion in the fcc-structured Al-Co-Cr-Fe-Ni high entropy alloys: Experimental studies and numerical simulations*. Journal of Alloys and Compounds, 2016. **674**: p. 455-462.
33. Allnatt, A., et al., *A high accuracy diffusion kinetics formalism for random multicomponent alloys: application to high entropy alloys*. Philosophical Magazine, 2016. **96**(28): p. 2969-2985.
34. Verma, V., A. Tripathi, and K.N. Kulkarni, *On interdiffusion in FeNiCoCrMn high entropy alloy*. Journal of Phase Equilibria and Diffusion, 2017. **38**(4): p. 445-456.
35. Paul, T.R., I.V. Belova, and G.E. Murch, *Analysis of diffusion in high entropy alloys*. Materials Chemistry and Physics, 2018. **210**: p. 301-308.
36. Vaidya, M., et al., *Radioactive isotopes reveal a non sluggish kinetics of grain boundary diffusion in high entropy alloys*. Scientific reports, 2017. **7**(1): p. 12293.
37. Vaidya, M., et al., *Bulk tracer diffusion in CoCrFeNi and CoCrFeMnNi high entropy alloys*. Acta Materialia, 2018. **146**: p. 211-224.
38. Gaertner, D., et al., *Tracer diffusion in single crystalline CoCrFeNi and CoCrFeMnNi high entropy alloys*. Journal of Materials Research, 2018: p. 1-8.
39. Gaertner, D., et al., *Concentration-dependent atomic mobilities in FCC CoCrFeMnNi high-entropy alloys*. Acta Materialia, 2018.
40. Kottke, J., et al., *Tracer diffusion in the Ni–CoCrFeMn system: Transition from a dilute solid solution to a high entropy alloy*. Scripta Materialia, 2019. **159**: p. 94-98.
41. Onsager, L., *Theories and problems of liquid diffusion*. Annals of the New York Academy of Sciences, 1945. **46**(5): p. 241-265.
42. Dayananda, M. and C. Kim, *Zero-flux planes and flux reversals in Cu– Ni– Zn diffusion couples*. Metallurgical and Materials Transactions A, 1979. **10**(9): p. 1333-1339.
43. Kirkaldy, J.S., *Diffusion in multicomponent metallic systems*. Canadian Journal of Physics, 1957. **35**(4): p. 435-440.
44. Dayananda, M. and Y. Sohn, *Average effective interdiffusion coefficients and their applications for isothermal multicomponent diffusion couples*. Scripta materialia, 1996. **35**(6): p. 683-688.
45. Dayananda, M.A. and Y.H. Sohn, *A new analysis for the determination of ternary interdiffusion coefficients from a single diffusion couple*. Metallurgical and Materials Transactions A, 1999. **30**(3): p. 535-543.
46. Belova, I.V., Y.H. Sohn, and G.E. Murch, *Measurement of tracer diffusion coefficients in an interdiffusion context for multicomponent alloys*. Philosophical Magazine Letters, 2015. **95**(8): p. 416-424.

47. Schulz, E.A., et al., *Simultaneous Measurement of Isotope-Free Tracer Diffusion Coefficients and Interdiffusion Coefficients in the Cu-Ni System*. Journal of Phase Equilibria and Diffusion, 2018. **39**(6): p. 862-869.
48. Ye, Y., et al., *High-entropy alloy: challenges and prospects*. Materials Today, 2016. **19**(6): p. 349-362.
49. Ye, Y., et al., *Design of high entropy alloys: A single-parameter thermodynamic rule*. Scripta Materialia, 2015. **104**: p. 53-55.
50. Fang, S., et al., *Relationship between the widths of supercooled liquid regions and bond parameters of Mg-based bulk metallic glasses*. Journal of Non-Crystalline Solids, 2003. **321**(1): p. 120-125.
51. Bakker, H., *Enthalpies in alloys, Miedema's semi-empirical model*. Trans. Tech. Publications. 1998: Enfield Publishing & Distribution Company.
52. Takeuchi, A. and A. Inoue, *Classification of bulk metallic glasses by atomic size difference, heat of mixing and period of constituent elements and its application to characterization of the main alloying element*. Materials Transactions, 2005. **46**(12): p. 2817-2829.
53. Yang, X. and Y. Zhang, *Prediction of high-entropy stabilized solid-solution in multi-component alloys*. Materials Chemistry and Physics, 2012. **132**(2): p. 233-238.
54. Takeuchi, A. and A. Inoue, *Calculations of mixing enthalpy and mismatch entropy for ternary amorphous alloys*. Materials Transactions, JIM, 2000. **41**(11): p. 1372-1378.
55. Mizutani, U., *Hume-Rothery rules for structurally complex alloy phases*. 2016: CRC Press.
56. Guo, S., et al., *Effect of valence electron concentration on stability of fcc or bcc phase in high entropy alloys*. Journal of applied physics, 2011. **109**(10): p. 103505.
57. Liu, D., et al., *Ternary diffusion in Cu-rich fcc Cu–Al–Si alloys at 1073 K*. Journal of Alloys and Compounds, 2013. **566**: p. 156-163.
58. Cheng, K., et al., *Interdiffusion and atomic mobility studies in Ni-rich fcc Ni– Al– Mn alloys*. Journal of Alloys and Compounds, 2013. **579**: p. 124-131.
59. Mehta, A., et al., *Microstructural Characterization of AA6061 Versus AA6061 HIP Bonded Cladding–Cladding Interface*. Journal of Phase Equilibria and Diffusion, 2018. **39**(2): p. 246-254.
60. Schulz, E., et al., *Effects of Marker Size and Distribution on the Development of Kirkendall Voids, and Coefficients of Interdiffusion and Intrinsic Diffusion*. Journal of Phase Equilibria and Diffusion, 2019: p. 1-14.
61. Park, Y., et al., *Interdiffusion and reaction between U and Zr*. Journal of Nuclear Materials, 2018. **502**: p. 42-50.

62. Mehta, A., et al., *Interdiffusion and reaction between Al and Zr in the temperature range of 425° to 475°C*. Journal of Phase Equilibria and Diffusion, 2019.
63. Kao, Y.F., et al., *Microstructure and mechanical property of as-cast, -homogenized, and -deformed $Al_xCoCrFeNi$ ($0 \leq x \leq 2$) high-entropy alloys*. Journal of Alloys and Compounds, 2009. **488**(1): p. 57-64.
64. Komarasamy, M., et al., *Hierarchical multi-phase microstructural architecture for exceptional strength-ductility combination in a complex concentrated alloy via high-temperature severe plastic deformation*. Scripta Materialia, 2019. **162**: p. 38-43.
65. Wu, Z., et al., *Recovery, recrystallization, grain growth and phase stability of a family of FCC-structured multi-component equiatomic solid solution alloys*. Intermetallics, 2014. **46**: p. 131-140.
66. Wu, B., et al., *Microstructures and thermodynamic properties of high-entropy alloys $CoCrCuFeNi$* . Intermetallics, 2018. **93**: p. 40-46.
67. Li, C., et al., *Effect of alloying elements on microstructure and properties of multiprincipal elements high-entropy alloys*. Journal of Alloys and Compounds, 2009. **475**(1-2): p. 752-757.
68. Wang, W.-R., W.-L. Wang, and J.-W. Yeh, *Phases, microstructure and mechanical properties of $Al_xCoCrFeNi$ high-entropy alloys at elevated temperatures*. Journal of Alloys and Compounds, 2014. **589**: p. 143-152.
69. Guo, S., et al., *More than entropy in high-entropy alloys: Forming solid solutions or amorphous phase*. Intermetallics, 2013. **41**: p. 96-103.
70. Poletti, M. and L. Battezzati, *Electronic and thermodynamic criteria for the occurrence of high entropy alloys in metallic systems*. Acta Materialia, 2014. **75**: p. 297-306.
71. Yang, X., et al., *Phase stability of low-density, multiprincipal component alloys containing aluminum, magnesium, and lithium*. Jom, 2014. **66**(10): p. 2009-2020.
72. Dong, Y., et al., *Effects of electro-negativity on the stability of topologically close-packed phase in high entropy alloys*. Intermetallics, 2014. **52**: p. 105-109.
73. Ng, C., et al., *Entropy-driven phase stability and slow diffusion kinetics in an $Al_0.5CoCrCuFeNi$ high entropy alloy*. Intermetallics, 2012. **31**: p. 165-172.
74. Tsai, M.-H., J.-W. Yeh, and J.-Y. Gan, *Diffusion barrier properties of $AlMoNbSiTaTiVZr$ high-entropy alloy layer between copper and silicon*. Thin Solid Films, 2008. **516**(16): p. 5527-5530.
75. ZHANG, L., et al., *Fabrication and thermal stability of $AlCrTaTiNi/(AlCrTaTiNi)$ N bilayer diffusion barrier*. Acta Metall Sin, 2013. **49**(12): p. 1611-1616.

76. Tsai, M.-H., et al., *Thermally stable amorphous (Al Mo Nb Si Ta Ti V Zr) 50 N 50 nitride film as diffusion barrier in copper metallization*. Applied Physics Letters, 2008. **92**(5): p. 052109.
77. Chang, S.-Y., M.-K. Chen, and D.-S. Chen, *Multiprincipal-element AlCrTaTiZr-nitride nanocomposite film of extremely high thermal stability as diffusion barrier for Cu metallization*. Journal of The Electrochemical Society, 2009. **156**(5): p. G37-G42.
78. Sathiaraj, G. and P.P. Bhattacharjee, *Effect of starting grain size on the evolution of microstructure and texture during thermo-mechanical processing of CoCrFeMnNi high entropy alloy*. Journal of Alloys and Compounds, 2015. **647**: p. 82-96.
79. Sathiaraj, G.D. and P.P. Bhattacharjee, *Effect of cold-rolling strain on the evolution of annealing texture of equiatomic CoCrFeMnNi high entropy alloy*. Materials Characterization, 2015. **109**: p. 189-197.
80. Sathiaraj, G., M. Ahmed, and P.P. Bhattacharjee, *Microstructure and texture of heavily cold-rolled and annealed fcc equiatomic medium to high entropy alloys*. Journal of Alloys and Compounds, 2016. **664**: p. 109-119.
81. Tsai, C.-W., et al., *Deformation and annealing behaviors of high-entropy alloy Al_{0.5}CoCrCuFeNi*. Journal of Alloys and compounds, 2009. **486**(1-2): p. 427-435.
82. Ma, S., et al., *Microstructural features and tensile behaviors of the Al_{0.5}CrCuFeNi₂ high-entropy alloys by cold rolling and subsequent annealing*. Materials & Design, 2015. **88**: p. 1057-1062.
83. Biswas, K. and N. Gurao, *Deciphering micro-mechanisms of plastic deformation in a novel single phase Fcc-based MnFeCoNiCu high entropy alloy using crystallographic texture*. Materials Science and Engineering: A, 2016. **657**: p. 224-233.
84. Duh, J.G. and M.A. Dayananda. *Interdiffusion in Fe-Ni-Cr Alloys at 1100° C*. in *Defect and Diffusion Forum*. 1985. Trans Tech Publ.
85. Bronfin, M., G. Bulatov, and I. Drugova, *Self-diffusion of Ni in the intermetallic compound Ni₃Al and pure Ni*. Fiz. Met. Metalloved., 1975. **40**(2): p. 363-366.
86. Million, B., et al., *Diffusion processes in the Fe • Ni system*. Materials Science and Engineering, 1981. **50**(1): p. 43-52.
87. Rothman, S., L. Nowicki, and G. Murch, *Self-diffusion in austenitic Fe-Cr-Ni alloys*. Journal of Physics F: Metal Physics, 1980. **10**(3): p. 383.
88. Takeuchi, A. and A. Inoue, *Quantitative evaluation of critical cooling rate for metallic glasses*. Materials Science and Engineering: A, 2001. **304**: p. 446-451.
89. Miedema, A., P. De Chatel, and F. De Boer, *Cohesion in alloys—fundamentals of a semi-empirical model*. Physica B+ C, 1980. **100**(1): p. 1-28.

90. Knorr, K., et al., *Self-diffusion in the amorphous and supercooled liquid state of the bulk metallic glass Zr₄₆. 75Ti₈. 25Cu₇. 5Ni₁₀Be₂₇. 5*. Journal of non-crystalline solids, 1999. **250**: p. 669-673.